UNIVERSITY OF CALIFORNIA,
IRVINE

Exotic phenomena in 4f systems: from complex magnetism to surface conduction

DISSERTATION

submitted in partial satisfaction of the requirements
for the degree of

DOCTOR OF PHILOSOPHY

in Physics

by

Sean Michael Thomas

Dissertation Committee:
Jing Xia, Chair
Zachary Fisk
Sid Parameswaran

2016

# TABLE OF CONTENTS

# LIST OF FIGURES

# LIST OF TABLES

# ACKNOWLEDGMENTS

# CURRICULUM VITAE

## Sean Michael Thomas

### EDUCATION

**Doctor of Philosophy in Physics**     **2016**
University of California, Irvine     *Irvine, CA*

**Master of Science in Electrical Engineering**     **2011**
University of Pennsylvania     *Philadelphia, PA*

**Juris Doctor**     **2009**
Duke University     *Durham, NC*

**Bachelor of Science in Electrical Engineering**     **2005**
Washington University in St. Louis     *St.Louis, MO*

### RESEARCH EXPERIENCE

**Graduate Research Assistant**     **2012–2015**
University of California, Irvine     *Irvine, California*

### TEACHING EXPERIENCE

**Teaching Assistant**     **2011–2012**
University of California, Irvine     *Irvine, California*

## REFEREED JOURNAL PUBLICATIONS

Maarten Nijland, Sean Thomas, Mark A. Smithers, Nirupam Banerjee, Dave H. A. Blank, Guus Rijnders, Jing Xia, Gertjan Koster, and Johan E. ten Elshof. *Epitaxy on Demand.* Advanced Functional Materials, 2015, 25, 51405148 (2015).

Maarten Nijland, Antony George, Sean Thomas, Evert P. Houwman, Jing Xia, Dave H. A. Blank, Guus Rijnders, Gertjan Koster, and Johan E. ten Elshof. *Patterning of Epitaxial Perovskites from Micro and Nano Molded Stencil Masks.* Advanced Functional Materials 2014, 24, 68536861 (2014).

D.J. Kim*, S. Thomas*, T. Grant, J. Botimer, Z. Fisk, and Jing Xia. *Robust Surface Hall Effect and Nonlocal Transport in SmB6: Indication for an Ideal Topological Insulator.* Nature: Scientific Reports 3, 3150 (2013).

# ABSTRACT OF THE DISSERTATION

Exotic phenomena in 4f systems: from complex magnetism to surface conduction

By

Sean Michael Thomas

Doctor of Philosophy in Physics

University of California, Irvine, 2016

Jing Xia, Chair

For materials synthesized with f-electron elements, the interaction between f-electrons and conduction electrons often leads to interesting physics. As the temperature is lowered, the f-electrons can hybridize with the conduction electrons in a process known as the Kondo effect. In a Kondo lattice material, the screening may become coherent at the so-called coherence temperature T*. The resulting material is often metallic, containing heavy bands with effective masses many times larger than the free electron mass. In some cases, the development of coherence leads to a filled heavy-electron band where the chemical potential lies within the hybridization gap, resulting in insulating behavior.

$CeAgBi_2$ is an antiferromagnetic compound (TN = 6.4 K) belonging to the former (metallic) case. The close energy scales of the Kondo coherence, antiferromagnetism, and crystal field levels results in complex physical properties. Transport measurements reveal a coupling between the different magnetic phases and Hall resistivity. As the field is increased, the antiferromagnetic transition temperature is suppressed to zero Kelvin. Typically, this is expected to result in a quantum critical point. However, due to strange transport behavior in the paramagnetic regime, the usual signatures of quantum criticality are hidden.

$SmB_6$ is a Kondo insulator due to the fact that the hybridization results in the opening of a gap. However, as the temperature is further lowered, the resistance saturates. Originally

believed to be due to in-gap conduction states in the bulk, the true reason for the resistance saturation is a robust conducting surface state. Several theories predict that the surface state is a result of $SmB_6$ belonging to a class of materials known as topological insulators. However, direct imaging of the spin-momentum locking of the surface states indicative of a topological insulator has proved elusive. Through transport and magnetic measurements, indirect evidence of the nature of the conducting surface state is presented.

# Chapter 1

# Introduction

$f$-electron materials contain magnetic ions forming a lattice of localized moments. In a process described by the Kondo effect,[1] the spin of the localized moment is screened by the conduction electrons and eventually forms a nonmagnetic scattering center.[2] This is expected to result in a -ln($T$) temperature dependence in resistivity when the magnetic ions are present as impurities. If instead the magnetic ions are part of a crystal lattice, they generate what is known as a Kondo lattice.[3] In some cases the Kondo effect scattering develops coherence as the temperature is lowered, leading to hybridization between the conduction electrons and the $f$-electrons.

In heavy fermion systems the hybridization leads to large effective masses below a certain temperature as estimated through the electronic specific heat.[4] This occurs when the Kondo coherence leads to a metallic system. Typically, there is sudden drop in the resistivity of the material as coherence occurs and the $f$-electrons become less localized. For metallic systems the specific heat is written as $C/T = \gamma + \beta T^2$. Classically, the accepted definition of a heavy fermion system is one where the electronic contribution to specific heat ($\gamma$) is larger than 400 mJ/(f-atom·mol·K$^2$).[5] Normal metals have $\gamma$ on the order of unity. This definition for

heavy fermions given above is somewhat arbitrary, and there are many systems that have $\gamma$ smaller than 400 but much larger than that found in ordinary metals.

Kondo insulators are another class of materials found in strongly correlated $f$-electron systems. Instead of forming a metal, Kondo coherence results in insulating behavior due to the fact that there is exactly one charge carrier in the conduction band to screen each local moment. The resulting band structure is such that the chemical potential lies in a narrow gap (typically $\sim$10 mev). In general, these materials have unstable or mixed valence.[4] Empirically, nearly all Kondo insulators have a cubic crystal lattice.[6] These materials differ from conventional semiconductors in that the gap only forms below a characteristic temperature.[7] Renewed interest in Kondo insulators, particularly $SmB_6$, is due to a recent theoretical prediction that some of them may be topological insulators.[8] For $SmB_6$, it was predicted that inversion between the $4f$ and $5d$ band at the X point leads to both insulating behavior in the bulk and a time-reversal symmetry protected conducting surface state.[9]

Following this introduction are three chapters. The first focuses on experimental methods. The other two are case studies on the $f$-electron systems $CeAgBi_2$ and $SmB_6$.

Chapter 2 focuses on the experimental techniques used to collect the data for this thesis. After a brief explanation of the cryostats used, information is provided about the construction of a rotating sample stage for performing angle dependent measurements down to about 50 mK. The basic techniques behind measuring transport, specific heat, and AC susceptibility are briefly discussed. A longer section is devoted to the measurement of magnetization through torque magnetometry due to the slightly more specialized nature of the measurement.

Chapter 3 focuses on the measurement of the low temperature phase diagram of the frustrated Kondo system $CeAgBi_2$. Using torque magnetometry to measure the magnetization at temperatures as low as 30 mK, a rich $H-T$ phase diagram is uncovered. It includes a total

of five magnetic transitions culminating with the suppression of anti-ferromagnetic (AFM) order to zero temperature. At least one of these transitions was revealed to be strongly first order. Hall resistivity measurements reveal a coupling between the magnetic transitions and transport. There is a large jump in Hall resistivity and change in sign at the transition occurring near 54 kOe. Transverse resistance and specific heat measurements are used to try to determine whether the suppression of the AFM order results in a quantum critical point. Finally, an unusual upturn in the low temperature resistance in the paramagnetic (high-field) regime is considered.

Chapter 4 focuses on $SmB_6$, a potential topological insulator. Transport measurements reveal that at low temperatures the surface is conducting while the bulk remains highly insulating. Torque magnetometry is used to perform quantum oscillations experiments to determine the shape and characteristics of the metallic surface state. Unfortunately, it is revealed that the observed quantum oscillations are not from $SmB_6$ but instead are from subsurface inclusions of Aluminum. Lastly, Cerium and Gadolinium are doped into $SmB_6$ to understand the interplay between the surface state and magnetic dopants. The theories of topological insulators say that the surface state should be protected by time-reversal symmetry, so that doping with magnetic impurities may break time reversal symmetry and lead to a non-metallic surface. Due to doping inhomogeneities and the interaction of the dopants with bulk conductivity, the reaction of the surface state to magnetic impurities remains unclear.

# Chapter 2

# Experimental Background

## 2.1 Cryostats

Most measurements were performed in either an Quantum Design Physical Property Measurement System (PPMS) or an Oxford Instruments dilution refrigerator (DR). The main difference between the two cryostats are the available temperature ranges and maximum applied field. The PPMS is capable of continuous measurement from 400 K down to 2 K (300 mK with a He3 insert) and magnetic fields up to 9 T. The DR can reach slightly below 20 mK and fields as high as 12 T (14 T with additional cooling of the magnet). However, it is only capable of performing continuous measurements to temperatures as high as about 10 K. Further, changing samples in the DR is a time-consuming process, whereas it typically takes less than one minute to change samples in the PPMS. Thus, it is best to use the DR only for those samples where the extreme conditions (low temperature, higher field) are required to probe interesting physics.

## 2.1.1 Dilution Refrigerator Sample Stages

The dilution refrigerator does not come with a standard sample stage. The He3/He4 dilution process (for more information about the thermodynamics of this process see Chapter 7 of Pobell's *Matter and Methods and Low Temperatures*[10]) occurs at the mixing chamber, which is .35 m above the field center. This is so that the mixing chamber can be located in a region with almost no magnetic field (secondary windings provide field cancellation of stray fields from the primary magnet).

It was thus necessary to build a custom part to provide mechanical support to mount samples in the field-center region. One requirement is that the sample holder have adequate thermal conductivity to bring the cooling power of the mixing chamber to the samples. To provide better cooling to our samples, the sample stage was initially made out of copper. However, this proved somewhat problematic for two reasons. First, the eddy current heating was very large when ramping the field near 0 T due to the fact that fairly thick copper disks were used. Second, at low temperatures and high fields, copper develops a non-neglible additional heat capacity from the ordering of its nuclear magnetic moments.[10] For these reasons, the second iteration of the stage uses a dual construction of silver and plastics (Delrin and Torlon). The plastic provides structural support and also thermal insulation between the sample stage and slightly warmer radiation shield. Silver foils are used instead of thicker disks, and cooling power is provided from the mixing chamber through a series of silver wires. Silver was used instead of copper because the ordering temperature for its nuclear moments is roughly one order of magnitude lower than that of copper.

While most experiments can be performed at a fixed angle with respect to the magnetic field (allowing the use of a fairly simple sample stage), some experiments require that the samples be rotated with respect to the field (e.g., torque magnetometry measurements to explore de Hass-van Alphen oscillations as explained in section 2.2.4). A suitable sample
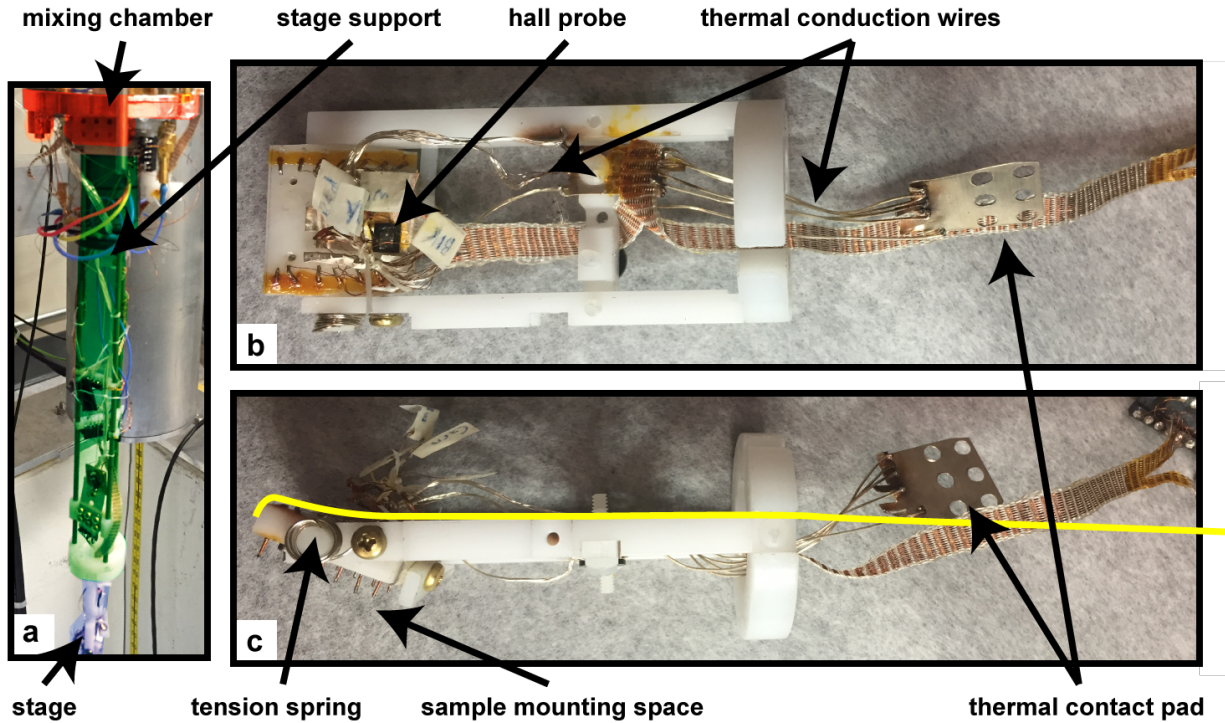
Figure 2.1: (a) Overview of how the sample stage mounts to the dilution refrigerator's mixing chamber. The mixing chamber is the red highlighted region, the stage support structure is the green highlighted region, and the stage is the blue highlighted region. (b) Top view and (c) side view of the rotating sample stage. The yellow line represents the pull-string for changing the rotation angle.

stage containing a rotating piece was designed and built for use in the DR. It is shown in figure 2.1 The sample stage is attached to a rigid support structure via a rotatable joint (basically, a rod through two holes on the rigid support). A berrylium-copper spring is used to apply tension so that it stays at a fixed position unless it is pulled. Pulling a string at the top of the DR insert allows turning the stage away from its equilibrium position. A hall probe mounted on the rotating part of the stage provides a way to accurately gauge the angle of rotation with respect to the applied field. To provide cooling to the sample stage, a large number of thin silver wires are welded directly to a silver foil on the rotating stage. It is necessary that both the silver wires and the instrument wiring are flexible enough to allow free rotation of the sample stage.

## 2.2 Measurement Techniques

### 2.2.1 Transport

Transport measurements are typically made using a 4-wire AC measurement with a lock-in amplifier. Standard lock-in amplifiers have a internal oscillator for generating an AC voltage and differential inputs for measuring an AC voltage. The sample is excited with a constant AC current by placing the AC output voltage in series with a resistor several orders of magnitude larger than the sample being measured ($I = V/R$). Typically, the excitation frequency is between 10 and 30 hz.

When measuring samples of very low resistivity, it is necessary that the impedance of the wires used for the differential voltage inputs is only on the order of several ohms. If the length of wire is long, it is helpful if the differential voltage lines are also made entirely of coaxial cable. Otherwise, the excitation current can couple to the voltage wires and create a very large background signal compared to the measurement signal. Due to the arbitrary phase of the background signal, it is quite difficult to separate out the part of the signal that is from the sample being measured. Thus, it is necessary to use coaxial cables in the DR
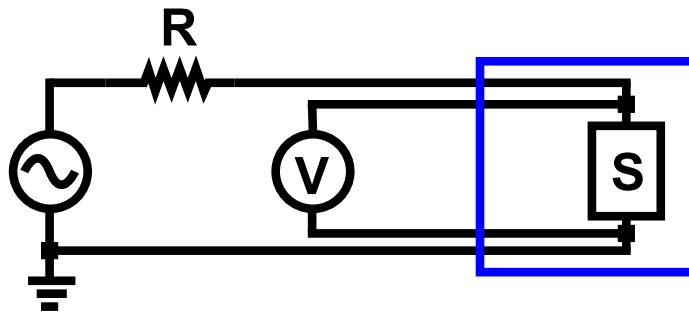


Figure 2.2: Diagram for 4-wire transport measurement. R is the resistor that determines the excitation current. S is the sample under test. V represents the differential voltage inputs on the lock-in amplifier. The source is an AC voltage out on the lock-in amplifier. The blue square represents the cryostat.

to measure samples with total resistance less than about .1 $\Omega$. No such issue exists in the PPMS, which also has an AC resistance bridge integrated with the cryostat control software that is capable of performing nearly all measurements.

## 2.2.2 Heat Capacity

Heat capacity can also be used to probe the properties of a material. For a metal at low enough temperatures, $C = \gamma T + \beta T^3$.[10] By plotting C/T versus T$^2$, both $\gamma$ and $\beta$ can be determined. $\gamma$ is the coefficient associated with the electron contribution, with larger values of $\gamma$ indicating a larger effective mass in the conduction electrons. $\beta$ is the coefficient associated with phonon contributions. Specific heat is also useful for detecting phase transitions. At a phase transition, the number of states accessible to the system increases, causing a jump in the heat capacity.

One way to measure heat capacity is using the relaxation technique. The sample is attached to a heat capacity platform containing a thermometer and a heater. The platform is weakly connected to a thermal bath. This can be achieved by using an appropriate length of resistive wire to make connections to the thermometer and heater, and heat sinking the other end of the wires to the thermal bath. If measuring at millikelvin temperatures, manganin wire should not be used because it has a large contribution to heat capacity from the Schottky anomaly that can overwhelm the heat capacity of the sample.[10] The sample platform is then suspended in vacuum by the resistive wire. With this method, a known amount of heat is applied to the sample platform for a specific period of time. The temperature of the sample platform is then allowed to relax back to the bath temperature. This relaxation is exponential, with time constant $\tau = C/\kappa$. The total heat capacity is given by $C = C_{sample} + C_{platform}$, with $\kappa$ being the thermal conductance of the link to the thermal bath. As long as $\kappa$ is lower than the thermal conductivities between all parts of the sample platform

8
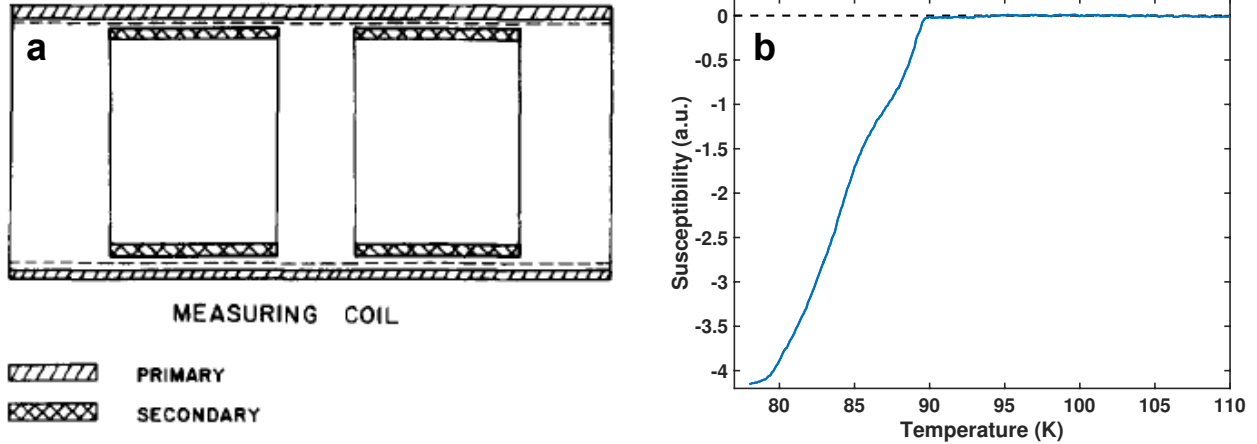
Figure 2.3: (a) Schematic of primary and secondary coils for AC susceptibility measurement. Borrowed from [12]. (b) An example measurement of $\chi'$ of a piece of a powdered YBCO superconducting magnet. The onset of $T_C$ is clearly visible, but the broad transition is due to the multi-crystalline nature of the material.

(i.e., platform, heater, thermometer, and sample), the relaxation can be fairly well described by a single exponential. By measuring the heat capacity of the sample platform setup before attaching any sample, the contribution from the sample can then be determined in a later measurement.[10]

### 2.2.3   AC Susceptibility

The magnetic susceptibility is the constant of proportionality between the magnetization of a sample and the applied magnetic field: $M = \chi H$.[11] AC susceptibility is the response of the magnetization to an AC magnetic field ($\chi_{AC} = dM/dH$) at a constant (DC) field and temperature. A simple way to measure AC susceptibility is by measuring the mutual inductance between a primary, excitation coil and a pair of secondary measurement coils (see figure 2.3). An AC current is applied to the excitation coil. This generates an AC voltage on each of the measurement coils due to the mutual inductance between the primary and secondary coils. The measurement coils are counter-wound, so that the voltage generated on each is 180° out of phase with the other.

9

By carefully winding each secondary coil the correct number of turns, without any sample the sum of the voltages of the excitation coils is close to zero. The presence of a sample inside one of the secondary coils alters both the phase and magnitude of the voltage generated by that coil. It can be shown that $V_x \propto -\chi''$ and $V_y \propto \chi'$, where $V_x$ and $V_y$ are the in-phase and out-out-phase components of the measured voltage, respectively. If a calibrated measurement is needed, each device must be individually calibrated by a material with known mass and AC susceptibility.

## 2.2.4  Torque Magnetometry

Torque magnetometry has been used in mapping electronic structures of macroscopic sized metal samples through detection of the De Haas-van Alphen effect (dHvA): the magnetic-field-induced quantum oscillation of magnetization.[13] More recently, the application of this technique has been extended to study phase transitions of the Dirac electrons in bismuth,[14] detect dHvA oscillations in a single-layer 2d electron gas,[15] and study Josephson vortex dynamics in nanogram sized single-crystals.[16] Advantages of torque magnetometry over other magnetic measurements are that the sensitivity can scale with the square of the applied field and that torque scales with the volume of the sample. A home-built torque magnetometer can achieve sensitivities near $1 \times 10^{-9}$ emu at 9 T. For comparison, squid magnetometers are usually limited to a sensitivity of $5 \times 10^{-8}$ emu, which decreases further at increasing fields.

**Background Material**

In a uniform applied field, a magnetic dipole will experience a torque causing it to align parallel with the field. A perfectly spherical sample with no inherent magnetic anisotropy will experience no torque, because the magnetization of the sample will be uniform and perfectly aligned with the applied field. However, many crystals have an anisotropic susceptibility, so

that the magnetization of the sample is not perfectly aligned with the applied field. This can be due to several different effects, including the shape of the sample and magnetocrystalline anisotropy.[17]

Samples that exhibit spontaneous magnetic ordering (ferro-, ferri-, and antiferromagnetic materials) have magnetocrystalline anisotropy, where the spontaneous magnetization aligns along one or more of the crystal axes (the easy axis). This effect arises from spin-orbit coupling, and prediction of the magnetocrystalline anisotropy generally requires *ab initio* calculation of the band structure.[18]

Even in samples with no spontaneous magnetization, the shape of the sample causes anisotropy in the magnetization. Shape anisotropy is caused by a demagnetizing field that is proportional to the magnetization of the crystal and anti-parallel to the magnetization in direction. The proportionality constant between the magnetization and the demagnetizing field (demagnetizing factor) is dependent on the shape of the crystal and the orientation of the crystal in the applied field. Further, for any crystal that is not a perfect ellipsoid, the demagnetizing factor will vary spatially within the crystal.

In materials that exhibit spontaneous magnetic ordering and in fields that are high enough to saturate the magnetization, the effects of shape anisotropy and magnetocrystalline anisotropy can often be of similar orders of magnitude.[19] This can obscure measurements of the magnetocrystalline anisotropy unless shape effects are accounted for. Further, the field inside the sample is equal to the applied field minus the demagnetizing field. If the sample is ferromagnetic, the saturation magnetization can be large enough that the magnitude of the demagnetizing field is a substantial fraction of the applied field (even in the high-field measurement regime for which torque magnetometry is best suited). If the sample is non-ellipsoidal, the field in the sample will be non-uniform. While in theory it may be possible to determine the demagnetizing coefficients everywhere in space for an arbitrary sample geometry, even for a rectangular prism the calculation of the demagnetizing coefficients in

all points in space is not trivial.[20] This is another reason that for ferromagnetic materials it is best to use ellipsoidal samples.

The above concerns are less of an issue for non-ferromagnetic materials. In such materials, the demagnetizing field is often small compared to the applied field. This means that the difference between the applied field and the actual field is effectively zero at any point in the sample.

Magnetic torque measurement is possible in materials even without magnetocrystalline anisotropy if the sample is of non-spherical shape. An oblong shape can be used to create an easy magnetic axis. If the long axis is not aligned with the applied field, there will be a torque acting on the sample.

For thin-films, there is an additional magnetic anisotropy due to surface effects.[21] The magnetic surface anisotropy tends to increase with decreasing film thickness and can either favor an easy-axis normal or parallel to the film plane. Thus, for very thin films the easy axis can switch from in-plane (due to shape anisotropy) to out-of-plane as surface effects begin to dominate.

For measuring quantum oscillations, the effects of anisotropy are not very important. Materials that exhibit quantum oscillations are metallic, so they will usually be para- or diamagnetic. Also, the amplitude of the oscillations can often be as large as the steady susceptibility of the crystal.[13] Because quantum oscillations are periodic with inverse field, any additional torque caused by the shape anisotropy can be treated as background.

The magnitude of the torque that a sample experiences in a uniform field is:

$$\tau = M_\perp V B \tag{2.1}$$

Where $M_\perp$ is the component of magnetization that is perpendicular to applied field, $V$ is the volume of the sample, and $B$ is the applied field. For a paramagnetic sample, the magnetization scales with the applied field. Thus, the torque acting on such a sample scales with the field squared. The scaling with applied field and volume of the sample makes torque magnetometry well-suited for studying larger samples in high fields.

One method of performing a torque magnetometry measurement is by measuring the deflection of the free end of a beam cantilever on which the sample is mounted to determine the torque acting on the sample. If the cantilever is constructed from a metal foil, the deflection can be determined by measuring the change in capacitance between the cantilever and a fixed conductor. For small changes in deflection, the angle of the sample in the magnetic field will be nearly constant and the change in capacitance of the cantilever will be proportional to the torque acting on the sample. For large torque beyond the small deflection regime, one can use a feedback system to apply a known current through a loop on the cantilever to cancel the torque generated by the sample, but such an approach was not used here.

Fig. 2.4(a) shows a schematic view of a beam cantilever device mounted in the dilution refrigerator. Shielded cables are used to connect the cantilever to a current-balance circuit that can measure the change in capacitance of the cantilever sensor. Both the cantilever and the fixed conductor are electrically isolated from ground. To reduce the effects of stray capacitance, every other metallic surface in the cryostat should be grounded. Further, the shielding layer of the coaxial cable should be terminated as close to the cantilever device as possible. Because of the low dissipation (less than 10 fW) inherent in a vacuum-gapped capacitive measurement, it is possible to perform the measurement at mK temperatures.

Using a lock-in amplifier capable of current measurement, the capacitance can be measured with sensitivity near 10 aF for sensors with total capacitance of 1 pF. As described in Huang et al.[22], when measuring a high impedance device is it necessary use a current measurement method to reduce the effects of the stray impedance to ground. To increase the resolution of
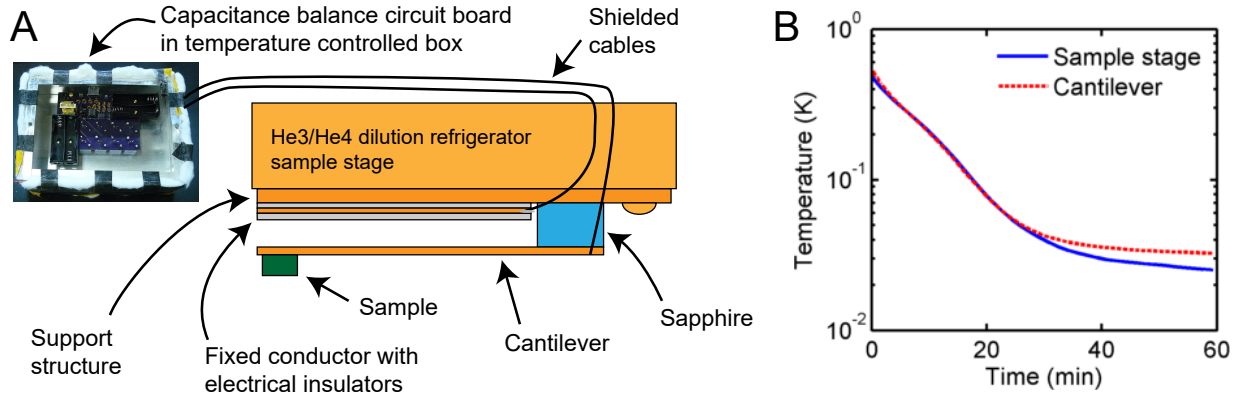
Figure 2.4: (a) Schematic for the cantilever construction. The cantilever device is attached to a base plate that is suspended below the mixing chamber of a $He^3/He^4$ dilution refrigerator. Shielding cables from the device are routed out of the cryostat to the current-balance circuit. (b) Comparison of sample stage temperature and cantilever temperature during the cooldown of the dilution refrigerator. The cantilever temperature tracks the sample stage temperature down to about 50 mK. After 20 minutes of thermal relaxation, the cantilever temperature reaches 30 mK.

the measurement, a current-balance method was used to bias the measured current at the equilibrium position of cantilever near zero.

## Cantilever Construction

For measurements in the mK temperature range it is important to select construction materials with suitable electrical, magnetic, and thermal properties. It is also necessary to consider the geometry of the cantilever, which controls the spring constant and equilibrium capacitance.

Fig. 2.4(a) details the construction used for the cantilever. Typical cantilevers are constructed on a .51 mm thick OFHC copper base piece that has a through hole drilled for mounting to the cryogenic sample stage attached to the mixing chamber in a dilution refrigerator. A cigarette paper is soaked in Ge-varnish and affixed to one end of the copper base. A thin copper foil is placed on top of the paper so that it is electrically insulated from the base. This foil serves as the fixed conductor. On the other end of the base a 435 $\mu$m

sapphire plate is affixed using low temperature epoxy (Loctite 1C Hysol). Using the same epoxy, a 35 $\mu$m thick copper foil is affixed to the top of the sapphire plate to serve as the cantilever arm. Because the thermal conductance of the epoxy is much lower than that of sapphire or copper at mK temperatures, it is necessary to make the epoxy layer as thin as possible. Ideally, some parts of the sapphire spacer should be in direct contact with both the cantilever and the base structure that is held at a fixed temperature through a heat link to the mixing chamber. The foil is cut into an I-shape, which allows for a smaller spring constant and also causes the motion of the free end of the cantilever to dominate the change in capacitance. To protect against an electrical short, the fixed conductor can be covered with a second piece of Ge-varnish soaked cigarette paper upon most of its surface except for a smaller corner to allow for an electrical contact to be made.

Copper is a useful material for the cantilever because foils of the appropriate thickness are readily available in the form of tape. Although there are materials (e.g., brass) that are less diamagnetic than copper, if the copper foil is mounted so that the plane of the foil is parallel to the applied field, the contributed torque signal will be minimal. If it is necessary to rotate the copper foil from this position, it may be necessary to subtract a background signal caused by the torque acting on the copper foil. Other materials, such as beryllium copper or kapton foils may be less subject to non-elastic deformation than copper, but have much lower thermal conduction. Copper foil was found to be the best material for measurement at mK temperatures due to its thermal properties, resulting in quick cooling of the sample.

The heat dissipated by the capacitance measurement is extremely low. For a typical sensor with a 1 pF equilibrium capacitance measured with a 2.5 V excitation at 2 kHz, the current through the device is only about 30 nA. With a vacuum-gapped capacitor, there is no lossy dielectric material in which heat is dissipated. Any device heating must be caused by ohmic losses in the wiring to the cantilever device, the solder joints, or in the copper foils that are used for the cantilever and fixed conductor. Even if the combined resistance were somehow

as high at 10 Ω, to total amount of heat dissipated would still be less than 10 fW, which is the level of heat generated by cosmic rays per gram of material.[10]

To check the sample temperature, a small ruthenium oxide thermometer (Scientific Instruments model RU600) was mounted to a cantilever device using Ge-varnish to mimic the sample. The thermometer was electrically insulated from the cantilever using a piece of Ge-varnish soaked cigarette paper. The electrical connection to the thermometer was made using thermally insulating manganin wires. It was found that the temperature of the cantilever and the sample stage remained nearly identical down to 50 mK (fig. 2.4(b)). After an additional 20 minutes of cooling, the temperature of the cantilever reached just over 30 mK. In an actual experiment, the sample is mounted directly to the surface of the cantilever, without the additional thermal barrier provided by the cigarette paper. Thus, it is likely that the thermal relaxation time and temperature of the sample may be even lower than that measured here.

For small deflections of the cantilever about its equilibrium position $(x_0)$, $\Delta C \propto -\Delta x/x_0^2$. The constant of proportionality is dependent on the effective area between the cantilever and the fixed conductor. Using available instruments, it has not been possible to measure capacitance with higher accuracy than about 10 aF (independent of the total capacitance values in the range of .5 pF to 10 pF). To increase sensitivity for a given deflection, $x_0$ should be as small as possible while ensuring that there is no chance that the motion of the free end of the cantilever may be obstructed.

The sample size and degree of magnetic anisotropy determine the magnitude of the torque acting on the cantilever. For each sample measured, a suitable spring constant of the can-

tilever must be chosen. The spring constant of the cantilever can be calculated as follows:[23]

$$k = \frac{E\omega t^3}{4l^3} \tag{2.2}$$

$E$ is the Young's modulus of the cantilever material, $t$ is the thickness, $\omega$ is the width, and $l$ is the length. A smaller spring constant maximizes the change in capacitance for a given change in applied torque to the cantilever. If the spring constant is too small however, the large deflection of the free end of the cantilever will mean that the assumptions that the magnetization of the sample is directly proportional to the change in capacitance and that the angle that the sample makes with the field is fixed may not be valid. Further, gravity or the torque from the applied quasi-static magnetic field may cause non-elastic deformations of the cantilever. For macroscopic crystals weighing approximately 50 mg with a small amount of magnetic anisotropy, a spring constant near 2 N/m provides a good compromise. On the other hand, for crystals with very strong anisotropy, it was necessary to use a sample weighing only .1 mg for the same spring constant.

To increase the capacitance, the free end of the capacitor can be widened compared to the arm of the cantilever, increasing the area of the deflected end of the capacitor. Due to the size constraints of the sample mounting area, typical dimensions of the widened end of the cantilever are 8 mm by 4.5 mm. For an example of typical sensitivity at 9 T, assume a spring constant of 2 N/m, a cantilever length of 10 mm, a measurement sensitivity of 10 aF, and equilibrium separation of 250 $\mu$m. Using a simple parallel plate capacitor model and assuming the full area of the widened end of the cantilever is deflected ($36\ mm^2$), the minimum detectable deflection would be about 2 nm. Since the torque is applied to the cantilever at the mounting point of the sample, $\tau = kl\Delta x$. The measured magnetic moment
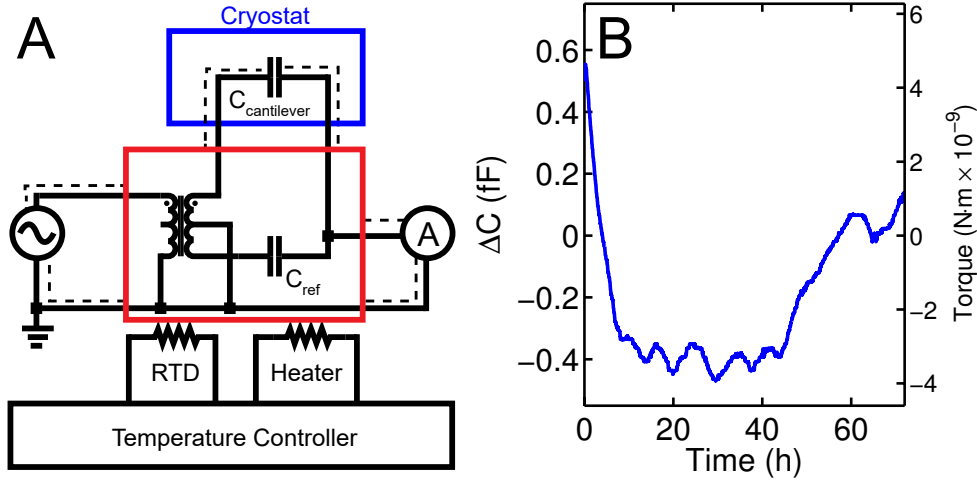
Figure 2.5: (a) Circuit schematic for the current-balance capacitance measurement. The voltage source and ammeter functions are provided by the Signal Recovery 7225 Lock-in Amplifier. It is important that the shielded cables in the cryostat extend as close to the cantilever device as possible to avoid interference from other electrical signals in the cryostat. (b) Drift in measured capacitance versus time for the balance circuit. With environmental control of the current-balance circuit, the drift per hour is less than 50 aF after the temperature control has stabilized for 8 hours. Right axis: equivalent drift in measured torque assuming typical cantilever dimensions.

of the sample is:

$$m = \frac{kl\Delta x}{B sin(\theta)} \tag{2.3}$$

$\theta$ is the angle between the magnetization and the applied field. For highly anisotropic samples, $sin(\theta)$ can be close to unity. Using the values assumed above, at 10 T the smallest detectable change in the magnetization of the sample is about $4.5 \times 10^{-9}$ emu. Depending on the size of sample and the amount of anisotropy, the sensitivity can be increased further by using a smaller spring constant for the cantilever.

**High Precision Capacitance Measurement**

As shown in fig. 2.5(a) measurement of capacitance is performed using a current-balance method.[22] An AC voltage from the lockin amplifier output is applied to an audio transformer (Triad Magnetics TY-141P). The transformer output is center-tapped, with the center tap connected to electrical ground. The transformer output then acts like two AC voltage sources, each 180 degrees out of phase with the other. The voltage from one of the transformer outputs is passed across the cantilever device, while that from the other output is passed across a balance capacitor. The output from both the cantilever and balance capacitor are then joined at a common node that is connected to ground through the current input on a lockin amplifier (or a current to voltage preamplifier). The current measured by the lockin amplifier is proportional to the capacitance difference between the cantilever device and balance capacitor. To accommodate devices with a range of capacitance, a capacitance bank was added to the balance side of the circuit instead of a single capacitor. A range of balance capacitance can be chosen by connecting the appropriate set of capacitors using jumper pins.

When measuring changes of capacitance on the order of tens of aF, great care must be taken to eliminate unwanted sources of drift. To reduce the changes in stray capacitance due to relative motion of the wires and electrical components, we designed a PCB to join the necessary components. A small drift of 50 aF/h is achieved. For comparison, in the initial attempts at performing measurement the same circuit was built but with fairly flexible 22 AWG stranded copper wire. This resulted in a much higher drift near 1 fF/h.

To reduce effects from thermal expansion, the electrical box containing the balance circuit was wrapped in an insulating material (aerogel). As shown in fig. 2.5(a), the whole box is held at a fixed temperature by attaching a temperature detector and heating element to the box inside to the insulation to provide temperature control. Temperature control was

provided using a resistive temperature controller with stability of +/- .1 °C/day. Finally, to reduce the effects of changes in relative humidity and water absorption by the PCB, the component box was partially filled with a desiccating salt.

Even though the drift was reduced to suitable levels for most measurements, residual drift on the order of 50 aF/h still exists, possibly from changes in the value of the reference capacitors (mainly due to changes in temperature) and changing stray capacitance between wires or traces in the system. NP0 capacitors have a tolerance in the temperature compensation of +/- 30ppm/°K. For a 1 pF balance capacitor, this gives a worst-case change in reference capacitance of 30 aF/°K. Thus, the drift due to changes in the value of the reference capacitance should be relatively minor.

Changes in the stray capacitances of the system from variance in the relative distance between wires or traces due to thermal expansion can have an impact on the measured capacitance. Typical capacitances between parallel traces are on the order of 10's of pF/m.[24] The stray capacitance for traces routed on top of each other between adjacent layers of a PCB is a similar order of magnitude. FR4 PCB, which was used for our capacitance balance circuit, has a coefficient of linear expansion near 13 ppm/°C for in-plane expansion. Along the z-axis, the expansion coefficient is over ten times larger. Assuming trace length of .5 m, trace width of .5 mm, and separation of 1.3 mm, the change in capacitance between parallel traces is about 40aF/°K. For a similar length of traces overlapping between layers, this effect is enhanced to near 500 aF/°K. In our completed system, the net effect of temperature drift was closer to 400 aF/°K as measured during a temperature sweep of the balance circuit near room temperature.

Even if all components and traces are perfectly fixed in relative position, there will be capacitance drift in the system due to changes in the relative permittivity of air from relative humidity or of the PCB due to water absorption. In one iteration of trying to minimize the measurement drift, it was thought that submerging the entire balance circuit in liquid

nitrogen might be a good idea because it would provide excellent thermal stability. However, the constant boiling of the nitrogen near the balance circuit due to the heat leak from the BNC cables created a mixture of liquid and gaseous nitrogen. The relative permittivity difference between liquid and gaseous nitrogen is over .4. This rapidly fluctuating change in the permittivity caused large fluctuations in the stray capacitance between different parts of the balance circuit, making measurement impossible.

The relative permittivity of moist air can be approximated as:[25]

$$\epsilon_r = 1 + \frac{211}{T}\left(P + \frac{48P_S}{T}H\right)10^{-6} \tag{2.4}$$

T is the temperature in °K, P is the pressure of the air in torr, $P_s$ is the saturation pressure of water vapor (in torr) at the given temperature and pressure, and H is the relative humidity in percent. At a temperature of 30°K, the change in capacitance per meter of parallel trace is approximately 40 aF for each percent change in relative humidity.

Typical FR4 PCB can absorb up to .15% moisture by weight. The dielectric constant of water at room temperature and low frequencies is nearly 20 times larger than the dielectric constant of the PCB. A fully saturated PCB may have a dielectric constant that is about 2% higher than a freshly baked PCB. While the absorption process is quite slow at room temperature,[26] it still may contribute to a constant drift in the measured capacitance.

It should be noted that changes in the stray capacitance to ground have negligible effect on the measured capacitance. The input impedance of the current detector in our lockin is less than 250 Ω at 1 kHz. The largest source of capacitance to ground is in the BNC cables used to connect the various components. Assuming that 10 meters of RG-58 cable are used, the total capacitance to ground would be 1 nF. Even assuming a 10 % change in capacitance to
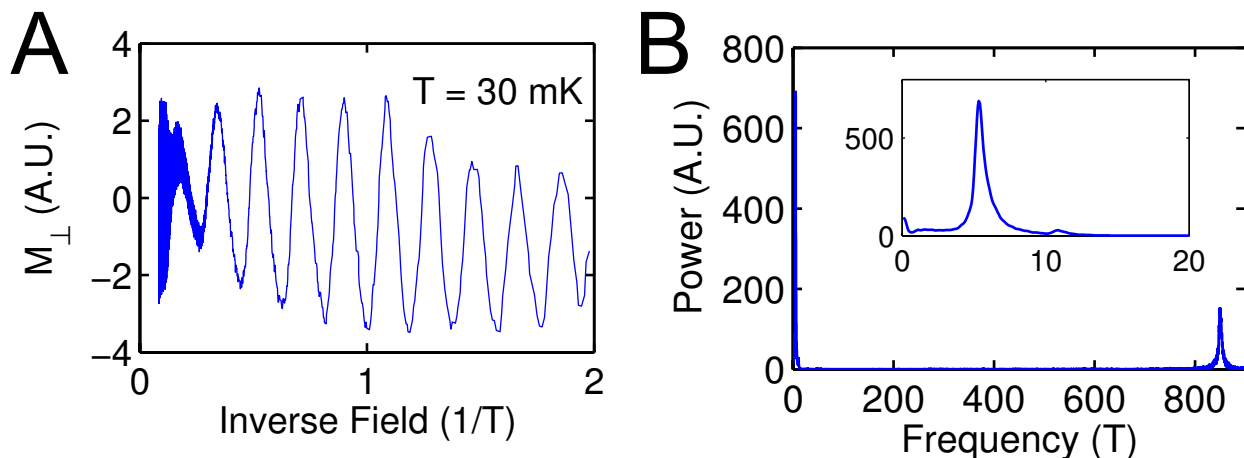
Figure 2.6: (a) Inverse field versus perpendicular magnetization for an $LaB_6$ sample. The low frequency oscillations are visible beginning at very low fields, whereas higher frequency oscillations begin at about 3 T. (b) The frequency spectrum of the oscillations in $LaB_6$. The lower frequency oscillations have a period of $.185$ $T^{-1}$; the higher frequency oscillations have a period of $1.18 \times 10^{-3}$ $T^{-1}$. Inset: A zoomed in view near the first frequency peak.

ground, a simple circuit analysis shows that the change in the measured capacitance would be less than 1 aF.

In sum, the combination of temperature and humidity controls implemented on the balance circuit and the rigidity of the wires from using a custom PCB are critical for achieving a low signal drift necessary for detecting small capacitance changes.

**Quantum Oscillations in $LaB_6$**

To test the torque magnetometry setup, the dHvA oscillations in $LaB_6$ were measured at a fixed orientation. DHvA effects are quantum oscillations in the magnetization of a material due to changes in an applied magnetic field.[27] In simplified terms, the external field limits the electronic states to a set of quantized tubes in k-space. Each tube has an area in a plane perpendicular to the magnetic field proportional to a quantum number times the magnetic field. As the field is varied, the outermost tube that is still inside the Fermi surface passes through the Fermi surface. As it does so, occupied states on that tube must relocate to

tubes still inside the Fermi surface, changing the energy of the system, which manifests as a change in the magnetization. Onsager showed that the change in magnetization (among other properties) is periodic in 1/B and is related to the extremal areas of the Fermi surface in planes perpendicular to the magnetic field as follows (in SI units):

$$\Delta(\frac{1}{B}) = \frac{2\pi e}{\hbar} \frac{1}{A_e}$$

(2.5)

$H$ is the applied magnetic field, and $A_e$ is an extremal area of the Fermi surface. This phenomenon is particularly well-suited for study via torque magnetometry because there is a torque on the sample as long as the extremal area of the Fermi surface varies with the direction of the applied field (i.e., the Fermi surface is not a sphere). We measure dHvA oscillations using the above-described capaci tively detected cantilever magnetometer while sweeping the magnetic field at a constant temperature. Fig. 2.6(a) shows the perpendicular magnetization of $LaB_6$ as the field is slowly swept from .5 T to 12 T. Low frequency oscillations are visible starting at very low fields, with higher frequency oscillations starting near 3 T. Fig. 2.6(b) shows the frequency spectrum of the change in capacitance versus inverse field. Frequency peaks occur at 5.41 T and 849 T. A slower ramping at high fields also showed a frequency peak at 3250 T. The fact that it is not possible to resolve more than one peak at 5.41 T demonstrates that the sample was mounted such that the angle between the applied field and the [100] axis of the sample was nearly zero.[28] The higher frequency oscillations also agree quite favorably with previous work at higher temperature.[29]

# Chapter 3

# CeAgBi$_2$

## 3.1 Introduction

Heavy fermion (HF) materials can exhibit many interesting physical phenomena due to the competition between Ruderman-Kittel-Kasuya-Yosida (RKKY) magnetic interactions, on-site Kondo interactions and crystalline electrical field (CEF) effects. Classic examples of fascinating properties include quantum criticality in YbRh$_2$Si$_2$,[30] unconventional super-conductivity in CeCoIn$_5$,[31] and metamagnetism in CeRu$_2$Si$_2$.[32] HF materials which host such exciting properties usually crystallize in the tetragonal structure and their ground state is on the border of antiferromagnetism (AFM). Thus, the common structural and electronic features may facilitate our search for novel materials with interesting properties.

The family of tetragonal compounds Ce$TX_2$ ($T$ = transition metal, $X$ = pnictogen) is a promising candidate in the class of 'light' heavy-fermions. Great attention has been given to the antimonide ($X$ = Sb) members due to the presence of anomalous ferromagnetism in CeAgSb$_2$[33, 34] and, more recently, due to the report of quantum criticality in the antiferro-magnetic CeAuSb$_2$ member.[35] In particular, the AFM state of CeAuSb$_2$ has been shown to

undergo two field-induced magnetic transitions before entering the polarized paramagnetic state at $H_c \sim 5$ T. Although the investigation of the Sb-based compounds is abundant, fewer reports can be found on the bismuthide ($X = $ Bi) members. For instance, CeAgBi$_2$ have been reported almost simultaneously by two different groups to be an antiferromagnet below $T_N = 6.1$ K with three field-induced magnetic transitions.[36, 37] However, a detailed analysis of the underlying interactions and a deep understanding of the phase diagram at low temperatures is still missing. In this regard, quantitative analyses have been performed in recent reports on Ce$T$Bi$_2$ ($T = $ Cu, Au), which present antiferromagnetic (AFM) ordering at $T_N = 16$ K (Cu), and 12 K (Au) [38, 39].

## 3.2 Experimental Results

The field-tuned properties of CeAgBi$_2$ were studied by means of magnetic measurements, including torque magnetometry and vibrating sample magnetometry, and through transport measurements. CeAgBi$_2$ is an intermetallic compound which crystallizes in the tetragonal ZrCuSi$_2$-type structure ($P4/nmm$) with a stacking arrangement of CeBi-Ag-CeBi-Bi layers. This compound shows a rich phase diagram as a function of applied field with five field-induced transitions at 40 mK. The transitions show signatures in both magnetization and transport. In contrast to the previous reports on the Ce$TX_2$ family, a well-defined metamagnetic transition with clear first-order character emerges at $\sim 79$ kOe in the vicinity of the transition to the paramagnetic state at $H_c \sim 84$ kOe. Another transition near 57 kOe has a large amount of hysteresis indicative of a first-order transition, but the lack of evidence of an instantaneous jump in magnetization make such a classification somewhat uncertain. While a first order character can not be ruled out for the remaining transitions (the magnetization data is quite sharp), the amount of hysteresis observed is minimal compared to the transitions at 57 and 79 kOe. Crystal field analysis indicates a small energy difference

between the field excited CEF state ($T_{CEF} \sim 19$ K) and the RKKY interaction ($T_N = 6.4$ K) indicating that, even at modest fields, the contribution from the first CEF excited state may be important. Analysis also reveal the presence of two competing anisotropic exchange interactions. Thus, the rich H-T phase diagram is likely due to this magnetic frustration along with the weak anisotropy.

Single crystals of CeAgBi$_2$ were grown from Bi-flux with starting composition Ce:Ag:Bi=1:$x_{nominal}$:8 ($1 \leq x_{nominal} \leq 3$). The mixture was placed in an alumina crucible and sealed in a quartz tube under vacuum. The sealed tube was heated up to 1050°C for 8 h and then cooled down at 10°C/h. The excess of Bi flux was removed after 24 h of annealing at 500°C by centrifugation. The single crystals with dimensions $\sim 3 \times 3 \times 0.5$ mm$^3$ were ground and their crystal structure was checked by X-ray powder diffraction experiments using Cu $K\alpha$ radiation at room temperature. Several single crystals from different batches were also submitted to elemental analysis using a commercial Energy Dispersive Spectroscopy (EDS) microprobe coupled to a FEG SEM microscope. The actual $x_{Ag}$ concentration was extracted from the EDS analysis. The precision of the analysis was calculated by $\sigma/\sqrt{N}$, where $\sigma$ is the standard deviation of the measurements, and $N$ is the number of points analyzed. Magnetization measurements were performed using a commercial superconducting quantum interference device (SQUID), down to 1.8 K. Below 1.8 K, cantilever-based torque magnetometry was used to measure the magnetization in a dilution refrigerator (see section 2.2.4). Electrical resistivity measurements were made using a low-frequency ac resistance bridge and a four-point configuration with either co-linear contacts for normal resistivity measurements or a crossed pattern for Hall resistance measurements.

Figure 3.1 shows the in-plane resistivity, $\rho(T)$, as a function of temperature down to 0.5 K at zero magnetic field. At high temperatures ($T > 200$ K), $\rho_{ab}(T)$ decreases linearly with decreasing temperature, as expected for a metallic system. As the temperature is further decreased a minimum is observed followed by $-\ln T$ behavior due to incoherent Kondo
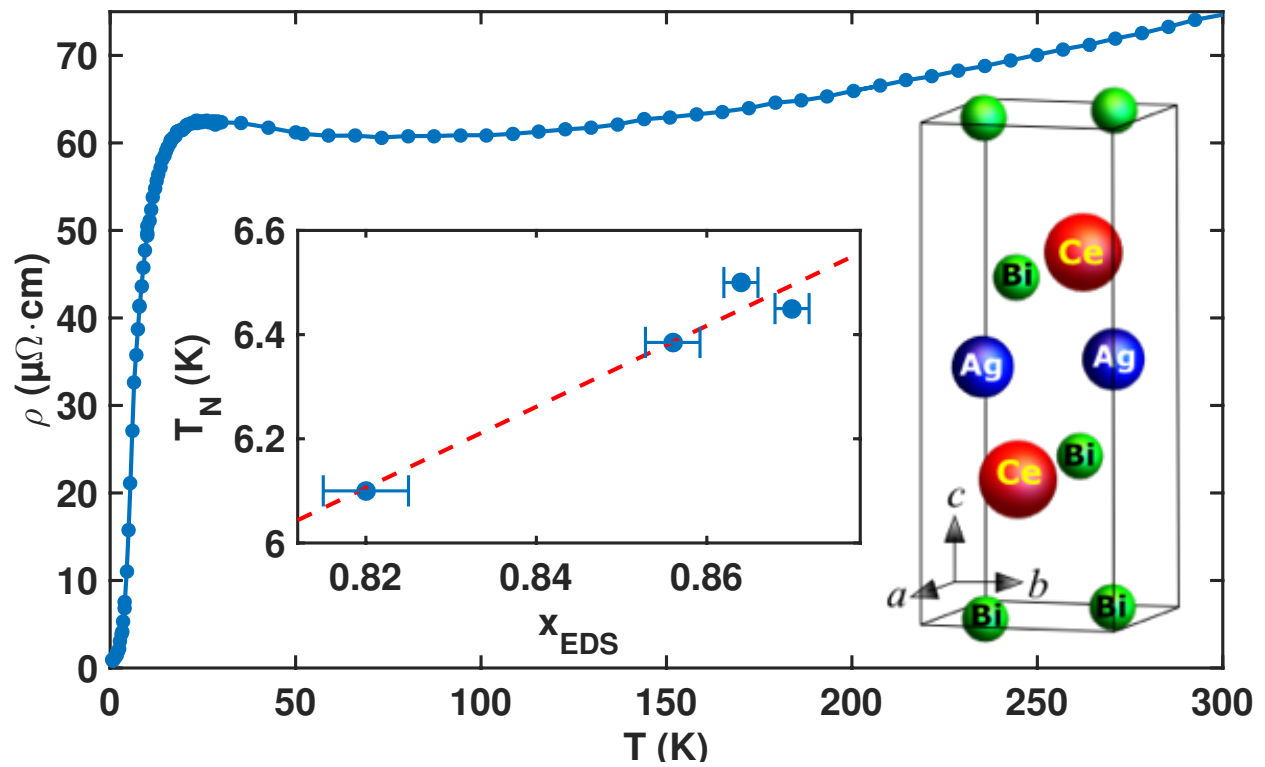
Figure 3.1: Resistivity of CeAgBi$_2$ measured in zero applied field. The inset shows the antiferromagnetic transition temperature versus measured silver concentration (the error bars signify the inhomogeneity in measured silver concentration). Finally, the diagram shows the crystal structure of CeAgBi$_2$.
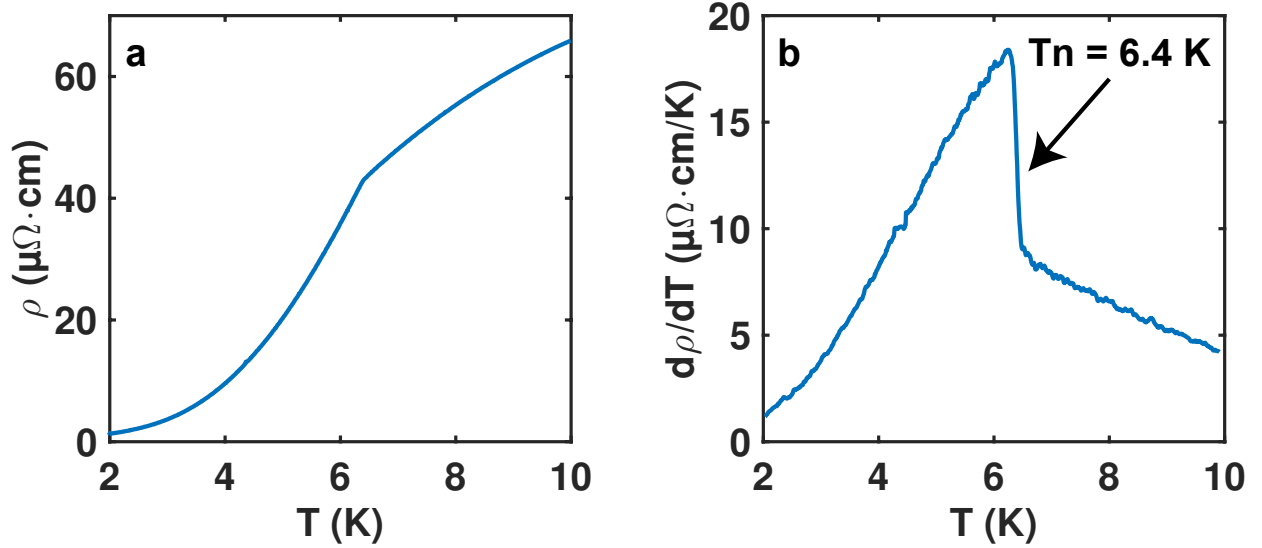
Figure 3.2: (a) Low temperature resistivity of CeAgBi$_2$ measured in zero applied field. (b) Derivative of low temperature resistivity of CeAgBi$_2$. The jump at T = 6.4 K signifies T$_N$.

scattering. Below 25 K, $\rho(T)$ drops abruptly either because the magnetic scattering becomes coherent or the first excited crystal field level becomes depopulated. A small kink is then observed at $T_N = 6.4$ K, as shown in figure 3.2(a), indicating a transition to the AFM phase. The derivative of the resistivity (3.2(b)) provides clear evidence of the AFM transition.

Compared to a previous report on CeAgBi$_2$,[36] the AFM transition occurs at .3 K higher temperature. Although this increase in $T_N$ is very small at first sight, EDS measurements revealed that it is caused by a substantial decrease in both number of vacancies and in-homogeneity at the Ag site. The inset of figure 3.1 shows the linear relation between $T_N$ and the occupation at the Ag site, $x_{EDS}$. For the most deficient samples, the transition temperature matches the ones reported in the literature, $T_N = 6.1$ K, and the Ag occupation reaches 82(4) %. For the best samples obtained so far, the occupancy reaches 87(2) %, leading to the highest transition temperature reported up to date, $T_N = 6.5$ K. It is worth noting that less deficient samples also are accompanied by higher resistance ratios and lower residual resistivity. At low temperatures, both the number of transitions and the field at which transitions occur is dependent on the silver deficiencies. Moreover, Shubnikov-de Haas
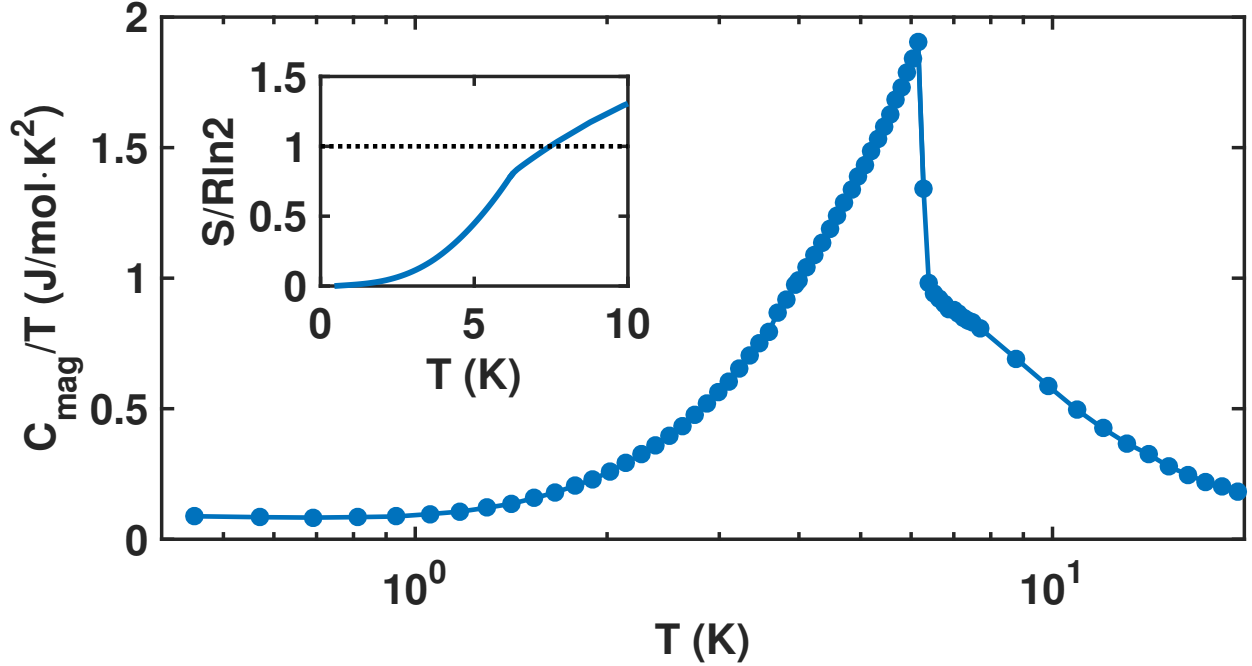
Figure 3.3: Magnetic specific heat of CeAgBi$_2$ in zero field. The non-magnetic contribution has been removed by subtracting away the specific heat of reference compound LaAgBi$_2$. Inset shows integration of specific heat divided by Rln(2). Only .83 of of Rln(2) is recovered by T$_N$.

oscillations could only be observed on the less deficient samples.

Finally, figure 3.3 shows the specific heat of CeAgBi$_2$ in zero applied field, confirming the transition to the AFM state. An integration of the specific heat shows that S/Rln(2) is less than one ($\sim$ .83) at T$_N$. This shows that either the Ce $f$-electron is partially hybridized with the conduction bands or there is some degree of magnetic frustration. It is likely that both magnetic frustration and hybridization are relevant. The electron masses as measured by dHvA oscillations were reported to be greater than 5 m$_e$ for a majority of the electron orbits, although one of the orbits had an electron mass as low as .5 m$_e$.[36] While the higher masses suggest some degree of hybridization of the Ce 4$f$ electron, the large saturated moment of nearly 2 $\mu_B$/Ce atom shows that the 4$f$ electron remains fairly localized. The large number of transitions in the $H - T$ phase diagram is strong evidence that magnetic frustration is present in CeAgBi$_2$.
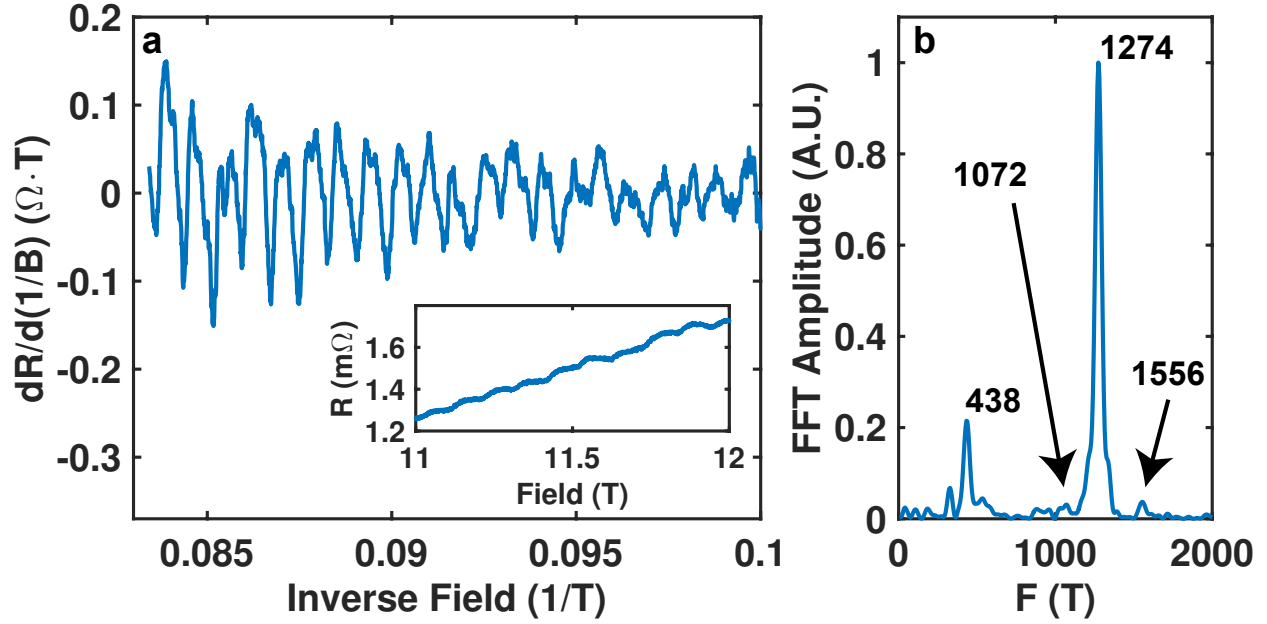
Figure 3.4: (a) Derivative of resistance of CeAgBi$_2$ plotted versus inverse field. The mixing chamber is at base temperature (30 mK), but the sample is likely above 100 mK due to the large current necessary to measure the sample. Inset show resistance versus field. (b) FFT amplitude of the oscillations. The peaks at 1072 and 1556 are marked for comparison with the literature.

As shown in figure 3.4, Shubnikov de-Haas (SdH) oscillations were observed in the resistivity of one of the measured samples, although surprisingly de-Hass van-Alphen (dHvA) were never observed. SdH oscillations were only observed in samples with lower number of silver vacancies. The scattering from the additional vacancies may have decreased the maximum temperature at which oscillations could be observed (the minimum achievable sample temperature during resistance measurement was ~100 mK due to ohmic heating). The lack of observation of dHvA oscillations may be due to the fact that torque magnetometry measurements are not ideal for measuring quantum oscillations in materials with magnetic anisotropy. Anisotropy between the c-axis and ab-plane ($\chi_{||}/\chi_{\perp} \sim 3.5$ in CeAgBi$_2$ at low temperatures) required using a small sample for torque magnetometry measurements ($\sim 100$ $\mu$g). The extremely large background signal in the torque measurement reduces the sensitivity to small, oscillatory signals. Other techniques, such as the field modulation method,[40] may be more suited to dHvA studies of crystals with magnetic anisotropy. This
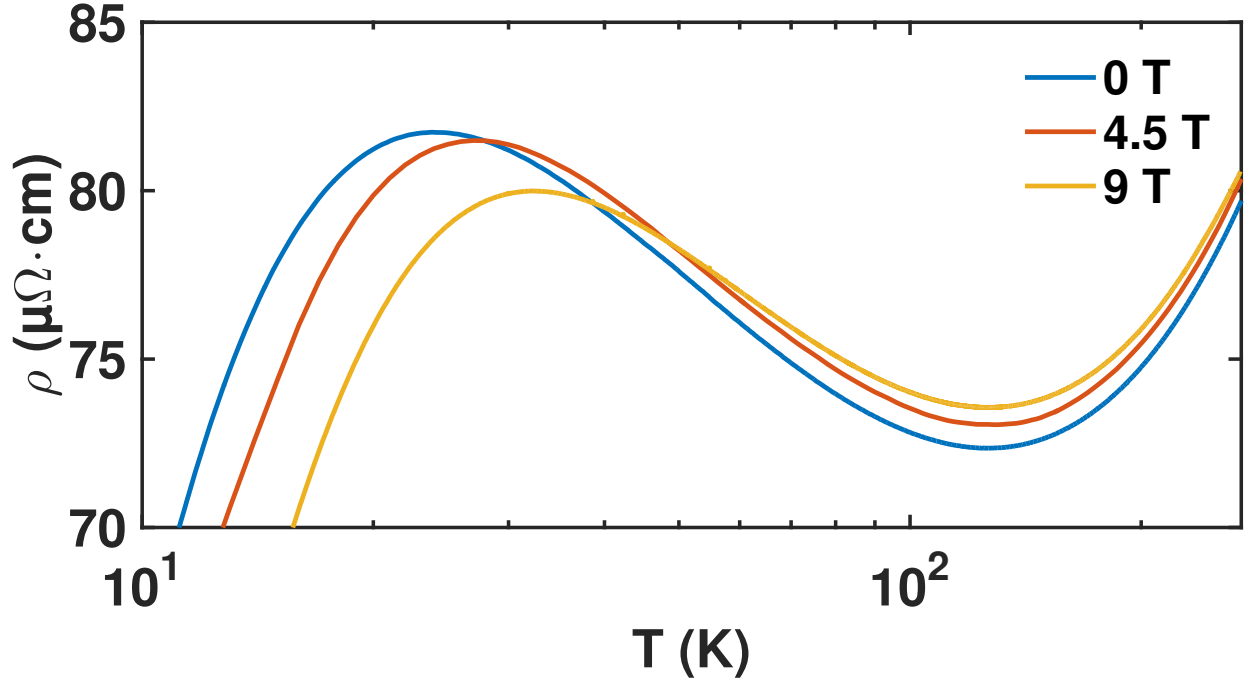
Figure 3.5: Resistivity of CeAgBi$_2$ in three different applied fields. As the field is increased, the position of the resistivity peak moves to higher temperatures.

was the technique used in previous reports of the dHvA oscillations.[36]

Attempts to determine the effective electron mass from thermal damping of the measured SdH oscillations (see section 4.2.3 for an explanation of this method) yielded electron masses nearly double that of previous reports. However, this discrepancy is most likely due to an error in the determination of the sample temperature. The current required to measure the oscillations (500 $\mu$A) would locally heat the sample much more than the thermometer located nearby on the sample stage, especially near the minimum temperature. If the sample temperature were higher than the reported temperature, it would cause the calculated effective mass to be higher than the true value.

To understand the origin of the peak in resistance near 24 K, the high-temperature resistance was measured in several different fields. The results are presented in figure 3.5. The increase in the temperature of the resistance peak as the field is increased, suggests either Kondo coherence or crystal field depopulation. Increasing the field should lead to a increase in
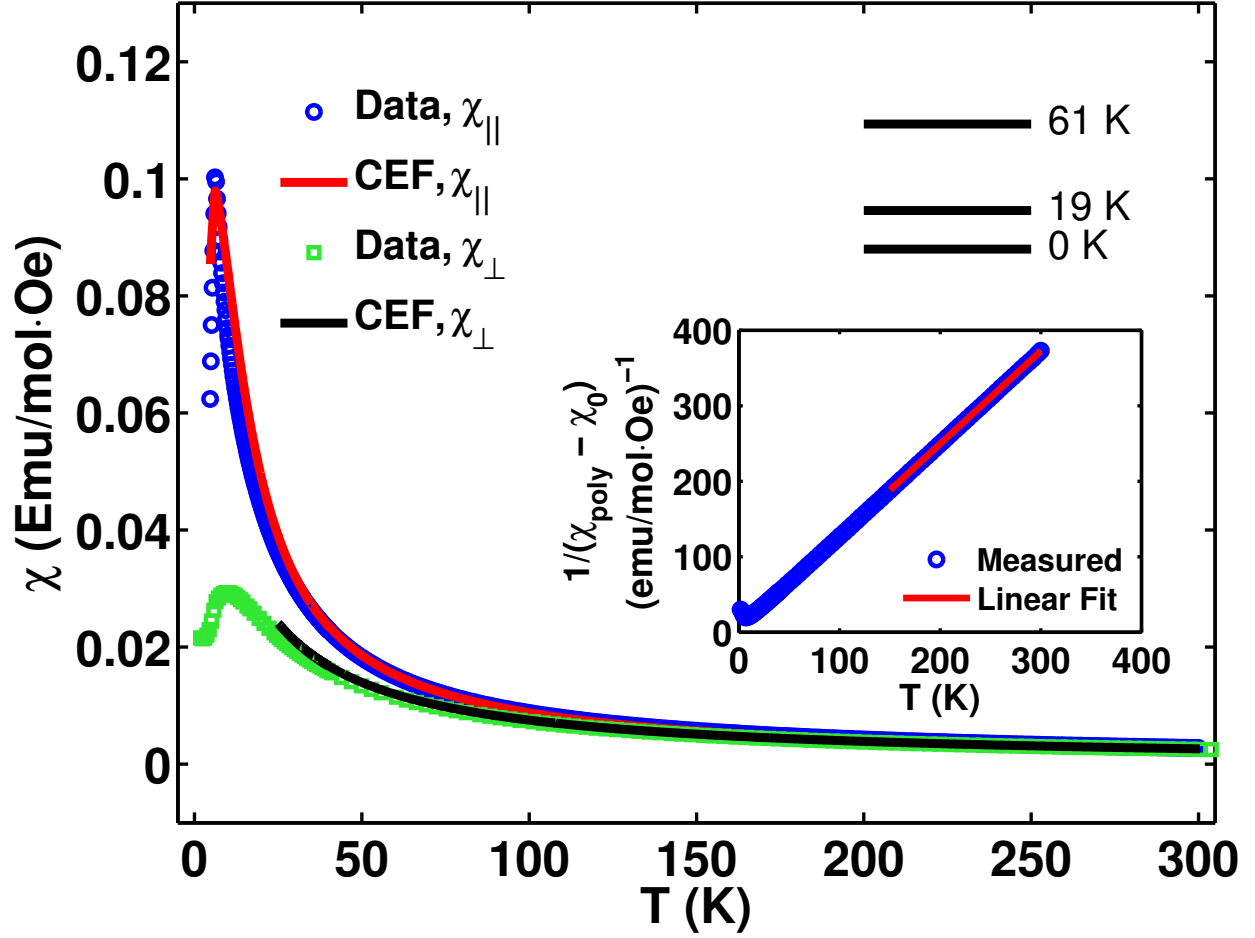
Figure 3.6: Magnetic susceptibility of CeAgBi$_2$ for fields parallel and perpendicular to the crystalline c-axis. Inset shows a fit of the high-temperature polycrystalline data to the Curie-Weiss law. The line in the upper-right represent the energy spacing between the ground state and first two excited crystal-field levels.

splitting between the lower Zeemna-split ground state and higher Zeeman-split first excited state. This in turn would lead to a raising of the temperature of the resistance peak as the field is increased. Kondo coherence could also explain the existence of the peak in resistance. As the field is increased, Kondo scattering is expected to decrease, resulting in a smaller resistance peak. Surprisingly, the relatively large magnetoresistance (MR) of over 1% at 150 K suggests that magnetism is playing a role even at high temperatures. The shift in the peak to higher temperature and lower resistivity is due to the crossover from positive to to negative MR as the temperature is lowered.

Figure 3.6 shows the temperature dependence of the magnetic susceptibility $\chi(T)$ when the magnetic field ($H = 1$ kOe) is applied parallel $\chi_\parallel$ and perpendicular $\chi_\perp$ to the crystallographic $c$-axis. At high temperatures ($T > 150$ K), $\chi(T)$ can be well fitted by a Curie-Weiss (CW) law plus a $T$-independent Pauli term, $\chi(T) = \chi_0 + C/(T - \theta_{CW})$ (solid lines). We obtain an effective moment of $\mu_{eff} \approx 2.5(1)\mu_B$ in both directions, in agreement with the theoretical value of $\mu_{eff} \approx 2.54\mu_B$ for $Ce^{3+}$ free ions. On the other hand, the $\theta$ values are anisotropic and yield to $\theta_\parallel = 5.7$ K and $\theta_\perp = -8.5$ K. In a molecular field approximation, such anisotropy indicates the presence of two effective exchange interactions with opposite signs between the $Ce^{3+}$ moments. Interestingly, it has been recently observed in $CeCuBi_2$ that the macroscopic properties could be well fit by a mean field model with tetragonal CEF only in the presence of anisotropic sign-changing RKKY interactions.[38] Thus, anisotropic exchange parameters appear to be an intrinsic property of this series of compounds. The inverse of the polycrystalline $1/\chi_{poly}(T)$ is presented in the inset of figure 3.6. A Curie-Weiss fit to this averaged data for $T > 150$ K (dashed line) yields an effective magnetic moment $\mu_{eff}$ = 2.5(1) $\mu_B$ and a paramagnetic Curie-Weiss temperature $\theta_p$ = -4K, in agreement with the AFM order at $\sim 6$ K. We note that this value of $\theta_p$ is smaller than the average value found along the antiferromagnetic series $CeTBi_2$, which may indicate that the RKKY exchange interactions are weaker in the Ag compound.

As $T$ is further lowered, we observe a sharp peak in $\chi(T)$ at the AFM ordering temperature, $T_N = 6.4$ K, along with a magnetic anisotropy consistent with an easy axis along the $c$-axis. The ratio $\chi_\perp/\chi_\parallel \approx 3.5$ at $T_N$ is mainly determined by the tetragonal CEF splitting and reflects the low-$T$ $Ce^{3+}$ single ion anisotropy. We note, however, that this ratio is smaller than what has been observed in other bismuthides, suggesting a smaller energy splitting between the CEF ground state and the first excited state. In order to confirm this hypothesis, we now analyze our data on the basis of a mean field model with anisotropic nearest-neighbor interactions plus a CEF (point charge) Hamiltonian given by $H_{CEF} = B_2^0 O_2^0 + B_4^0 O_4^0 + B_4^4 O_4^4$, where $B_i^n$ are the CEF parameters, and $O_i^n$ are the Stevens equivalent operators obtained

| CEF parameters | | | | |
| --- | --- | --- | --- | --- |
| $B_2^0$ | $B_4^0$ | $B_4^4$ | $z_{FM}J_{FM}$ | $z_{AFM}J_{AFM}$ |
| -1.78 | 0.168 | 0.71e-3 | -0.89 | 1.35 |

| Energy levels and wave functions | | | | | | |
| --- | --- | --- | --- | --- | --- | --- |
| $E(K)$ | $\lvert-5/2\rangle$ | $\lvert-3/2\rangle$ | $\lvert-1/2\rangle$ | $\lvert+1/2\rangle$ | $\lvert+3/2\rangle$ | $\lvert+5/2\rangle$ |
| 0 | 0 | -1 | 0 | 0 | 0 | 0 |
| 0 | 0 | 0 | 0 | 0 | 1 | 0 |
| 19 | 1 | 0 | 0 | 0 | 0 | 0 |
| 19 | 0 | 0 | 0 | 0 | 0 | -1 |
| 61 | 0 | 0 | -1 | 0 | 0 | 0 |
| 61 | 0 | 0 | 0 | -1 | 0 | 0 |

Table 3.1: CEF parameters (in Kelvin), energy levels, and wave functions obtained from the best fits of magnetic susceptibility data of CeAgBi$_2$ single crystals.

from the angular momentum operators.[41]

The fit that best reproduces the anisotropy and the AFM transition temperature are shown by the solid lines in figure 3.6. The extracted CEF parameters, exchange interactions, and the corresponding eigenvalues and eigenfunctions are displayed in table 3.1. As expected, two RKKY parameters with opposite signs but similar amplitudes are found, suggesting a strong competition between FM and AFM ground states. The fitting yields an AFM coupling between planes ($z_{AFM} * J_{RKKY} = 1.35$ along the c-axis) and a FM coupling in the ab-plane ($z_{FM} * J_{RKKY} = -0.89$), with the antiferromagnetic interaction dominating. Furthermore, it becomes clear that the smaller anisotropy in $\chi$, as compared to other bismuthides, is a reflection of the smaller value of $B_{20}$, which in turn gives rise to a small overall splitting of $\sim 60$ K. In addition, the first excited state sets the rather small CEF energy scale of $\Delta_{CEF} = 19$ K. Although the anisotropy between $\chi_{\parallel}$ and $\chi_{\perp}$ is well reproduced by our simple theoretical model, the single ion CEF effect is not able to capture the field-induced transitions in M(H), which is not surprising.

### 3.2.1 Magnetic Transitions

CeAgBi$_2$ has an $H - T$ phase diagram with a total of 5 transitions leading to the paramagnetic phase at 84 kOe. The magnetization of CeAgBi$_2$ was measured at 40 mK using torque magnetometry, as shown in figure 3.7. The transverse magnetoresistance (MR) is simultaneously plotted with the magnetization, showing that at each magnetic transition there is a corresponding feature in transport. This indicates strong Kondo coupling between the Ce magnetic moments and itinerant $p$-electrons from Bi. Before the 84 kOe transition the overall trend of MR is linear, a feature shared with the (non-magnetic) compounds LaAgBi$_2$ and LaAgSb$_2$, where it is attributed to an underlying Dirac dispersion for Bi/Sb itinerant electrons.[42, 43] Above the 84 kOe transition, there is a change in the slope of this trend. As the field is increased to 120 kOe, the trend becomes quadratic (not shown), suggesting a Fermi-liquid region. Also, the magnetization is saturated, with a saturation value just below 1.9 $\mu_B$/Ce atom. This is slightly lower than the saturation value of 2.1 $\mu_B$/Ce previously reported,[36] and may be due to a non-linearity between the deflection of the cantilever and the corresponding change in capacitance (see section 2.2.4). Five field-induced transitions are observed at 34, 37, 54, 78, and 84 kOe as the field is swept from zero field up to 120 kOe.

Interestingly, the transition near 79 kOe appears to be strongly first-order, as shown in figure 3.8. First, as the temperature is lowered from 500 mK to 35 mK, one can observe a clear sharpening of the transition to a step-like increase at the lowest temperature, as expected from a first-order transition. Secondly, hysteresis loops show a clear difference of $\sim$4 kOe at this transition (inset of figure 3.8). Hysteresis loops also show a large difference ($\sim$2.5 kOe) at the transition centered near 54 kOe. However, the change in magnetization is less abrupt, which may be an indication that the observed hysteresis is due to pinning of defects. In fact, a small amount of hysteresis (on the order of a hundred gauss) was also observed in magnetization and transport at the remaining three transitions.

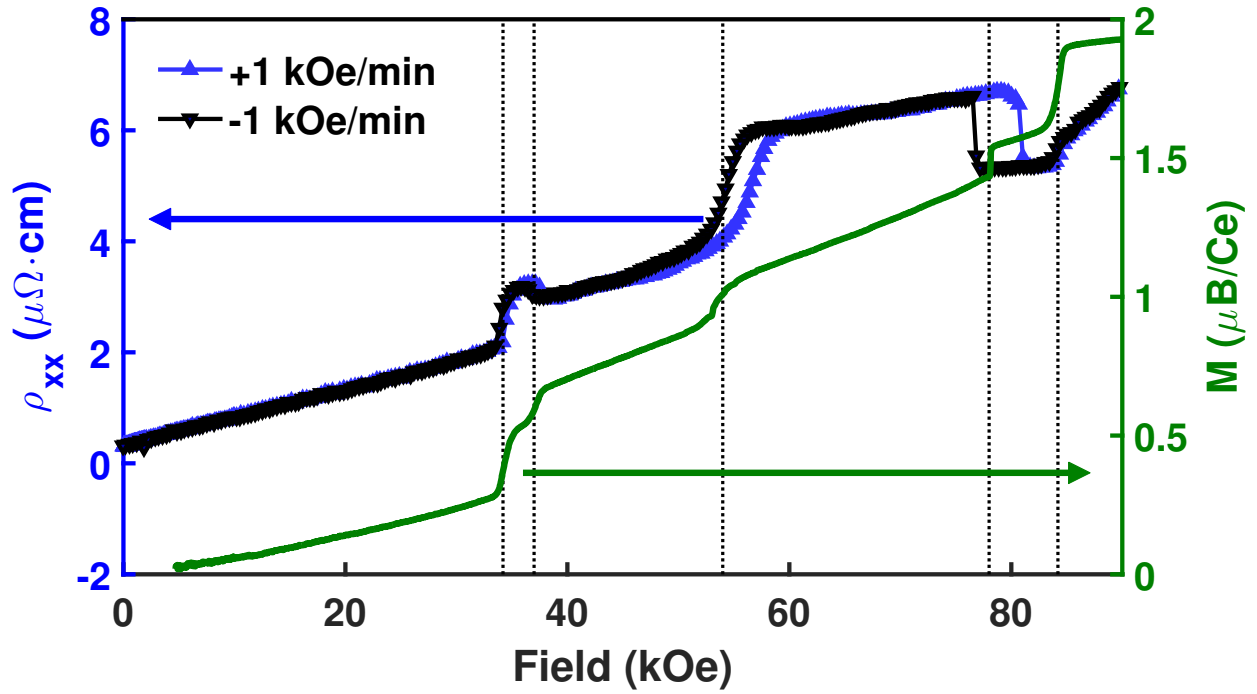Figure 3.7: Resistivity and magnetization of CeAgBi$_2$ measured at 100 mK. The resistivity is for both increasing (light blue) and decreasing fields (dark blue).
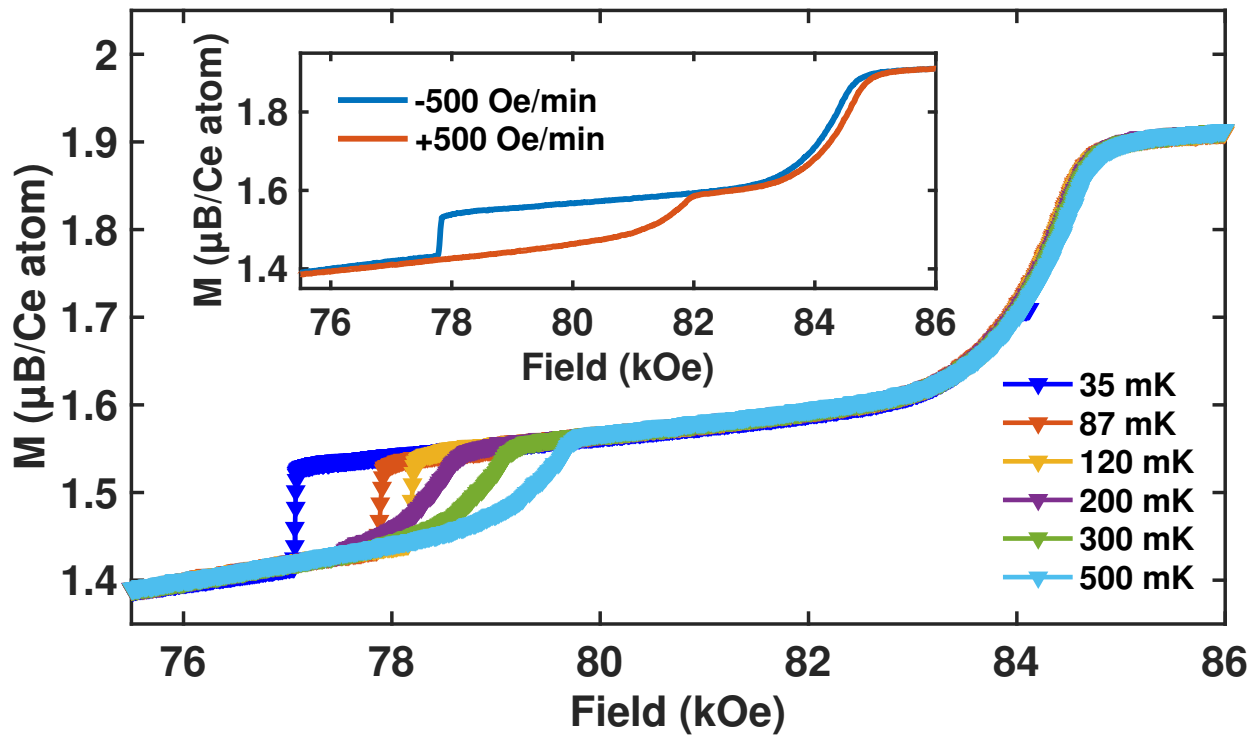


Figure 3.8: Magnetization versus field for decreasing field sweeps (500 Oe/s). As the temperature is lowered, the transition becomes sharper and moves to lower fields. Inset shows a comparison between sweeping the field up and down near 87 mK.

In many heavy fermion materials, an applied field continuously reduces the AFM ordering temperature to zero, resulting in a quantum critical point (e.g., $YbRh_2Si_2$[30], YbAgGe[44–46], CeCoIn5[47], and most similarly $CeAuSb_2$[35]). If this trend was followed in $CeAgBi_2$ the transition at $\sim 84$ kOe is, by all means, expected to be second order. Instead, a small amount of irreversibility is observed. Nevertheless, the difference of $\sim$150 Oe in the peak position of the first derivative of M versus field when the temperature is very small. While unlikely, this difference could be attributed to the time constant of the lock-in amplifier or an error in the measurement of the field. As this transition is clearly not strongly first-order, the slight amount of irreversibility is likely attributed to magnetic pinning due to crystallographic defects due to the inherent silver deficiency. Even so, due to several unfortunate properties (e.g., resistance upturn, low energy level of first excited state), it has not been possible to collect evidence as to whether the transition to the paramagnetic region at 84 kOe is a quantum critical point (see section 3.2.2).

Motivated by the evidence for coupling of itinerant electrons and local moments, we performed measurements of the Hall resistivity $\rho_{xy}$ to further elucidate the nature of the different phases. Like the MR, the Hall effect tracks each transition (figure 3.9). The decrease in $\rho_{xy}$ roughly parallels the increase in magnetization over the first two transitions, but then sharply deviates from this trend as the field is increased across the trio of transitions at 57, 78, and 84 kOe, even changing its sign between $\sim 60 - 80$ kOe.

In general, the Hall resistivity can be written as a combination of the normal Hall effect and the anomalous Hall effect:

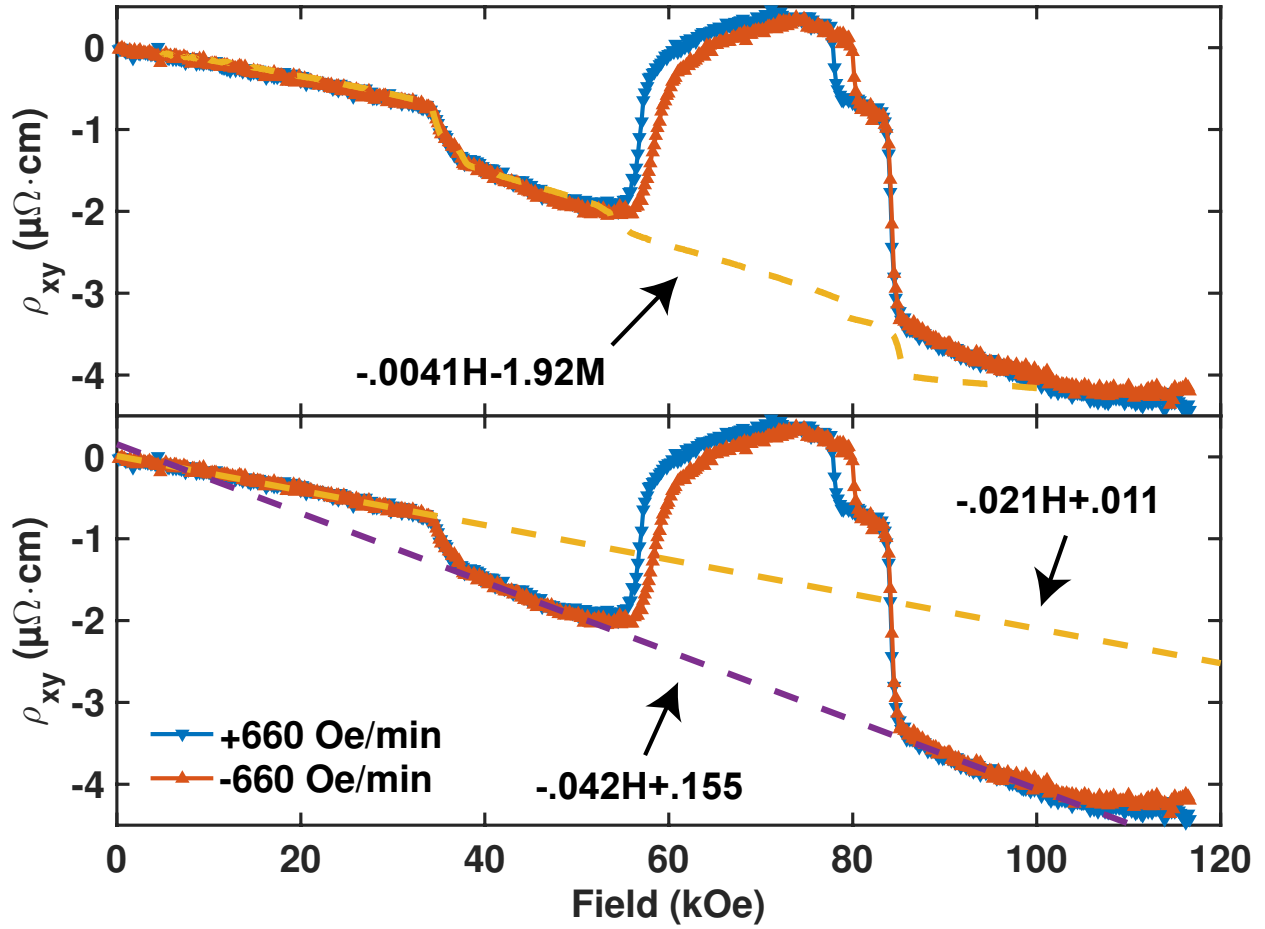$$\rho_{xy} = R_0 H + R_S M \tag{3.1}$$

Figure 3.9: Hall resistivity $[(\rho_{xy}(H > 0) - \rho_{xy}(H < 0))/2]$ of CeAgBi$_2$ at 100 mK. In the upper panel, the first 30 kOe of the data was fit assuming an anomalous Hall contribution $\rho_{xy} = R_0 H + R_S M$, where H is in kOe and M is in $\mu_B$/Ce atom. In the lower panel, the data was fit assuming the anomalous Hall contribution is zero.

Where $R_0$ is the ordinary Hall contribution, $H$ is the applied field, $R_S$ is the anomalous Hall contribution, and $M$ is the magnetization.[48] The anomalous Hall effect (AHE) can arise from asymmetric scattering from a magnetic impurity (skew scattering),[49] a side-jump scattering mechanism,[50] or due to a non-zero Berry phase.[51] Assuming a simple one band model and only ordinary Hall effect contributions, the Hall resistivity can provide information about the carrier concentration via the following relation:

$$\frac{V_H t}{IB} = \frac{-1}{ne} \tag{3.2}$$

There are two ways to interpret the Hall data, although neither is sufficient to explain the region between 54 and 84 kOe. The first approach is to fit the Hall resistivity to the standard form $\rho_{xy}(H) = R_0 H + R_S M$ that includes Hall effect contributions from both the applied field and the induced magnetization. Using the data up to $H \lesssim 38$ kOe to obtain the fit parameters, this model fits the data extremely well for low fields $H \lesssim 54$ kOe, whereupon the measured $\rho_{xy}$ strongly deviates from the expectation based on the low field fit. While there is still some discrepancy between the fit and the data after the last transition ($H \gtrsim 84$ kOe), this is relatively small compared to the much larger deviation between fit and data in the regime 54 kOe $\lesssim H \lesssim 84$ kOe. With this approach the AHE contribution is the dominant contribution. Generally, the AHE is minimal in heavy fermion systems, especially far below the coherence temperature.[48] In more deficient samples (with higher residual resistivity and $T_N$), evidence of the magnetic transitions is far less visible in the Hall resistivity. This suggests that skew scattering and side-jump scattering are not responsible for the observed features in the Hall resistivity, leaving only Berry phase contributions.

The other approach is to perform a polynomial fit on the data between no applied field and the first transition (F1), and between the second transition and the third transition (F2).
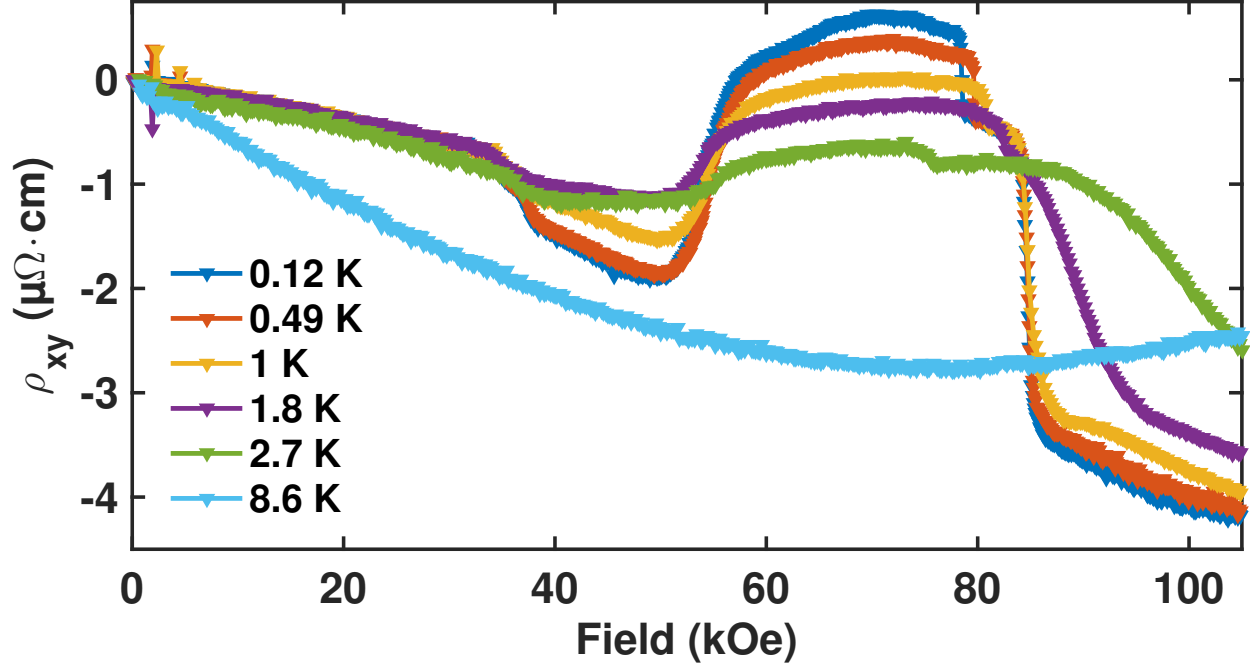
Figure 3.10: Temperature dependence of the Hall resistivity of CeAgBi$_2$.

The fit F2 matches the data above 84 kOe quite well up least up to 105 kOe. Interestingly, the slope of the fit doubles after the first transition. Under the assumption of a single band model, this corresponds to a reduction in the number of carriers by a factor of two (the slope is proportional to $\rho_{xy}/B$). At the same time, the transverse resistivity (figure 3.7) shows a jump between the first and third transition. A reduction by a factor of two could occur if somehow there was a spin-dependent splitting of the majority conduction band, and one of the bands became gapped. The matching of the slope to the high field region may just be a coincidence; the transverse resistance in the paramagnetic regime has a very different character than in the AFM regime.

Further measurements would be needed to determine whether the AHE contribution, a carrier density reduction in a specific band, or multi-band effects is responsible for the Hall behavior below 54 kOe. The mechanism for the behavior between 54 and 84 kOe is also unclear. If the main source of the jump is the anomalous Hall term, then it could signify an abrupt change in the Berry phase. On the other hand, the jump may signify a change

40
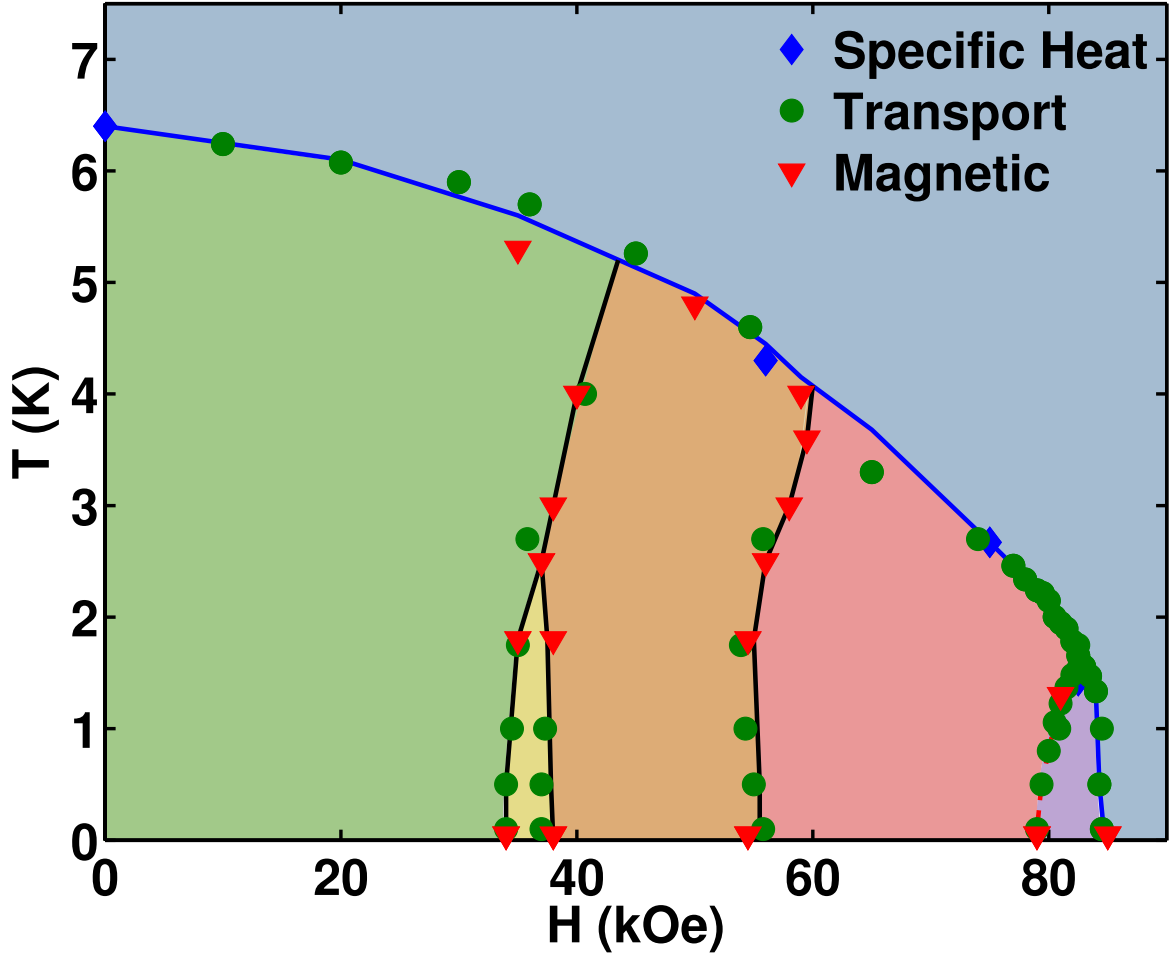
Figure 3.11: Low-temperature phase diagram of CeAgBi$_2$.

of the dominant charge carrier from electrons to holes. The increase of transverse resistivity in the same regions suggests a reduction of electron carriers instead of a sudden increase in the number of hole carriers. Prior dHvA measurements in the paramagnetic region revealed a Fermi surface similar to LaAgSb$_2$ which has both hole and electron pockets.[36] Since the Ce $f$-electron is fairly well localized in CeAgBi$_2$ a similar band structure is likely here. As the temperature is raised, the magnitude of the anomaly in $\rho_{xy}$ near 54 kOe is decreased, as shown in figure 3.10. Finally, while the Hall resistivity reveals an additional deviation from linear behavior of $\rho_{xy}$ above $\sim 110$ kOe, a previous study on lower-quality samples using pulsed fields up to 400 kOe [36] appears to rule out an additional transition.

Figure 3.11 is a compilation of specific heat, transport, and magnetic measurements into a low-temperature $H - T$ phase diagram. At temperatures above 3 K, there are only 3 transitions as the field is swept from 0 to beyond 70 kOe. Near 2.5 K, the transition at 37 kOe bifurcates. At about 1.8 K, there is a bifurcation of the AFM to paramagnetic transition line. The lower field bifurcation displays very strong first order behavior. The transition line that wanders between 60 and 54 kOe also displays a large amount of hysteresis and may also be first order. Near 0 K, there are five transitions at 34, 37, 54, 78, and 84 kOe. Finally, the Hall resistivity between 54 and 84 kOe displays a large anomaly, even changing signs below about 500 mK. This rich phase diagram likely arises from magnetic frustration.

## 3.2.2   Search for Quantum Criticality

In many heavy fermion compounds, the continuous suppression of the AFM ordering temperature to 0 K by application of magnetic field results in a quantum critical point (QCP).[30, 35, 44, 47] One signature of a QCP at the critical field is a logarithmic increase in $C_e(T)/T$. In the paramagnetic region above the critical field, Fermi-liquid behavior is typically observed with $\rho \propto AT^2$ and a constant Sommerfeld coefficient at low temperatures ($C_e/T = \gamma + \beta T^2$). Both $\gamma^2$ and $A$ are expected to diverge as $1/(H - H_c)$ when the critical field is approached from above.[35] Unfortunately, a Schottky anomaly from the first excited CEF level at 19 K obscured whether there is a logarithmic increase in $C_e(T)/T$ at 84 kOe. The specific heat does show hints of a logarithmic divergence, but only over a very limited temperature range.

Initially, much effort was spent collecting $\rho$ versus temperature curves in an attempt to demonstrate the expected divergence of the $A$ coefficient. As the sample quality improved, it became clear that this approach would not be viable. Figure 3.12 shows that as the temperature is decreased, there is an upturn in the resistivity. Such an upturn has also been previously observed in heavy fermion compounds $UPt_3$ and $CeCoIn_5$.[47, 52] In analyzing
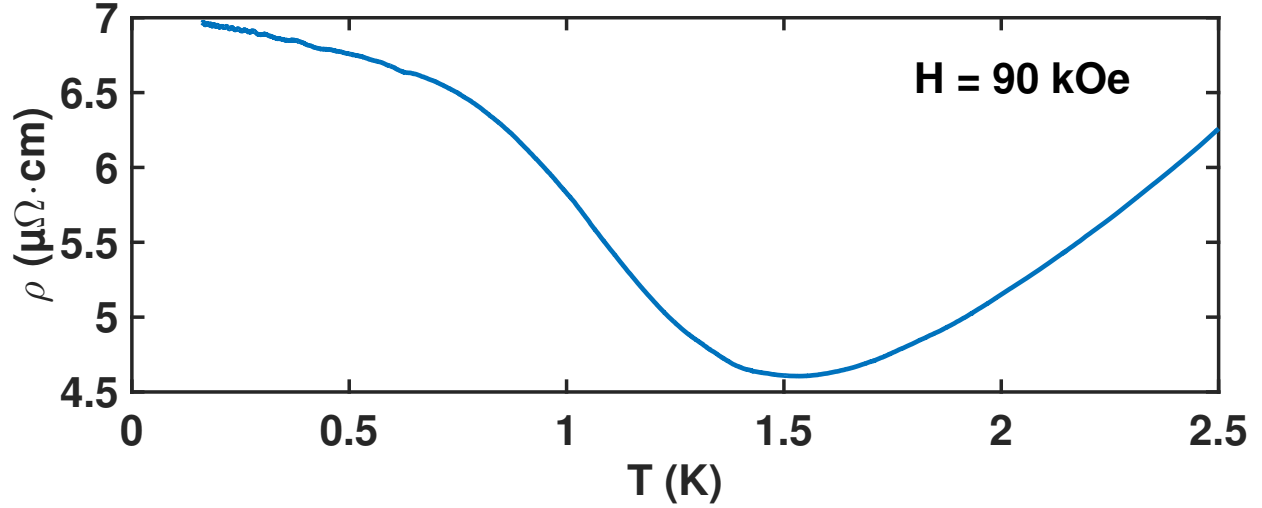
Figure 3.12: Resistivity versus temperature of CeAgBi$_2$ at 90 kOe.

CeCoIn$_5$, even though there was an upturn, it was possible for the authors of that paper to isolate a region with a $T^2$ temperature dependence and show the expected divergence in the $A$ coefficient. However, it was not possible to perform a similar analysis with CeAgBi$_2$. Attempts to isolate a temperature region with T$^2$ dependence were ultimately unsuccessful, due to the fact that the temperature dependence never seemed to include a region with a constant exponent. The origin of the resistance upturn will be speculated upon later.

Another option is to consider the Sommerfeld coefficient ($\gamma$) in the electronic specific heat. As mentioned above, $\gamma^2$ is expected to diverge as $1/(H - H_c)$ when the critical field is approached from above.[35] In the Fermi liquid regime, the specific heat over temperature should be $C/T = \gamma + \beta T^2$. A plot of $C/T$ versus $T^2$ should be linear, with the extrapolated y-intercept giving $\gamma$. Figure 3.13(b) shows $C/T$ versus $T^2$ for two different fields–one that is close to the final transition (84 kOe) and one that is further away (86 kOe). The lack of linearity in $C/T$ versus $T^2$ complicates the determination of $\gamma$ and $\beta$. Further away from the final transition (higher fields), it appears that change in $C/T$ between the lowest temperature and second lowest temperature is relatively modest. Of course, due to the limited number of temperatures measured, it is hard to be certain of the importance of this trend. Nonetheless, $C/T$ at a fixed (low) temperature may be used as a first approximation for $\gamma$. Approximating
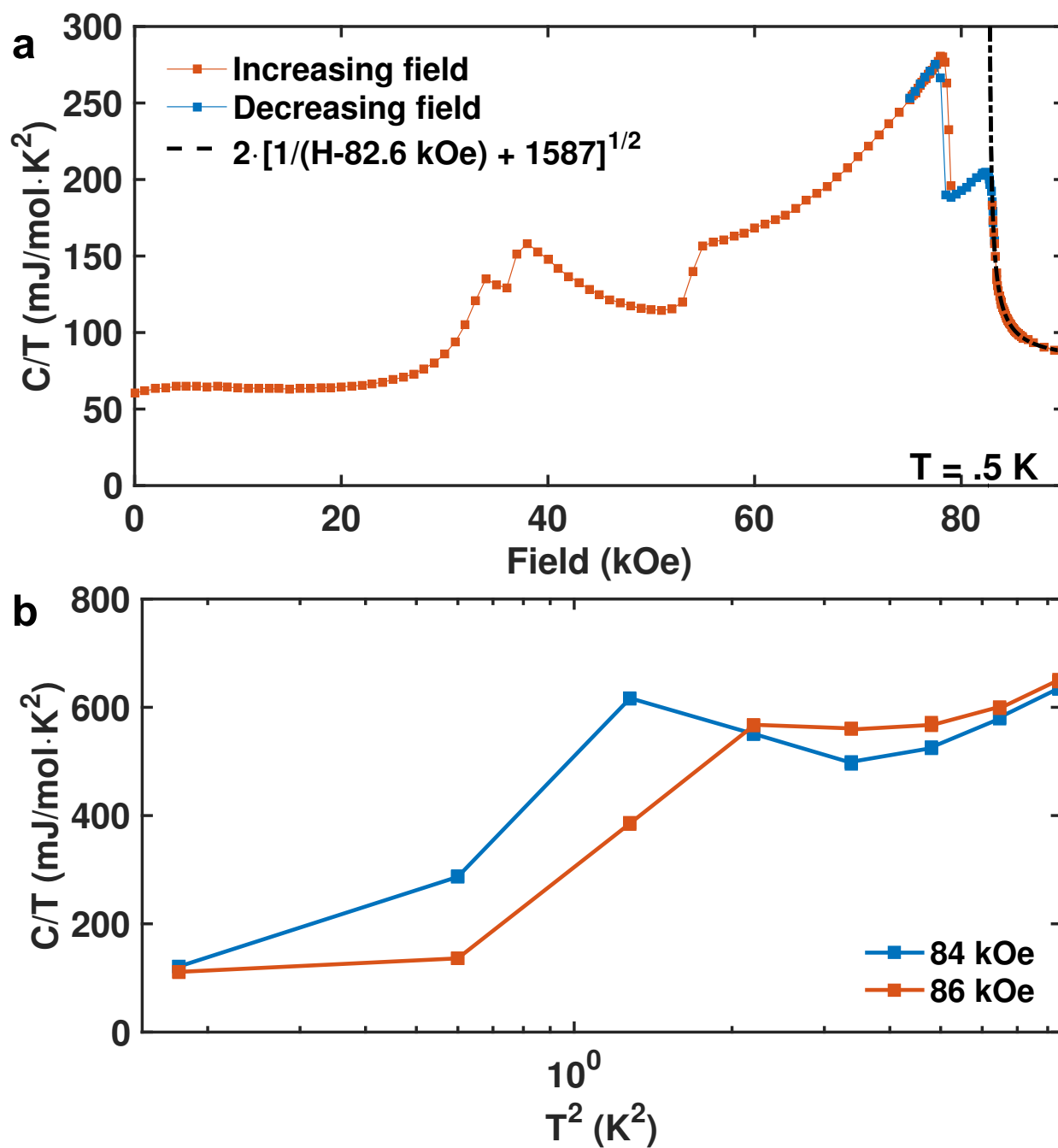
Figure 3.13: (a) Specific heat over temperature versus field of CeAgBi$_2$ at .5 K. (b) Specific heat over temperature versus temperature squared of CeAgBi$_2$ at several different fields.

$\gamma$ as $C/T$ at a fixed temperature may be less valid near the transition.

Figure 3.13(a) shows a plot of the specific heat over temperature at 500 mK plotted versus field. Evidence of all 5 transitions is visible as either a jump (37 kOe, 54 kOe, and 79 kOe) or a kink in $C/T$ (34 kOe and 83 kOe). As with transport and magnetization, the transition near 79 kOe shows hysteresis when comparing an increasing versus decreasing field sweep direction. The dashed line is a fit to the high field region with the form $\sqrt{A/(H-H_C)+B}$, yielding a critical field of 82.6 kOe. The fit is fairly close, although it starts to deviate as the field gets nearer to the critical field. This is expected because using $C/T$ at a fixed temperature as a proxy for $\gamma$ becomes less valid (or requires going to lower temperature) near the critical field. One problem with the fit, calling to question whether the final transition is a true quantum critical point, is that it requires the use of the additive constant $B$. It is not clear what might contribute to this "background" heat capacity.

Finally, while unsuccessfully trying to measure the $A^2$ term of the supposedly Fermi liquid state, an interesting trend in the resistivity upturn was noticed. As mentioned above, a similar resistivity upturn had previously been seen in $UPt_3$ and $CeCoIn_5$. On the study on $UPt_3$, it was attributed to the fact that the low temperature magnetoresistance is governed by features of the Fermi surface because the condition $\omega_c\tau \gtrsim 1$ is satisfied.[52] A similar claim was made in the study of $CeCoIn_5$.[47] In samples of $CeAgBi_2$ with higher amounts of silver vacancies, no resistance upturn was observed. Instead, the temperature dependence of the resistivity started to deviate from $T^2$ as the temperature was lowered, approaching a value of $T^3$. This suggests that a non-Fermi liquid temperature dependence (with exponent greater than 2) may be due to the fact that the sample is approaching the limit $\omega_c\tau \gtrsim 1$, but doesn't reach it due to disorder. Exponents greater than 2 in the paramagnetic (PM) regime were observed in two other Ce-based compounds ($CeAuSb_2$ and $CeNiGe_3$), one of which claimed a QCP at the AFM to PM transition (the authors of the $CeNiGe_3$ report did not, despite a fairly similar phase diagram).[35, 53] Compared to samples with more silver vacancies,
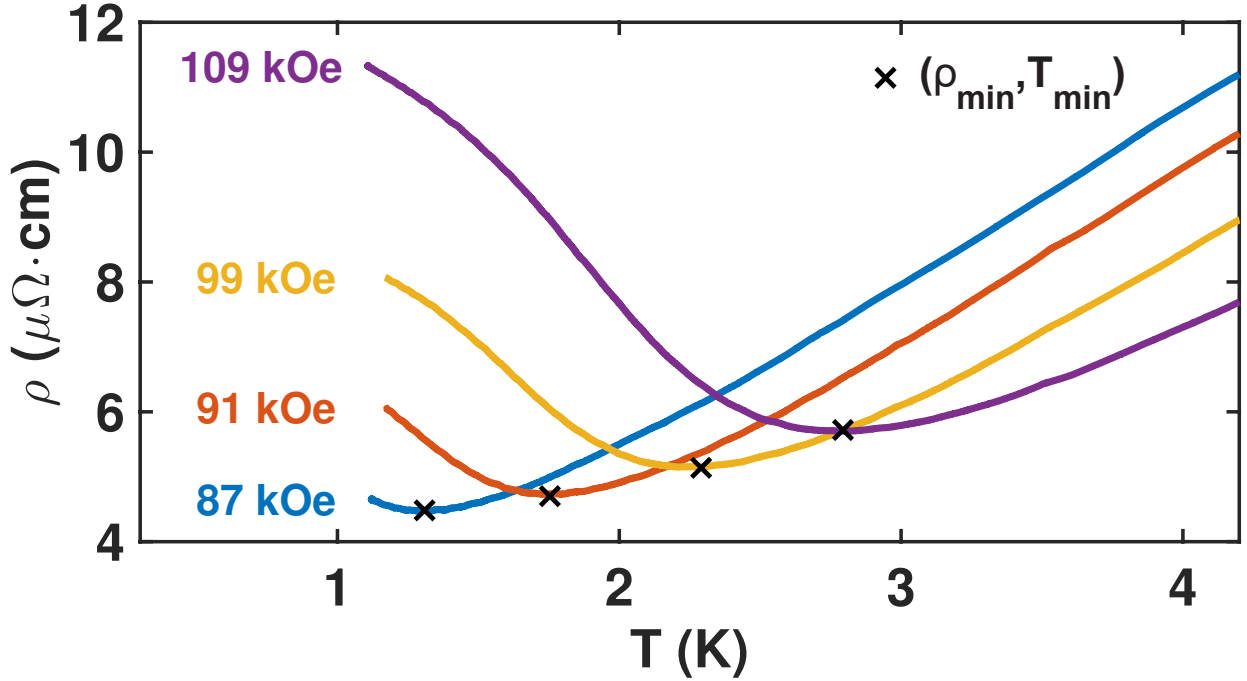
Figure 3.14: Resistivity versus temperature of CeAgBi$_2$ showing the upturn at high fields. As the field is increased, both the minimum value of $\rho$ and the temperature at which the minimum occurs also increased. For a given field, the minimum occurs at a point defined by three parameters $(\rho_{\mathrm{min}}, T_{\mathrm{min}}, H_{applied})$.

the highest quality CeAgBi$_2$ samples demonstrated both a resistance upturn and quantum oscillations in magnetoresistance (SdH). The observation of SdH oscillations requires $\omega_c \tau > 1$, so the condition $\omega_c \tau \gtrsim 1$ is clearly met. It is possible that with higher quality samples (or lower temperatures) a resistivity upturn might also be observed in CeAuSb$_2$ and CeNiGe$_3$. CeAuSb$_2$, like CeAgBi$_2$, is known to suffer from deficiencies on the transition metal site. The value for T$_N$ reported in the Balicas study was 6 K,[35] but samples with T$_N$ as high as 7 K have been grown. It may be interesting to see whether a similar resistance upturn can be observed in higher quality samples of CeAuSb$_2$.

Figure 3.14 shows a series of resistivity versus temperature curves measured in 4 different magnetic fields. The observation of the resistivity minimum allows for the definition of unique point (H, $\rho_{\mathrm{min}}$, T$_{\mathrm{min}}$) determined by the applied field, the minimum value of resistance, and the temperature at which the minimum value of the resistance occurs. Figure 3.15(a) shows
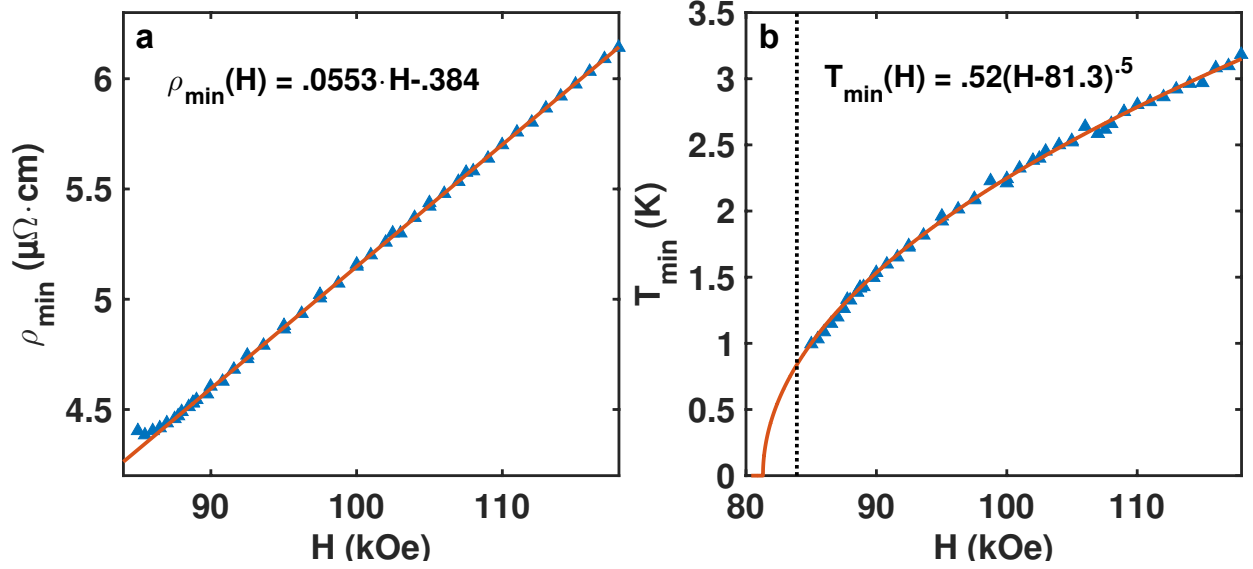
Figure 3.15: (a) Field dependence of $\rho_{\min}$. The red line is a linear fit to the data. (b) Field dependence of $T_{\min}$. The red line is a fit to the data of the form $T_{\min} = A\sqrt{H_{applied} - B}$. The dashed line shows the location of the last magnetic transition, which was measured at 83.9 kOe in this particular sample.

that $\rho_{\min}$ plotted versus field gives a remarkably linear fit. The linearity may be due to the fact that resistivity upturn is governed by the cyclotron frequency ($\omega_c$) which is linear in the applied field. As the field is increased, the crossover from Fermi liquid to Fermi surface governed behavior is also linear in applied field. The relation between the temperature at which the minimum occurs ($T_{\min}$) and applied field follows directly from the expected Fermi-liquid behavior of the resistance before the upturn. The fact that $\rho \propto T^2$ implies that $\rho_{\min} \propto T^2_{\min}$. Figure 3.14(b) shows a fit of the temperature at which the minimum occurs versus applied field. The dashed line represents the AFM to PM transition. The x-intercept occurring at a field below this transition may be related to the bicritical point observed in the phase diagram where the first order transition splits off the the AFM to PM transition (see figure 3.11). This suggests that CeAgBi$_2$ might be similar to YbAgGe where quantum criticality was observed near the bicritical point in the phase diagram.[46]

While the functional relationship between the onset of the upturn and applied field seems established, the temperature dependence of the upturn is not yet understood. The upturn

is related to the Fermi surface, but the features of the Fermi surface topology that cause an increase in resistance as the temperature is lowered are unknown. It may require classification of more systems with a similar low temperature resistivity to identify the underlying physics.

# Chapter 4

# SmB$_6$

## 4.1 Introduction

SmB$_6$ is a member of the class of materials known as Kondo insulators. Unlike in heavy fermion metals, the scattering from the heavy $f$-electrons becomes coherent and leads to a filled heavy electron band where the Fermi level sits in the middle of the narrow insulating gap of order T$_K$. SmB$_6$ was studied as early as 1969, in which it was observed that transport showed activated resistance behavior ($\rho \propto e^{\Delta/T}$). During the initial study, it was mentioned that the resistance increase saturates near 3 K. At this time, the saturation was attributed to either another conduction mechanism or trace impurities in the sample.[54]

In the late 2000's, several groups of theorists predicted a new class of materials known as 3d topological insulators.[55–57] The first direct experimental observation of a 3d topological insulator occurred in 2008 in Bi$_{0.9}$Sb$_{0.1}$.[58] Topological insulators have attracted great attention due to their promise for the realization of interesting physics, including Majorana fermions and the resulting opportunity for quantum computing. However, so far unambiguous proof of the realization of Majorana fermions in such systems has not been observed.[59]

One of the problems with the current set of topological insulators is that the bulk tends to not be a true insulator. Work has been underway to find new materials that have the topologically protected surface state but also have a bulk with a large bandgap. Most of the previous candidate materials have not been strongly correlated systems.[60] The search for an ideal system has not been easy. For example, one of the most promising materials ($Bi_2Se_3$), has residual conductivity in the bulk (presumably due to Se vacancies) and requires that the Fermi level be tuned so that is it closer to the surface Dirac point.[61]

In 2010, it was proposed that some Kondo insulators may also be topological insulators.[8] In particular, both $SmB_6$ and $Ce_3Bi_4Pt_3$ were singled out. This prediction cast the resistance saturation of $SmB_6$ in a new light. Much effort has been spent in determining whether $SmB_6$ is in the same topological class as the previously studied $Bi_{1-x}Sb_x$, $Bi_2Se_3$, and other well-known topological insulators. Direct evidence could be obtained by imaging the spin-texture of any observed surface states. However, the small hybridization gap in $SmB_6$ (10 mev) prevents the use of angle-resolved photoemission spectroscopy capable of imaging the spin.[62] The following chapter presents evidence of the existence of the surface state and other studies that have been performed to try to probe its nature.

## 4.2   Experimental Results

### 4.2.1   Surface Conduction

One of the most basic properties of a topological insulator is that there must be topologically protected metallic surface states. Thus, a necessary (but by no means sufficient) requirement for a topological insulator is the existence of a conducting surface. In $SmB_6$, unlike in several of the materials discussed above, the bulk appears to be a true insulator with an unusual low-temperature saturation. Because the bulk is an insulator, is it possible to determine
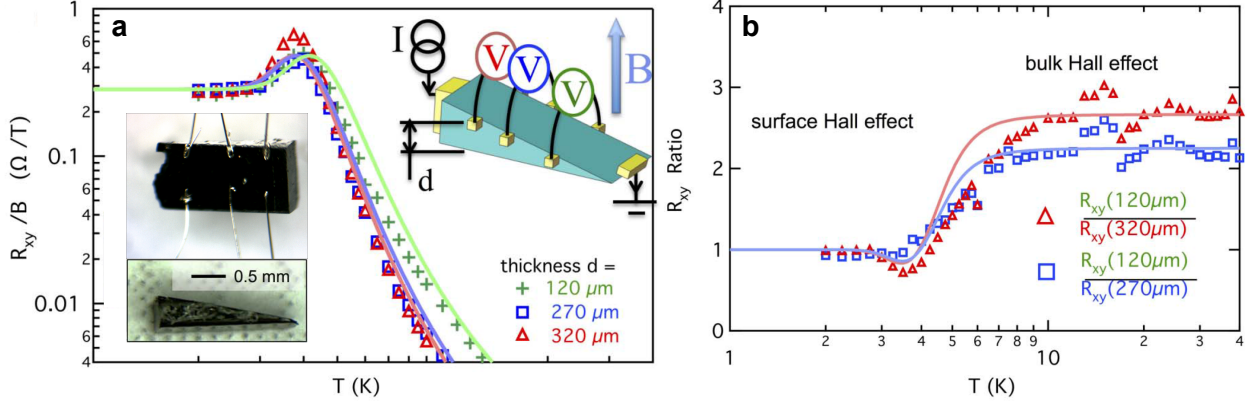
Figure 4.1: (a) Hall resistivity versus temperature for three different thicknesses along a single SmB$_6$ wedge-shaped crystal. The inset shows a top- and side-view picture of the sample. (b) The ratio of the Hall resistances versus temperature. At higher temperatures, the bulk conduction dominates, so the ratio is proportional to the thickness. At lower temperatures, the surface conduction dominates, so the ratio reduces to unity. The solid lines are fits to a simplified two-channel conduction model described in the text.

whether the residual conductivity has a surface origin using transport measurements.

Hall measurements were performed on wedge-shaped SmB$_6$ crystals. A picture of one of the samples measured is shown in the bottom left insets of figure 4.1(a). The bottom photograph is a side-view of the sample showing the sloped top surface that gives the sample its wedge shape. By attaching pairs of leads along the length of the sample, the Hall voltage can be measured at different sample thicknesses from a single crystal. The top photograph is a picture of the sample after the leads have been attached. Because the leads are not attached to the sides of the sample, to get the true Hall voltage it is necessary to scale the measured Hall voltage by the ratio of the distance between a pair of leads over the width of the sample.

The upper right inset shows a schematic view of the ideal measurement setup. A current is applied from the thick side of the sample to the tip of the wedge. A magnetic field is applied perpendicular to the bottom face of the sample. The voltage ($V_{xy}$) is then measured across successive pairs of leads along the length of the sample. In the sample shown in figure 4.1(a) the three measured thicknesses were 320 $\mu$m, 270 $\mu$m, and 120 $\mu$m. The Hall resistance is given by $R_{xy} = V_{xy}/I$. For a typical material, where the majority of conduction is through

the bulk $R_{xy}/B \propto 1/d$ where $B$ is the applied field and $d$ is the thickness of the sample. If, however, the majority of the conduction is through the surface, then the Hall resistance will be independent of the sample thickness.

For a two channel model where one of the channels is a surface channel and the other is a bulk channel, the Hall resistance can be given by:[63]

$$R_{xy}/B = \frac{R_S\rho_B^2 + R_B\rho_S^2 d + R_S R_B (R_S d + R_B)B^2}{(\rho_S d + \rho_B)^2 + (R_S d + R_B)^2 B^2} \tag{4.1}$$

$R_S$ is the Hall coefficient for the surface, $\rho_s$ is the surface resistivity, $R_B$ is the Hall coefficient for the bulk, and $\rho_B$ is the resistivity of the bulk. In the above equation, $R_S$ and $\rho_S$ no longer have thickness dependence, so they were each multiplied by d. For small fields, the terms proportional to $B^2$ can be ignored, leaving:

$$R_{xy}/B = \frac{R_S\rho_B^2 + R_B(\rho_S)^2 d}{(\rho_S d + \rho_B)^2} \tag{4.2}$$

If the bulk dominates conduction ($\rho_S >> \rho_B$) this reduces to $R_{xy}/B = R_B/d$ showing the correct $1/d$ dependence. On the other hand, if the surface dominates conduction, then it reduces to $R_{xy}/B = R_S$, which has no thickness dependence. Using low field data (B < 1 T), $R_{xy}/B$ for the different thickness was measured and plotted in figure 4.1(a). At high temperatures, the measured Hall resistivity differs between the three different thicknesses, but at the sample is cooled below 4 K, they all converge to the same value of .3 $\Omega$/T. Since more than one conduction channel probably exists on the surface,[64, 65] it is not possible to determine surface carrier density or mobility from this measurement.

Figure 4.1(b) presents the ratio of the Hall resistance between two pairs of thicknesses: $120\mu$m/$320\mu$m (1/2.66) and $120\mu$m/$270\mu$m (2.25). At high temperatures (T > 10 K) the inverse ratio of the thicknesses is very similar to the ratio of the Hall resistances. As the temperature is lowered to below 4 K, the ratios all converge to unity. This is clear evidence that the character of the conduction changes from bulk at high temperatures to surface at low temperatures. The solid lines in both plots are calculated by using the equation for low-field Hall resistivity given above. It is assumed that the surface carrier density and resistivity are both constant in temperature. For the bulk, it is assumed that the carrier density decreases (and resistivity increases) exponentially with temperature with an activation energy of 38 K. This fairly simple model qualitatively captures all of the features observed in Hall resistance and ratio plots.

Another way to demonstrate surface conduction is through a "non-local" transport experiment. If the surface of a material is conducting while the bulk is a near-perfect insulator, then there should be non-local voltages due to the transport of current through the surface of sample instead of directly through the bulk. This effect is also observed in $SmB_6$ crystals. The inset of figure 4.2(a) shows a schematic of a thin plate sample that was measured to look for non-local voltages. A photograph of the top surface of the sample can be seen in the inset of panel (b). In this measurement, current is applied between contacts 1 and 6, which are ideally located in the center of the sample. Voltage is then measured across the pair of contacts 2 and 3 ($V_{23}$) and the pair of contacts 4 and 5 ($V_{45}$).

If bulk conduction is dominating, then nearly all of the current density will be concentrated at the center of the sample between pins 1 and 6 (see the inset of figure 4.2(b)). Some current density will pass near pins 2 and 3, whereas only a very small amount will be found near pins 4 and 5. Thus, it is expected that $V_{23}$ should be much larger than $V_{45}$ under any conditions where the bulk conduction is dominating. On the other hand, if surface conduction is dominating, then the majority of the current will be concentrated on the
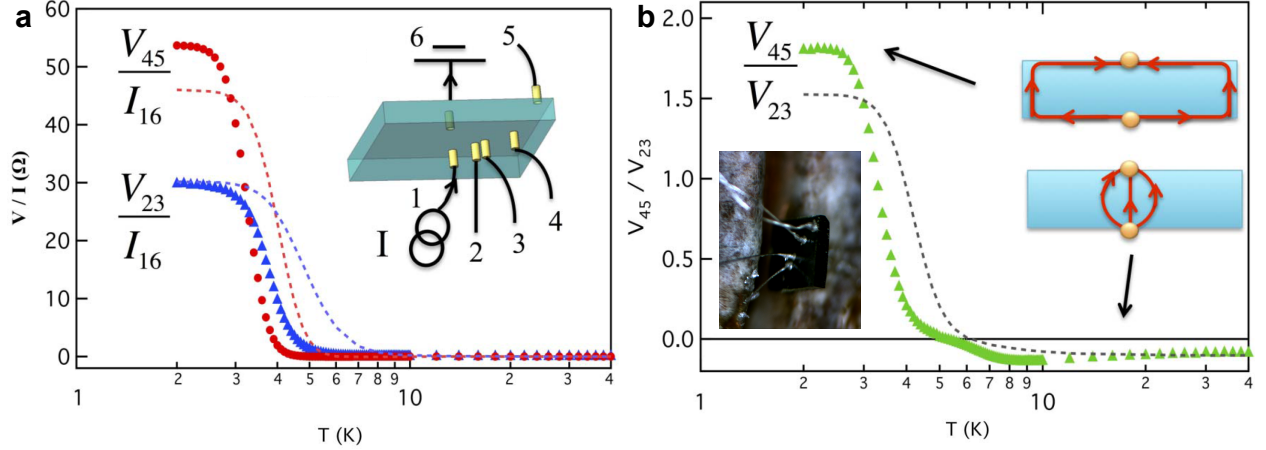
Figure 4.2: (a) Voltage divided by applied current for measurement setup depicted in inset. (b) The voltage between pins 4 and 5 divided by the voltage between pins 2 and 3. Inset in bottom-left shows a photograph of the front side of the sample. Insets in upper-right show a cartoon depiction of current flowing through the bulk compared to flowing across the surface. The dashed lines are calculated from finite element method simulation, the details of which are described later.

surface of the sample. It is expected that both $V_{23}$ and $V_{45}$ should greatly increase as the conduction channel changes from bulk to surface. Experiments confirmed that this is the case. Figure 4.2 shows that as the temperature is lowered both $V_{23}$ and $V_{45}$ show a very large increase. Additionally, the ratio $V_{45}/V_{23}$ is very small (although negative) at high temperatures and actually exceeds unity as the temperature is lowered.

To be certain that the above result agrees with a crossover from bulk to surface conduction, finite method simulation was performed using a commercial finite element analysis software tool. As mentioned before, the change in bulk resistivity is modeled as arising a thermally activated gap: $\rho_B = \rho_B^0 e^{\Delta/k_B T}$. The resistivity of the surface is assumed to be a constant with temperature. The sample is modeled as a rectangular cuboid of dimensions similar to the actual sample with resistivity determined by the above equation for bulk resistance. Surrounding the bulk volume, a very thin (200 nm) layer was added with constant resistivity to represent the surface state. Two very low resistance wires were extruded from the sample to represent the current leads. During simulation, a voltage difference of 1 V was applied across the current leads. For simulation purposes, it was not necessary to extrude voltage
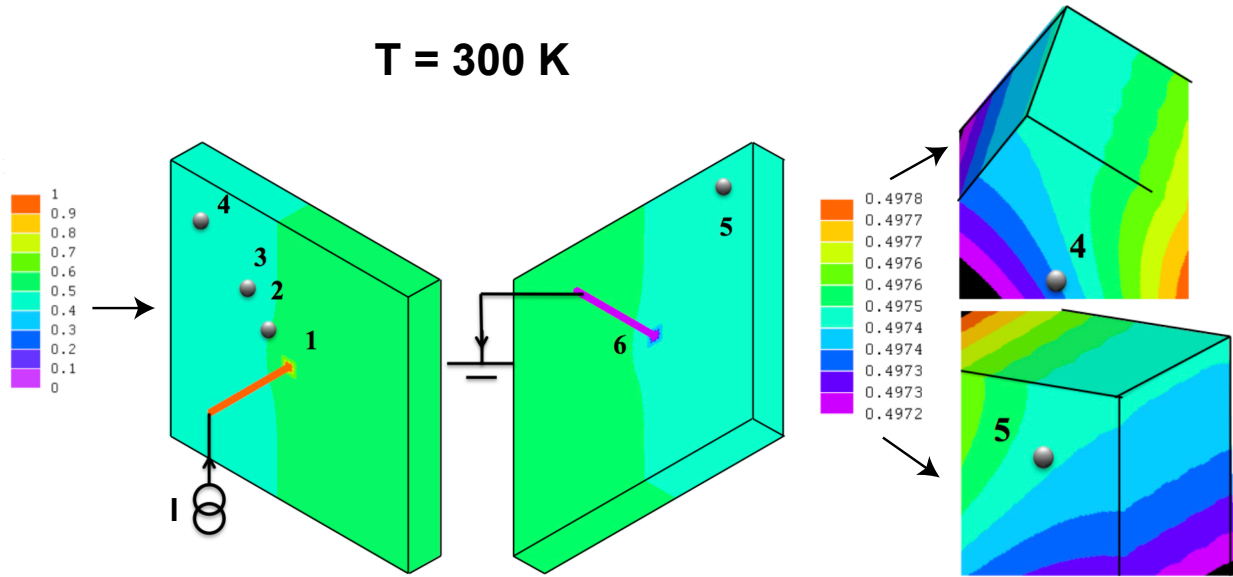
Figure 4.3: Simulation of voltage on plate-shaped sample at 300 K. Zoomed in view of corner is shown on the right side of the panel. The color scale represents voltage. A slight mismatch in the positioning of pins 1 and 6 leads to a negative voltage difference between pins 4 and 5.

leads from the sample. The voltage value is calculated at every point of the model.

Figure 4.3 shows the results of the simulation at 300 K. The entire sample is at nearly the same potential of .5 V. Near the points where the voltage leads make contact with the sample, it is possible to see a small region where the voltage is not .5 V. This region does not extend very far away from the current leads in the high temperature regime. One puzzle when analyzing the experimental data was the negative voltage for $V_{45}$ observed at high temperatures. Because in the actual sample the current leads were not directly across from each other, the relative position of the current leads (1 and 6) was varied. The simulation revealed that a slight misalignment of the current leads results in non-symmetric voltages across the diagonal of the sample face. The right side of figure 4.3 shows a zoomed in view of front and back corner of the simulated sample. It is easily seen that voltage pins 4 and 5 can be arranged in such a way that pin 4 is at a slightly lower voltage than pin 5.

Figure 4.4 shows the results of the simulation at 0 K, when the bulk is a perfect insulator.
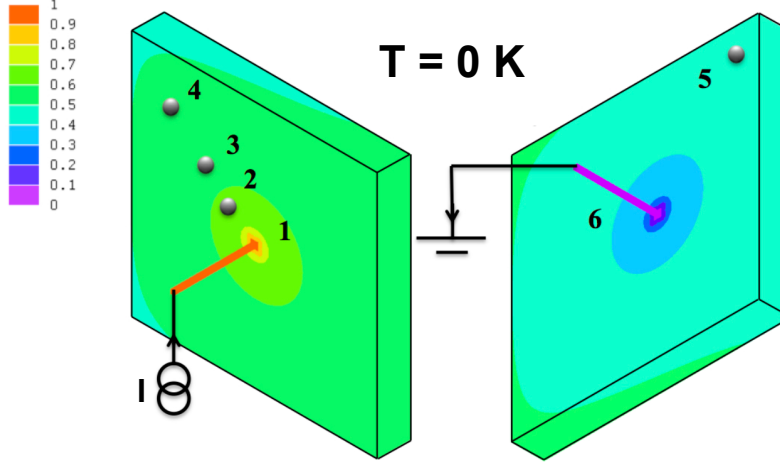
Figure 4.4: Simulation of voltage on plate-shaped sample at 0 K. Since the current now flows along the surface, the voltage decreases radially outward from each current lead. The color scale represents voltage.

Under these conditions, there is a clear radial pattern of voltage potentials extending outward from each of the current leads. The potential of any given point on the surface is proportional to its distance (along a path on the surface) away from the current lead. This leads to $V_2 > V_3 > V_4 > V_5$. The change in sign of $V_{45}$ is clear indication of the crossover from bulk- to surface-dominated conduction.

After fixing the geometry, the simulation was performed at many different temperatures between 0 K and 300 K. At each temperature, the only value that changes is the resistivity of the bulk. After performing the simulation at all temperatures, a curve can be generated for $V_{23}$ and $V_{45}$ as a function of temperature. The result is presented as the dashed lines in figure 4.2. The simulated behavior qualitatively matches the experimental data, correctly capturing the crossover from negative to positive voltage in $V_{45}$. At temperatures greater than 40 K, experimental data for $SmB_6$ does not follow the activated behavior very closely, sometimes even behaving like a metal (increasing resistance with temperature) down to about 100 K. Thus, it is not surprising that the simple two channel model (constant surface, activated bulk) is unable to quantitatively match the experimental data.

The experiments presented above provide strong evidence that $SmB_6$ has a conducting sur-

face state that dominated transport at low temperatures. After abrading the surface of the wedge-shaped sample, the thickness-independence of the Hall data was repeatable, demonstrating that the surface state is quite robust to non-magnetic perturbation. Near the same time that this study was performed, an independent group also confirmed surface conduction in $SmB_6$.[66] A later experiment showed that is the surface is completely destroyed by non-magnetic ion bombardment surface conduction is reestablished in the undamaged material underneath.[67] Combined, these experiments definitively show that $SmB_6$ possesses a very robust conducting surface state.

## 4.2.2   Transport at Millikelvin Temperatures

To further characterize the surface state of $SmB_6$ transport measurements were performed on many single-crystal samples at temperatures as low as 20 mK and fields up to 12 T. Low temperature magnetoresistance can provide information about the nature of the surface states. For example, magnetoresistance data in high fields could potentially reveal Shubnikov de-Haas (SdH) oscillations from the surface state, which might provide evidence of the effective mass of the surface electrons and also confirm the 2D shape of the conducting surface. Unfortunately, SdH oscillations were never observed. All samples measured revealed negative magnetoresistance at the highest fields measured. However, some samples showed a region of positive magnetoresistance centered at 0 T. Further, low temperature resistance versus temperature data revealed that the surface state of $SmB_6$ does not behave as a simple metal as the temperature is decreased, but instead shows a slight increase in resistance as the temperature is lowered. This temperature dependent behavior is likely due to Kondo scattering in the surface state.

Magnetoresistance measurements of three different $SmB_6$ crystals are presented in figure 4.5 at temperatures $\leq$ 170 mK. Typical behavior of the measured $SmB_6$ samples is negative
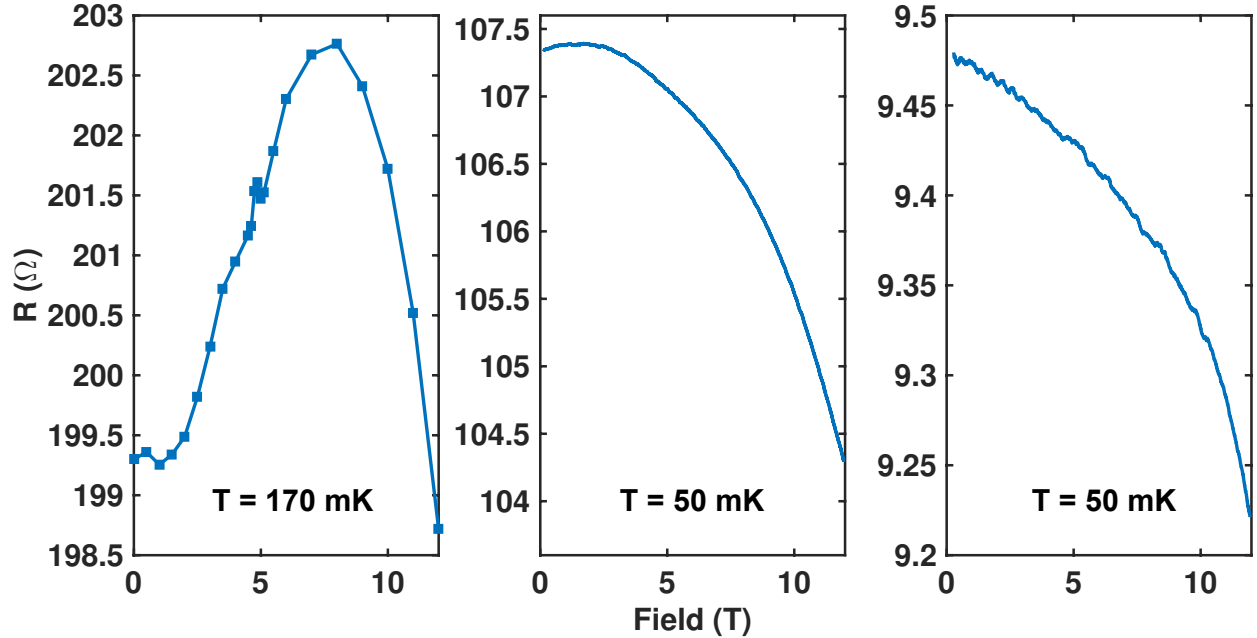
Figure 4.5: Comparison of magnetoresistance of $SmB_6$ at milli-Kelvin temperatures. All samples show negative magnetoresistance a high fields. At low fields, the samples have very different amounts of positive magnetoresistance.

magnetoresistance at high fields. This behavior had historically been attributed to field dependent closure of the hybridization gap, reflecting a slight increase in the conductivity of the bulk.[68] However, it has recently been argued that the field needed to suppress the gap to a level detectable in transport at such low temperatures is much higher than the 12 T maximum field measured here.[69] As shown later, the resistance versus temperature curves do show evidence of Kondo scattering. If the resistance increase is due to Kondo scattering (regardless of where the magnetic impurities come from that cause the scattering) it is expected that a increase in the applied field would serve to reduce the amount of scattering. However, negative magnetoresistance is also observed at higher temperatures when the bulk dominates transport.

The origin of the positive magnetoresistance in certain samples is less clear, especially considering the high variance in the amount or even existence of a positive magnetoresistance region between samples. The magnetoresistance also depends on the angle between the current and the applied field. As shown in figure 4.6, when the field is applied parallel to
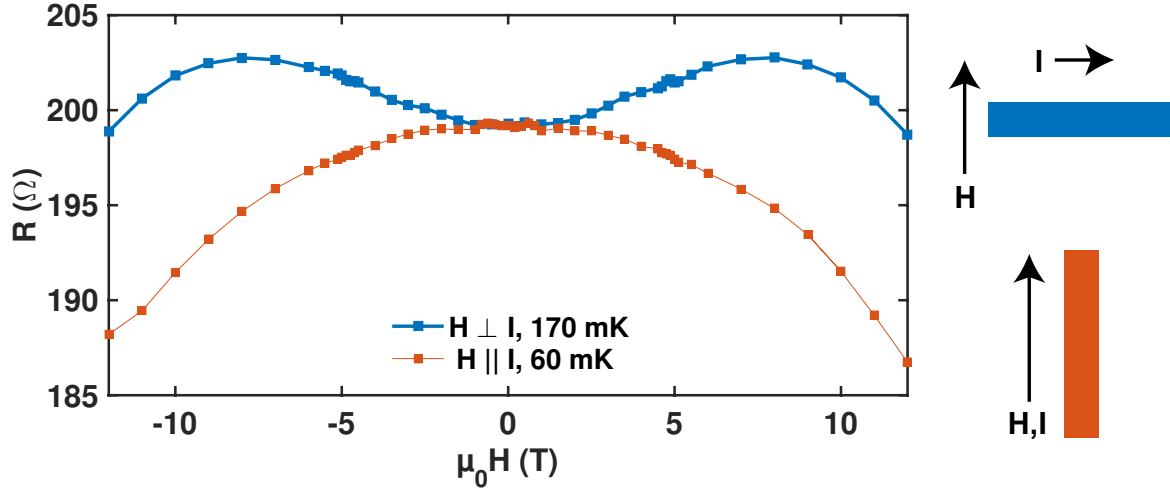
Figure 4.6: Comparison of magnetoresistance of $SmB_6$ at milli-Kelvin temperatures. In one configuration, the field is applied perpendicular to the current (blue curve). In the other, the field is applied parallel to the current (red curve).

the current, the region of positive magnetoresistance disappears. Due to the highly sample dependent nature of this effect, it is not possible to draw any strong conclusions about its origin.

Even in the saturation regime, where the metallic surface state is dominating conduction, the resistance of $SmB_6$ continues to increase. As shown in figure 4.7, this resistance rise is fairly linear in $\ln(T)$ for temperatures higher than .3 K, suggesting it is due to Kondo impurity scattering. Initially, it was proposed that the impurities are due to "Kondo holes" that arise when non-magnetic impurities substitute Sm on the surface.[70] The resulting Sm hole can then act as a magnetic impurity due to its absence. More recently, it was also suggested that the origin of the magnetic impurities may be a Samarium oxide layer on the surface.[69] The Kondo impurity behavior is also expected to be suppressed as a function of applied field, and may explain the origin of some of the negative magnetoresistance observed in $SmB_6$.
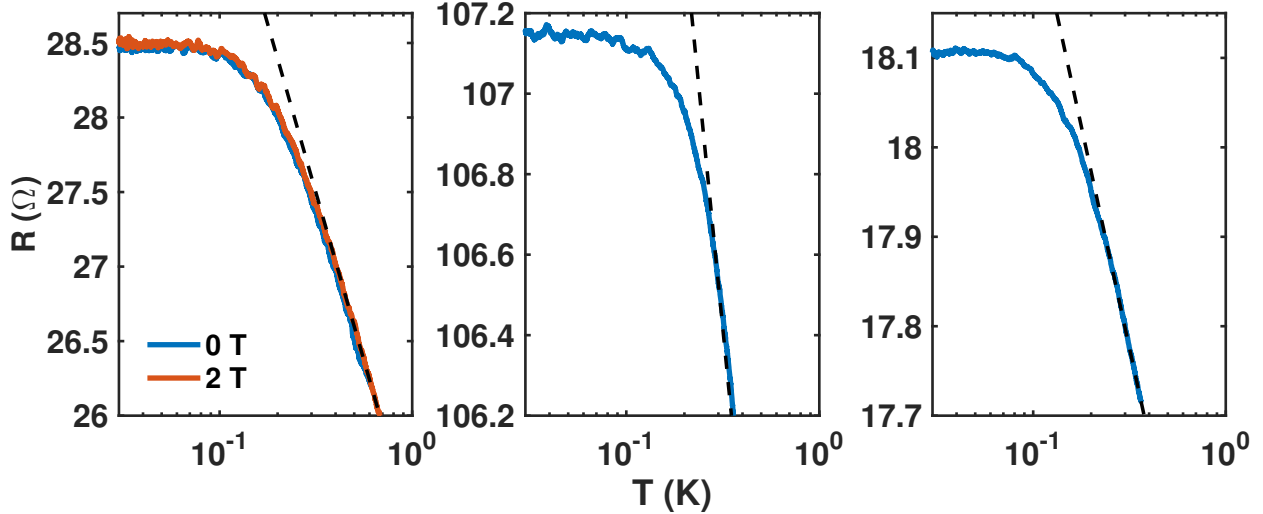
Figure 4.7: Resistance versus temperature for $SmB_6$ below 1K. Temperature is plotted on a log scale. The dotted lines are fits to T > .3 K that are linear in ln(T).

### 4.2.3 Quantum Oscillations

Further information about the shape of the Fermi surface can be obtained through the measurement of the angular dependence of quantum oscillations. To date, no group has reported quantum oscillations in the resistivity of $SmB_6$. However, two independent reports have been made on de Haas-van Alphen oscillations (dHvA, oscillations in the magnetization). In the first report, the dHvA oscillations were attributed to a 2D Fermi surface arising from the metallic surface state.[71] The cyclotron mass of the surface electrons (on the order of .1 $m_e$) was quite surprising considering that the origin of the surface state was thought to be the hybridization between the conduction band and the relatively heavy Sm $f$-electrons. Considering the high mobility and light mass observed by Li et al.,[71] it is unexpected that experimental evidence of oscillations has not be found in transport measurements. Further, combined thermopower and transport measurements suggest a heavy effective mass on the order of 10 to 100 $m_e$ for the surface states of $SmB_6$.[72] In the second report of quantum oscillations, the measured Fermi surface had a 3D shape and was claimed to arise from the insulating bulk states.[73] The is also surprising considering that quantum oscillations are traditionally observed in clean, metallic systems. Nonetheless, theoretical explanations have

been made for both the light electrons observed in the 2D Fermi surface,[74] and for the unexpected presence of oscillations arising from an insulating state.[75]

Quantum oscillations arise in many physical properties of metallic materials under the condition that $\omega_c \tau > 1$. Onsager showed that the oscillation period in inverse field is proportional to the cross sectional area of the Fermi surface:[27]

$$\Delta(\frac{1}{B}) = \frac{2\pi e}{\hbar} \frac{1}{A_e}$$

(4.3)

For a 2D material, the Fermi surface is expected to have cylindrical features, so that as the surface is rotated in real-space the oscillation frequency diverges proportional to $1/\cos(\theta+\phi)$. In a 3D material, the frequency will also diverge along any open orbits in the Fermi surface.

When searching for dHvA oscillation in $SmB_6$ it was found that flux-grown crystals only exhibit dHvA oscillations from embedded aluminum impurities, in contrast to the previously reported result. The angular dependence of the oscillation frequencies suggests that the impurities grow coaxially with the $SmB_6$ host crystal, with the [100] aluminum axis along the [100] $SmB_6$ axis. The aluminum impurities are often wholly embedded within the bulk, meaning that no feature appears near the aluminum superconducting transition in transport measurements.

The single crystals of $SmB_6$ measured were grown using the aluminum flux method, which turns out to be very important. Magnetization was measured down to 2 K in the PPMS, or down to 30 mK in the dilution refrigerator using the cantilever-based torque magnetometry described in section 2.2.4. Figure 4.8 shows a survey of four different $SmB_6$ crystals that were measured in the PPMS. Only two of the four show evidence of dHvA oscillations. Although both samples S2 and S4 have similar surface area and were mounted at nearly the same angle, the oscillation amplitude appears to be stronger in S4. The lack of any dHvA oscillations in two of the samples measured, and the differing amount of oscillations in two seemingly
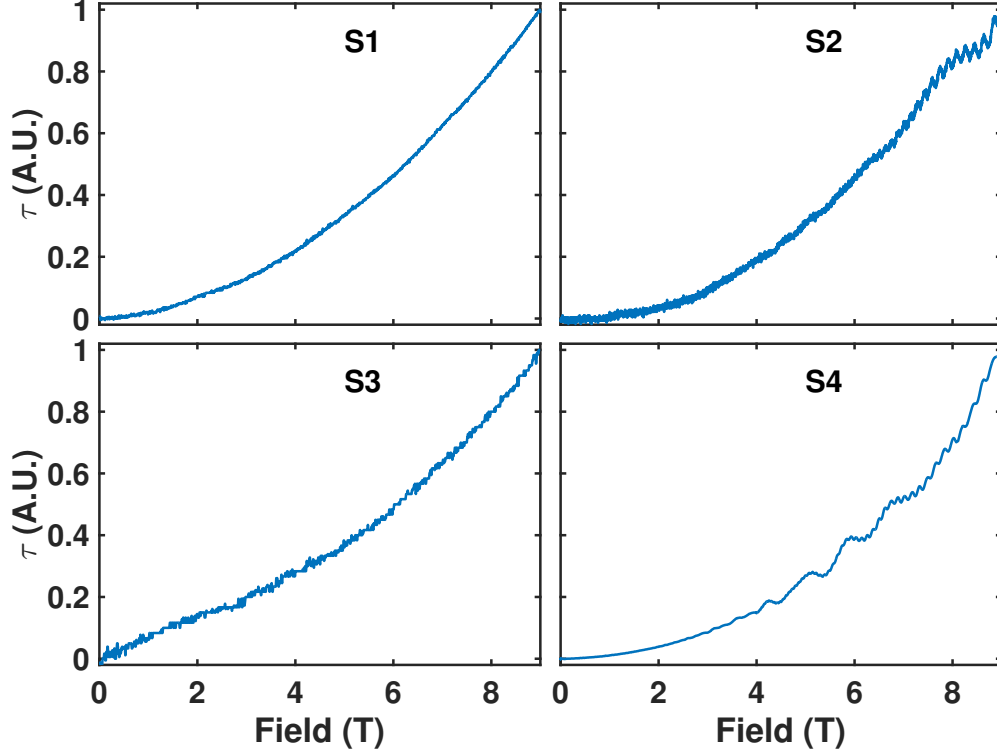
Figure 4.8: Survey of torque magnetometry results at 2 K in 4 different $SmB_6$ crystals. Only two of the crystals measured showed any evidence of quantum oscillations (S2, S4).

similar samples, suggests that the origin of the oscillations may not be an intrinsic property of the 2D surface states.

Further concerns arise when considering the thermal damping of the oscillation amplitude. The magnitude of the dHvA oscillations has temperature dependence given by the Lifshitz-Kosevich formula:[13]

$$R_T = \alpha T m^* / B \sinh\left(\alpha T m^* / B\right) \tag{4.4}$$

Figure 4.9 shows a fit of the low-frequency oscillation amplitude to the thermal damping equation. Using this fit, an effective mass of .101 $m_e$ was obtained, which is consistent with both the previous value obtained for the low-frequency (large area) orbit of aluminum and $\alpha$-orbit observed by Li et al. when measured near the [100] axis.[71, 76]
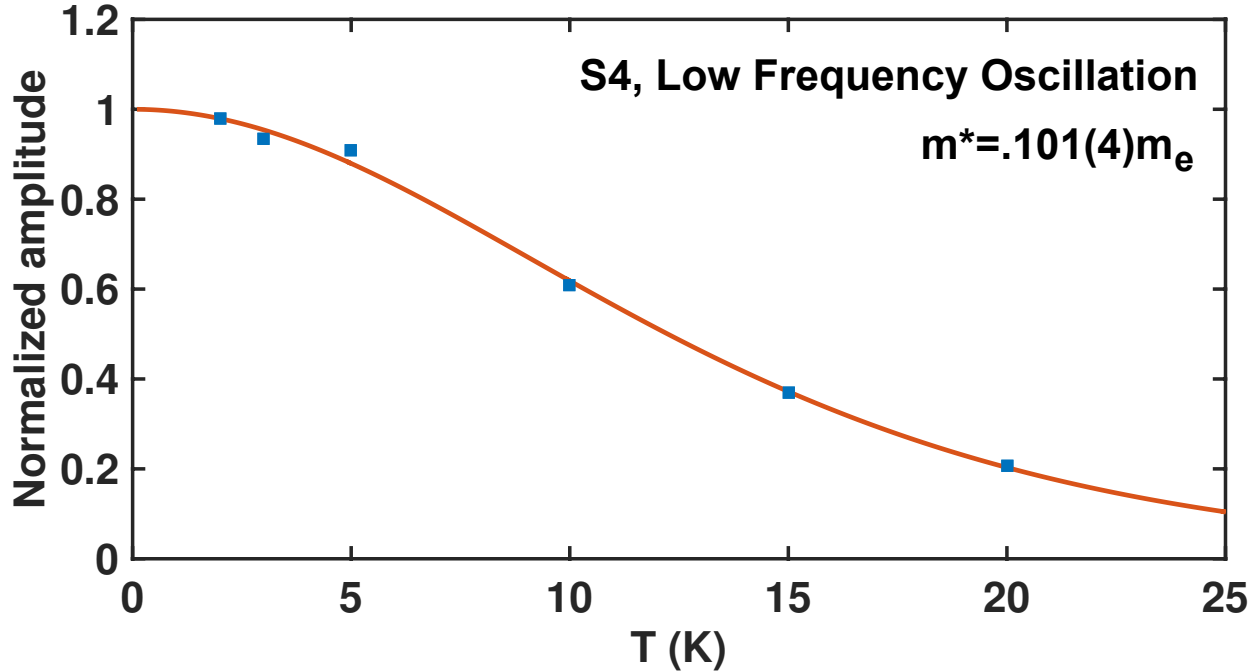
Figure 4.9: Thermal damping of lowest frequency oscillation with field along [100]. The oscillation had a frequency of 50 T.

The close agreement between the $SmB_6$ oscillation and aluminum is somewhat concerning on its own, but the light electron mass reveals another problem. Much effort has been spent searching for evidence of Shubnikov-de Haas oscillation (SdH) in resistivity, but so far none have been reported. Figure 4.10 shows a magnetoresistance measurement at 50 mK of an $SmB_6$ crystal. Fourier analysis of the results reveals no dominant frequency peaks, and especially none that agree with the frequency of dHvA oscillations. Many other samples were measured, on both (100) and (110) surfaces which are claimed to be the origin for the 2D dHvA oscillations. All magnetoresistance measurements lacked evidence of SdH oscillations. Wolgast et al. measured at fields as high as 45 T on both (100) and (110) surfaces and has also failed to observe SdH oscillations.[69] Originally it was argued that the lack of observation of SdH oscillations may be due to the fact that most of the magnetoresistance measurements had been performed on samples with a much larger amount of (100) surface area compared to (110) surface area and that the electrons from the (110) surface contribute much larger oscillation amplitude. However, in the magnetoresistance measurements of Wolgast et al.,
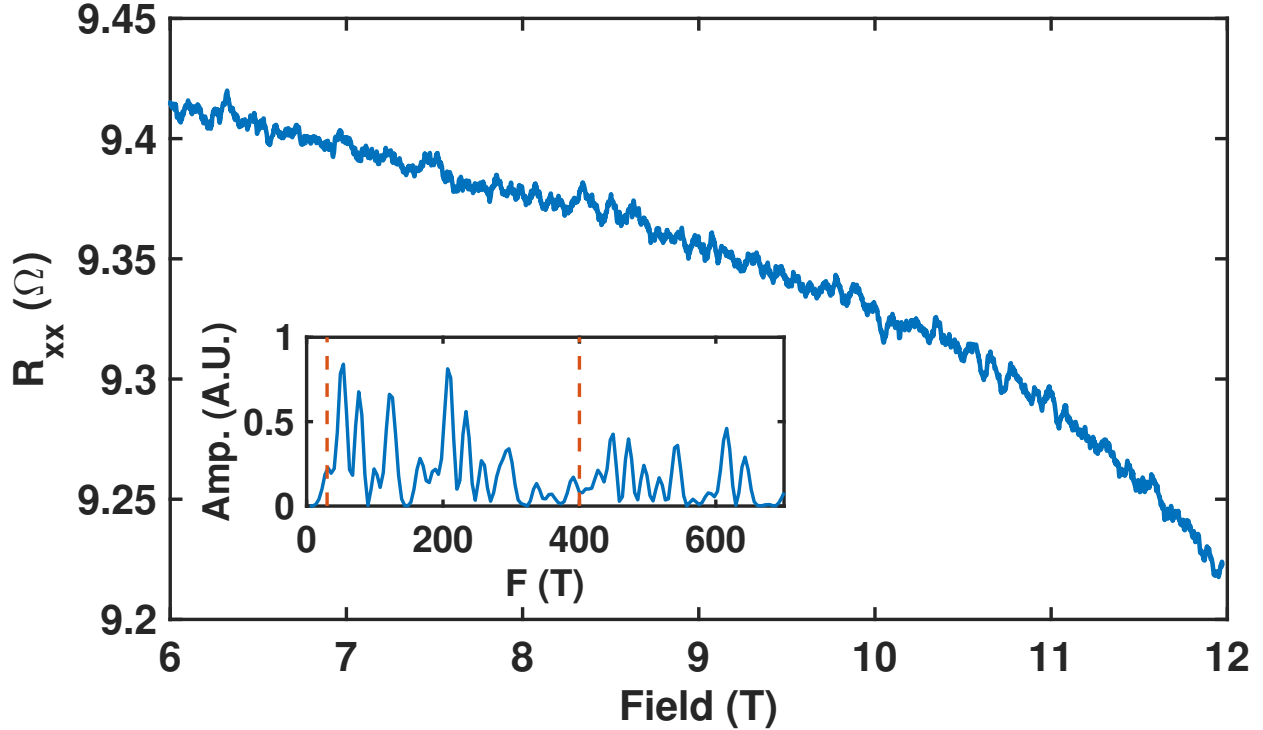
Figure 4.10: Resistance versus field of $SmB_6$ at 50 mK. The inset shows an FFT of the data (resistance versus inverse field) after a polynomial background has been subtracted. The dashed lines indicated where peaks would be expected based on the data of Li et al.[71]

special structures were used that can isolate the contribution to transport from each surface, and still no evidence of SdH oscillations was obtained.[69]

Considering the fact that $SmB_6$ is grown with aluminum flux and that aluminum inclusions are very often found in the bulk of the sample when polishing, the most likely scenario is that the dHvA oscillation signal in flux-grown $SmB_6$ is due to subsurface aluminum inclusions. To confirm this possibility, S2 was polished to check for the possibility of any subsurface aluminum. The inset of the left panel in figure 4.11 shows the sample after polishing away about 1/3 of the thickness. The polished surface is a (100) surface. Three unconnected aluminum inclusions were discovered.

Even though three unconnected aluminum inclusions were found, the FFT spectrum (left panel of figure 4.11) only shows one dominant frequency in the 300 to 400 T range. The
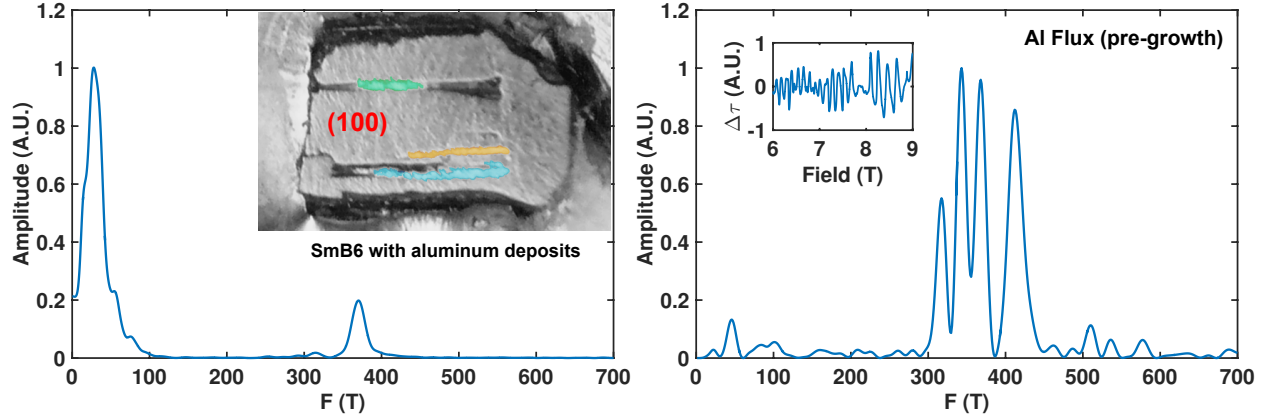
Figure 4.11: Frequency comparison between embedded aluminum and pre-melt aluminum flux. Panel on the left shows frequency spectrum of $SmB_6$ with embedded aluminum. The highlighted section in the photo show three, unconnected aluminum deposits. Panel on the right shows frequency spectrum for pre-melt aluminum flux. The inset shows the torque signal on the flux. The embedded aluminum has only a single dominant frequency, whereas the flux has many frequencies in the 300 to 400 T range.

sample was mounted so that the [100] direction of the $SmB_6$ crystal was rotated 5 degrees away from the direction of the applied field. The peak near 370 T is the expected value for single-crystal aluminum if the crystalline [100] axes of all three independent deposits are aligned with the [100] $SmB_6$ axis. As a comparison, torque magnetometry was also performed on a piece of pre-melt aluminum flux (right panel of figure 4.11). The pre-melt flux is an amorphous piece of aluminum composed of many microcrystals. Thus, it is expected to have many randomly oriented domains with respect to the applied field. This explains why there are many peaks in the 300 to 400 T range. The contrast of the FFT spectrum between the aluminum embedded in $SmB_6$ and a piece of amorphous aluminum suggests that any aluminum embedded in $SmB_6$ are aligned coincident with the axes of $SmB_6$.

To determine whether the aluminum inclusions are truly coincident with the $SmB_6$ crystal axes, angular dependent dHvA measurements were performed on S4. In the Li et al. paper, which claimed that the observed dHvA oscillations were from the 2D surface states of $SmB_6$, angular dependent measurements were provided for three different electron pockets: $\alpha$, $\beta$, and $\gamma$.[71] Their measurement of the angular dependence of the $\alpha$ pocket has a very high
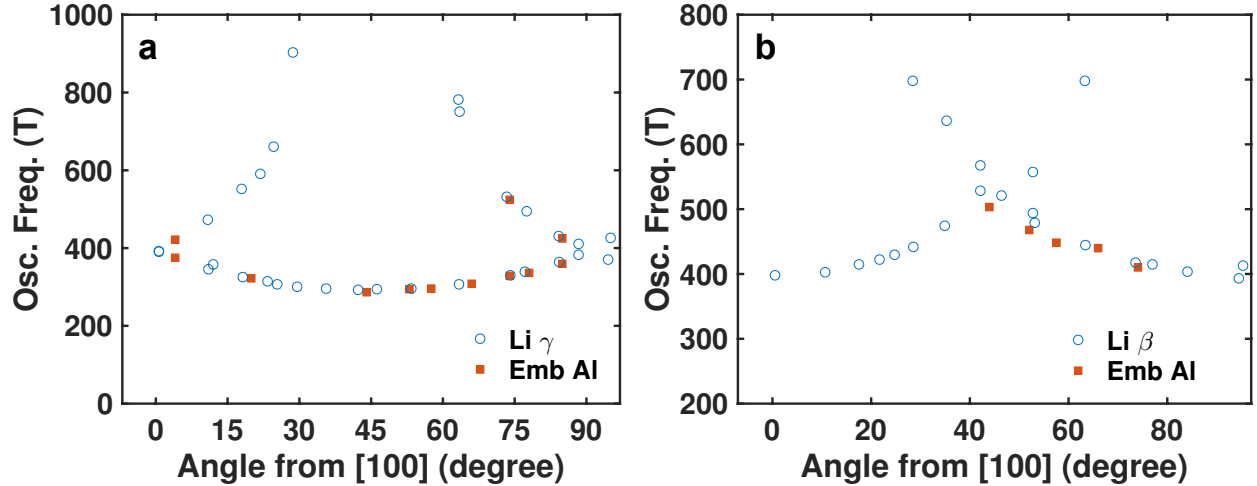
Figure 4.12: Angular dependence of observed oscillations in $SmB_6$ S4. The angles were measure from the [100] axis of $SmB_6$, and the crystal was rotated in a (100) plane. At 0 and 90 degrees, the applied field is along a <100> direction. At 45 degrees, the applied field is along a <110> direction. (a) shows the frequency dependence of the electron pocket that was called the $\gamma$ pocket by Li et al. (b) shows the frequency dependence of the electron pocket that was called the $\beta$ pocket by Li et al.[71]

level of noise (the origin of which will be speculated upon later), so it will be excluded from comparison. Figure 4.12 shows the angular dependence of the so-called $\gamma$ (left panel) and $\beta$ (right panel) pockets, compared with data obtained in my own angular dependent measurements. The data for the $\gamma$ pocket is a very good match, except for the lack of the higher frequency points from Li at al.[71] The data for the $\beta$ pocket is also a fairly good match for the lower frequency points. In general, the lowest frequency $\gamma$ oscillation has the strongest signal in the dHvA measurement. The oscillation amplitude of the $\beta$ and the higher frequency $\gamma$ pockets tend to be nearly one order of magnitude smaller.

When performing the angular dependence measurement, it was necessary to use the PPMS due to the lack of access of a rotating sample stage. After every measurement, the sample stage was removed from the PPMS and the angle of the sample was manually adjusted. This required many fast sample changes, so it precluded the use of the dilution refrigerator (DR). One limitation of the PPMS is that the maximum magnetic field is only 9 T, compared to 12 T in the DR. As the field is increased, the oscillation amplitude also tends to increase in

a relation given by the dingle damping factor:[71]

$$R_D = e^{-\alpha T_D m^*/B} \tag{4.5}$$

$\alpha$ is a constant equal to 14.69 T/K. With the values reported for m* (.129 $m_e$) and $T_D$ (18.58 K) in Li et al., the amplitude of oscillation is expected to more than double between 9 T and 12 T. Also, with a torque magnetometry measurement, the signal is proportional to dM/dH times H. There is an additional factor linear in H that increases the amplitude of the measured oscillations. The measurements in Li et al. were made at a fields up to 45 T, which explains why they were able to obtain more complete angular dependence data.[71] The measurement near 74° was made in the DR. That is why it was possible to measure both the high frequency $\gamma$ oscillation and the $\beta$ oscillation at that particular angle.

The quantum oscillations reported by Li et al. were fit to a $1/\cos(\theta)$ dependence, which was the basis for their claim that they came from a 2D Fermi surface.[71] The lower frequency oscillations are matched nearly perfectly by the values of the oscillations for aluminum in previous reports on aluminum.[77, 78] There is a slight difference in the higher frequency data. This could arrive from several factors, but the main source of the discrepancy is probably misidentification of the peaks. When dHvA is measured in higher fields, one must be especially careful to correctly identify all the peaks that are shown in the frequency spectrum. There are two effects that can cause multiples of a single frequency to arise, or even sums or differences of the frequencies from two separate orbits. The first of these is magnetic breakdown. Magnetic breakdown occurs when electrons tunnel between orbits on different parts of the Fermi surface that are only separated by a small gap.[13] The

requirement for this to occur is:[79]

$$\hbar\omega_c \gtrsim \epsilon_g^2/\zeta \qquad (4.6)$$

Where $\hbar\omega_c$ is the separation between energy levels, $\epsilon_g$ is the energy gap and $\zeta$ is the Fermi energy. The second possibility is magnetic interaction. This occurs when:[13]

$$4\pi\tilde{M} \sim H^2/F \qquad (4.7)$$

Where $\tilde{M}$ is the amplitude of the oscillation, H is the field, and F is the frequency of the oscillations. In fact, magnetic interaction has already be noted as occurring in pure aluminum and has limited the accuracy of previous studies in measuring the Fermi surface using quantum oscillation techniques.[80] Finally, some of the higher frequency oscillations often have lower amplitude that is not much higher than the noise level. It is possible that a claimed peak in the frequency spectrum might actually lack any significance.

The $\alpha$ oscillations reported by Li et al. were also fit to $1/\cos(\theta)$ dependence.[71] However, the oscillation data was subject to a large percent uncertainty in identification of the frequency. This is due to several reasons. First, the small size of the aluminum inclusions precludes measuring the oscillations at very low fields. Since the oscillations are periodic in 1/B, measuring to lower fields would allow for significantly more periods of the low frequency oscillations. Because the number of periods is limited, the frequency peak is likely to be broad, preventing accurate identification of the frequency. Also, in pure aluminum there are many different orbits with frequencies in the range of 25 to 100 T.[77] As only a

single frequency was reported by Li et al. in this range, it is likely that the peaks were all merged into a single broad peak.[71] Fitting such uncertain data to a $1/\cos(\theta)$ curve is optimistic at best. Independently, it does not provide very compelling evidence for the observed oscillations coming from orbits on a 2D surface.

Having established similarity in the angular dependence of the dHvA oscillations, the next step is to confirm the source of the oscillations. Instead of polishing away the sample to determine whether there is are any aluminum deposits, it would be helpful if there was a non-destructive way to help screen samples for any embedded aluminum deposits. Perhaps fortuitously, aluminum has a superconducting transition near 1.2 K, with a critical field of 105 Oe at zero temperature.[81] Thus, it should be possible to search for the presence of aluminum by searching for signatures of the superconducting transition.

Li et al. made the argument that the lack of any feature in the resistance versus temperature curves of their samples at 1.2 K is evidence that the samples measured lack any aluminum in the interior of the sample.[71] Figure 4.13 shows both resistance versus temperature and resistance versus field curves for S4. There is clearly no feature in the resistance versus temperature curve at 1.2 K. Further, no transition is evident in either of the resistance versus field curves out to 2500 Oe.

Either transport measurements are not useful for probing whether there is subsurface aluminum, or sample S4 does not contain any aluminum deposits. The first scenario is actually quite likely. The reason for the interest in the study of $SmB_6$ is that it is expected to have a metallic surface state and an insulating bulk. An Arrhenius fit to the thermally activated behavior of the bulk shows that at temperatures near 1 K, the bulk resistance is expected to be many orders of magnitude larger than the surface. Thus, there is no parallel conduction channel between the outer surface of an $SmB_6$ crystal and an interior surface that is in contact with an aluminum inclusion. Even though the interior surface's resistance may be shorted out by aluminum at the superconducting transition, the bulk completely insulates
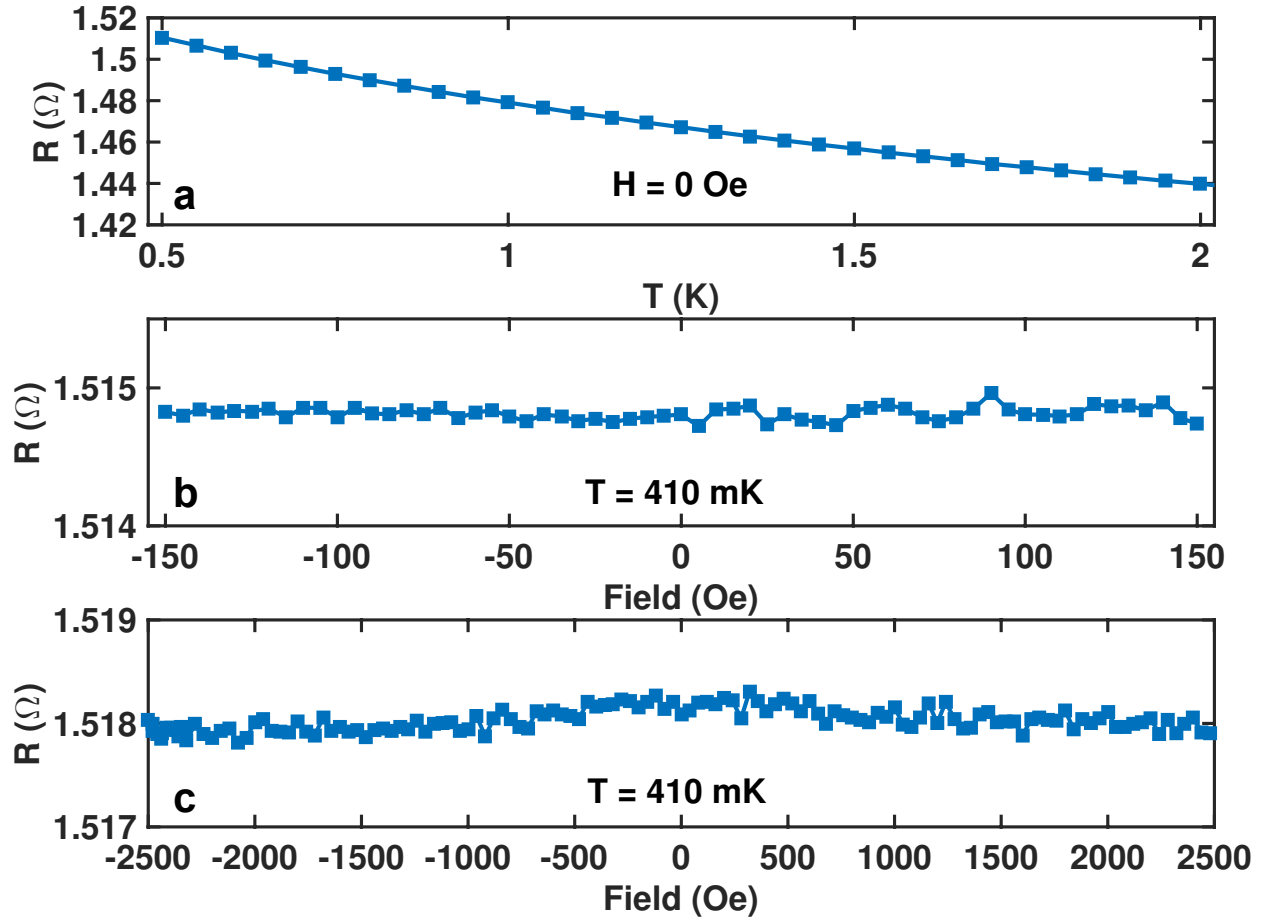
Figure 4.13: Low temperature transport of $SmB_6$ S4. (a) Resistance versus temperature at zero magnetic field. Note the lack of any feature at or near 1.2 K. (b) Resistance versus field at 410 mK in a very narrow field range of $\pm150$ Oe. At 410 mK, the critical field should be about 92 Oe. (c) Resistance versus field at 410 mK in a wider field range. If the aluminum inclusions were filamentary, it is possible that the critical field could be higher. No transition is observed even to $\pm2500$ Oe. The apparent feature is due to a slight instability in the temperature.

the exterior surface from this change.

To conclusively determine whether there is any subsurface aluminum inclusion, it is necessary to use other probes. There are several other methods that still might be used: heat capacity, torque magnetometry, and AC susceptibility. Of the three, heat capacity might be the most useful. If a jump in heat capacity can be observed at the superconducting transition, it can be used to determine the total amount of aluminum contamination in the sample. However, if the total amount of aluminum is too small, then there is a chance that no feature will be observed in heat capacity. On the other hand, if torque magnetometry can determine whether there is a superconducting transition from aluminum, it would be the most convenient probe as long as the cryostat that is being used for the torque magnetometry experiment is capable of reaching temperatures below 1.2 K. In this case, before ramping to high fields to perform a dHvA measurement, the sample could first be measured at very low fields to check whether there is a signature from an aluminum inclusion. This approach can suffer from the drawback that the torque magnetometry signal scales with the applied field. At very low fields, there might not be enough resolution to measure a superconducting transition if the inclusion is too small. AC susceptibility provides the most sensitive probe for the existence of an aluminum inclusion, but unlike heat capacity it cannot be reliably used to determine the total volume of the inclusion (it can only determine whether there is screening of magnetic field by the surface of the inclusion, not the bulk Meissner effect).

Evidence of an aluminum inclusion is visible in both AC susceptibility and a low-field torque magnetometry measurement of S4. However, the background signal from $SmB_6$ was too large to tell if there was a jump in specific heat near the superconducting transition of aluminum. Figure 4.14 shows low field measurements of both susceptibility and torque at temperatures near or below the superconducting transition of aluminum. While the torque measurement does have a signal that seems to coincide with the critical field temperature dependence of aluminum, its behavior is quite strange. The signal is not symmetric around
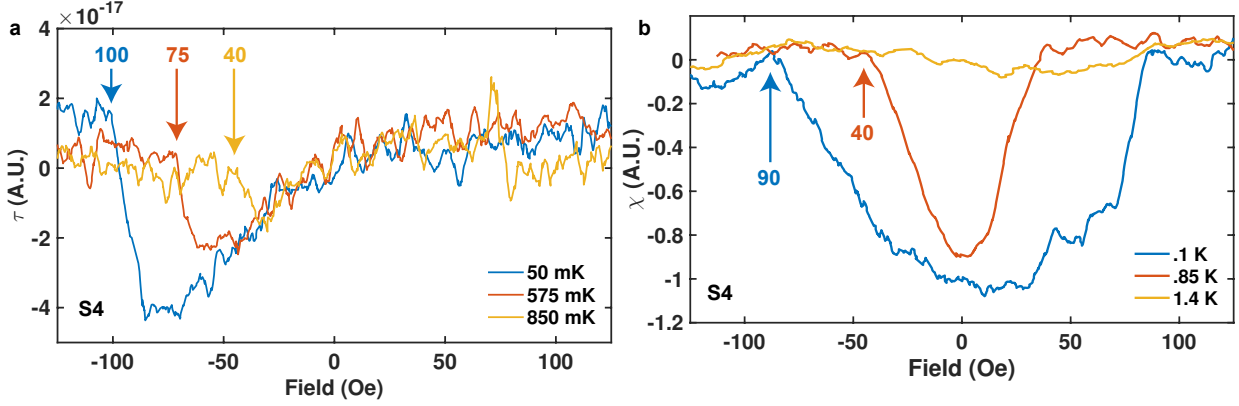
Figure 4.14: Low-field torque and AC susceptibility of $SmB_6$ S4. Both measurements are in arbitrary units (uncalibrated). (a) Measurement of torque versus field in S4. The magnetic field was swept from positive to negative field during measurement. (b) The real part of AC susceptibility versus field.

zero applied field, but instead depends on the direction of the magnetic field sweep. In the data shown, the field was swept from positive to negative field. If the direction of the magnetic sweep is reversed, the data is essentially mirrored over the H = 0 axis. The reason for this dependence on the direction of the magnetic field sweep is not fully understood. Nonetheless, the temperature and field dependence of the transition is a close match to the critical temperature of aluminum. AC susceptibility also shows the expected behavior for an embedded aluminum inclusion.

The strong match between the angular dependence of aluminum and the ubiquitous presence of sub-surface aluminum in larger single-crystal of $SmB_6$ suggests that the 2D quantum oscillation signal identified by Li et al. is actually due to the aluminum inclusions. The dHvA signal only exists in a subset of all $SmB_6$ crystals measured; typically those with a much larger volume. The lack of multiple dominant oscillation frequencies in a crystal with 3 separate aluminum inclusions suggests that there is alignment between the $SmB_6$ and aluminum crystal axes. Finally, the angular dependence of the dHvA oscillations in a sample that is known to include aluminum nearly perfectly matches the data obtained by Li et al.[71] It should not be too surprising that the very light effective mass oscillations are not intrinsic to the surface state of $SmB_6$. The predicted surface state arises from the inversion

of a $4f$ and $5d$ band, and was theoretically predicted to result in heavy quasiparticles.[64, 65] To resolve intrinsic quantum oscillations in $SmB_6$ may require going to much higher fields and even lower temperatures. Even if high enough fields might be reached, at some point the field can become so large that the Kondo insulating behavior is quenched and transport or magnetization measurements may no longer be able to distinguish the surface from the bulk.[68] Finally, the quantum oscillations indicative of a 3D Fermi surface coming from the bulk $SmB_6$ is a separate matter entirely.[73] The crystals used in that study were not grown from aluminum flux, so the arguments presented above are not applicable.

## 4.2.4    Magnetic Dopants

One prediction of a surface state in a topological insulator is that the surface state should be resistant to perturbations that do not break time-reversal symmetry.[55] On the other hand, breaking time-reversal symmetry may cause the destruction of the surface state. It was shown that doping $SmB_6$ with low concentrations of Gd impurities resulted in bulk dominated conduction down to the lowest temperatures measured.[82] This was accomplished using a sample polishing technique. In a bulk material, the resistance is given by $R = \rho l / A$, where A is the width times the thickness. By reducing the thickness by a factor of two, the resistance doubles. If however the conduction is dominated by a surface state, the resistance is independent of sample thickness. By measuring an undoped $SmB_6$ crystal, polishing it (while making sure the original leads stay intact), and measuring it again, it is possible to see the crossover from bulk to surface conduction as the temperature is lowered by plotting the resistance ratio between the two measurements. At high temperatures, the ratio is equivalent to the ratio of the thicknesses, but as the conduction channel changes to the surface, the ratio goes to unity. Kim et al. found that when doping $SmB_6$ with non-magnetic impurities the surface state was preserved (see figure 4.16(c)). However, when doping $SmB_6$ with Gd, the resistance ratio remained constant down to at least 2 K.[82]

In another study, the surface of an $SmB_6$ crystal was bombarded by both magnetic (Iron) and non-magnetic ions.[83] For non-magnetic ions, it was found that although the surface layers of the $SmB_6$ crystal were destroyed by the ion bombardment, the surface state reconstructed under the damaged upper layers. Somewhat surprisingly, this was also found to be the case when $SmB_6$ was bombarded with Iron ions. The proximity of Iron to the undamaged portion of the $SmB_6$ surface did not affect the surface states. There are at least two different explanations for this different behavior to a magnetic perturbation. On one hand, it is already well established that an applied magnetic field does not destroy the surface state in $SmB_6$.[68] Therefore, it is not too surprising that proximity to Iron has no effect. Perhaps then, Gadolinium is a special case. Due to its very large J (7/2) value it may be able to locally perturb the surface state in a way that an applied magnetic field or Iron ions are not. On the other hand, the bombardment with Iron ions does not extend all the way through the bulk of the samples. It may be that the surface state only reforms far away from the magnetic influence of the Iron atoms. Thus, more information is needed to understand the influence of magnetic perturbation on $SmB_6$. Further studies were carried out with Gd-doped $SmB_6$, measuring to lower temperatures and performing a survey on a large number of samples. The effect of Ce-doping is also explored.

Figure 4.15 shows the magnetoresistance (MR) of Ce-doped, Gd-doped and undoped $SmB_6$. A striking difference between Gd and Ce dopants can be found in a comparison of the low-temperature MR (panel (a)). Near zero field, Gd-doped samples exhibit a large peak in MR that is quickly suppressed with applied field. The peak is not affected by the orientation of the sample with respect to an applied magnetic field. At higher fields the negative MR becomes more gradual and eventually saturates. Ce-doped $SmB_6$ shows MR consistent with Kondo scattering. As the field is increased, the Ce local moments become polarized and the spin-flip scattering is reduced, resulting in a reduction in resistivity. This process should be independent of applied field direction, which was indeed observed for Ce-doped samples. The peak near zero field may also be due to Kondo scattering in the Gd-doped samples.
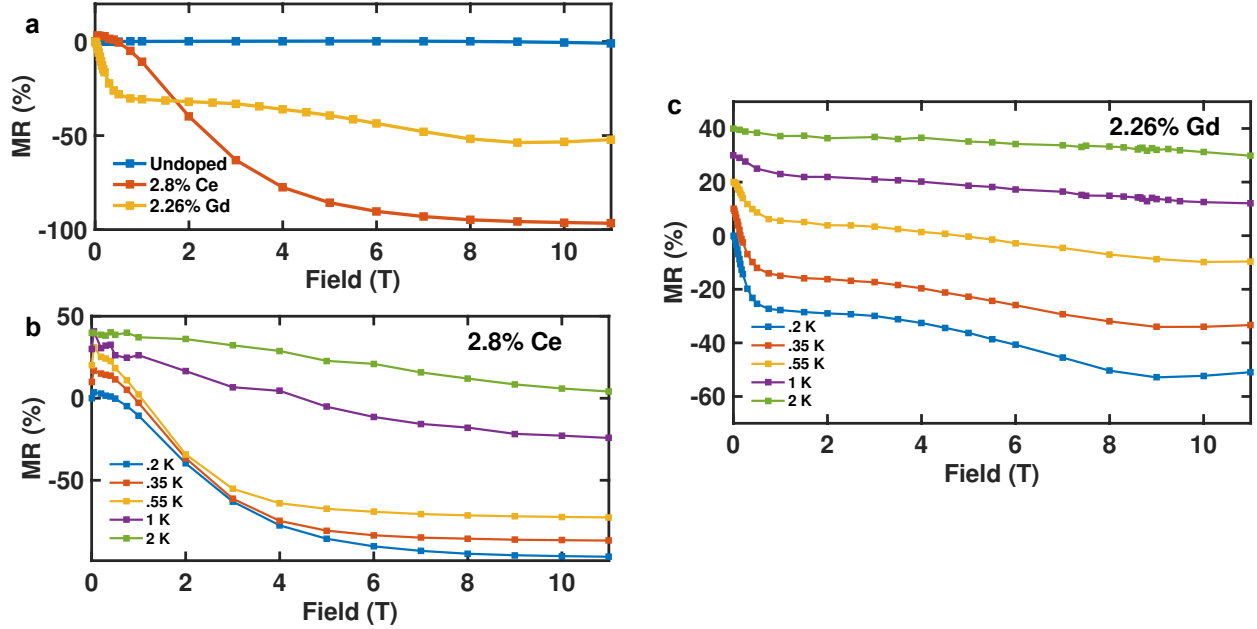
Figure 4.15: Magnetoresistance comparison between Ce- and Gd-doped SmB$_6$. (a) Resistance versus field at 200 mK between undoped, Ce-doped, and Gd-doped SmB$_6$. (b) Resistance versus field for Ce-doped SmB$_6$ at several different temperatures. (c) Resistance versus field for Gd-doped SmB$_6$ at several different temperatures.

Since the spin of the Gd-doped samples is larger, they may tend to align more quickly with applied field. However, this does not explain why there is a second region of much more gradual negative MR. Also, the feature near zero field is not related to 2D weak-localization. The effect is independent of the direction of the applied field, showing that it is not a surface effect.

One obvious question to ask is whether the difference in MR might also arise from the fact that Ce-doping preserves the metallic surface state of undoped SmB$_6$. To determine whether there is a surface state in Ce-doped SmB$_6$, the resistance ratio measurement described above was performed on crystals with nominal 1% and 3% Ce-doping. Most of the samples measured resulted in inconclusive results. Very often, the ratio after polishing had almost no relation to the thickness ratio, even at room temperature. The reason for this is likely due to large inhomogenieties in the Ce-doping throughout the body of a single crystal (this will be described more below). However, as figure 4.16 shows, three samples with 1% nominal
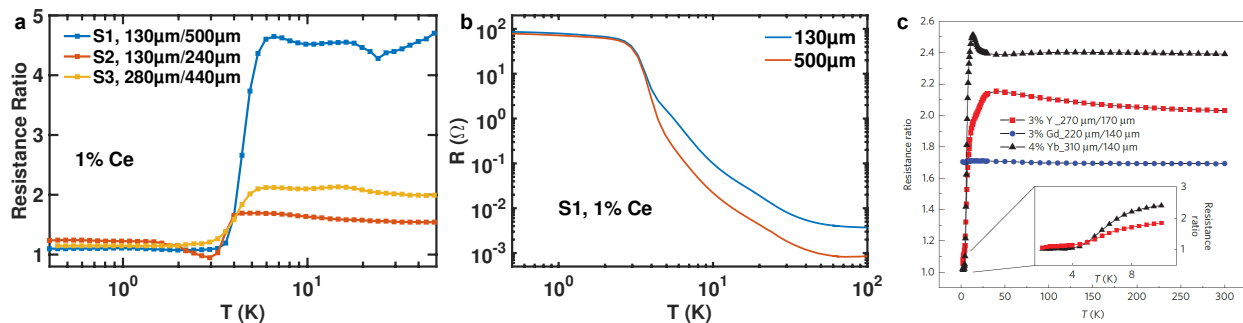
Figure 4.16: Survey of resistivity versus temperature of Ce- and Gd-doped SmB$_6$. (a) Resistance ratio of selected, nominally 1% Ce-doped SmB$_6$ crystals. (b) Resistance versus temperature for S1 from resistance ratio plot. (c) In a Gd-doped study performed by Kim et al. it was shown that Gd dopants result in bulk conduction dominating down to 2 K.[82]

doping concentration were measured that appeared to exhibit surface conduction due to a crossover of the resistance ratio to unity at low temperatures.

Unfortunately, it was impossible to determine whether the surface state can coexist with Ce-doping. The Ce-doped samples that showed promise of surface conduction were submitted to energy-dispersive X-ray spectroscopy (EDS). This technique is able to determine the relative elemental concentrations near the surface of a sample. All three Ce-doped samples that exhibited surface conduction had Ce-levels below the minimum detection threshold on the side on which the measurement leads were attached. Thus, it seems that the surface state was only confirmed on samples with a nearly undoped surface. At the same time, the back side of one of the sample showed over 4% Cerium concentration. While EDS may have an uncertainty of about half a percent for low sample concentrations, the difference between 0% on the side with the leads and 4% on the backside is significant. This may explain why the resistance ratio never showed very much correlation with the thickness ratio at room temperature. If the room temperature resistance is sensitive to the doping concentration and the doping is uneven throughout the body of the sample, the resistivity of the portion of the sample that was polished off may not match the resistivity of the remaining part of the sample. Under this scenario, the resistance ratio is not necessarily related to the thickness ratio. While the resistivity results presented below show that Ce-doped SmB$_6$ is much less
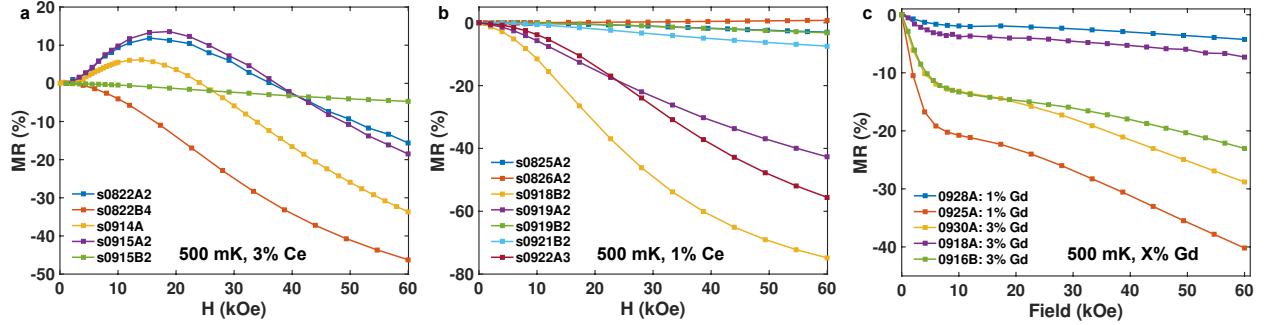
Figure 4.17: Survey of magnetoresistance of Ce- and Gd-doped SmB$_6$ at 500 mK. (a) Nominally 3% Ce-doped samples. (b) Nominally 1% Ce-doped samples. (c) Nominally X% Gd-doped samples (see legend).

sensitive to doping concentration than Gd-doped SmB$_6$, it is still a non-negligible effect. Also, if the temperature dependence of the resistivity depends on the doping concentration, the resistance ratio may not even be constant with temperature even in the high temperature limit when bulk conduction is dominating.

Even though the inhomogeneities in the sample may prevent making any certain claims about the existence of the surface state in Ce-doped SmB$_6$, comparing a large number of samples with both 1% and 3% nomial doping may at least allow some general trends to be observed. Figure 4.17 panels (a) and (b) show magnetoresistance (MR) for 3% and 1% Ce-doped samples respectively. The percent change of MR at 60 kOe shows very little correlation with nominal doping percentage. However, the 1% samples showed a larger percentage of crystals with very little MR (one of them even shows a slightly positive MR). Also, some of the 3%-doped samples show a region with positive MR for fields less than 20 kOe. This may be due to the onset of Kondo coherence of the Ce-ions as the concentration is increased.[84] As the concentration is lowered this peak moves toward 0 T, it may be that eventually the region of positive MR disappears. The samples showing positive MR tend to have a small feature reminiscent of the logarithmic rise in resistance followed by a drop in resistivity expected when first excited crystal field level is depopulated (see figure 4.18(a)). Instead of the temperature continuing to drop below this feature, the hybridization gap from the SmB$_6$
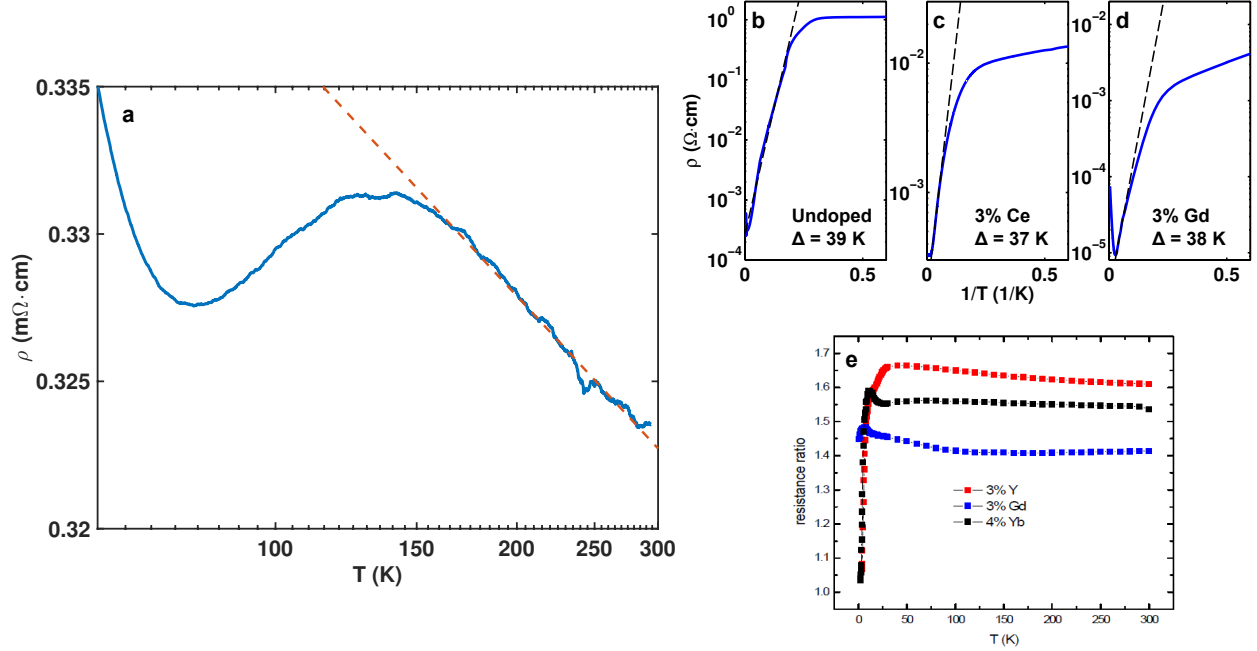
Figure 4.18: Resistivity feature in 3% Ce-doped SmB$_6$, bulk gap, and resistance ratio plot. (a) Resistivity versus temperature for nominally 3%-doped Ce SmB$_6$ showing high temperature peak in resistivity preceded by a logarithmic rise. (b)–(d) Arrhenius plots for undoped and doped SmB$_6$ samples, showing that the bulk gap is largely unaffected by low concentrations of dopants. (e) Resistance ratio plot from supplemental of Kim et al.,[82] hinting that at low temperature the resistance ratio might start to approach unity in a second 3% Gd-doped sample.

lattice quickly gives rise to an exponential increase in resistance. However, the temperature at which the feature occurs is near 130 K. In CeB$_6$, the first excited level is at 30 K.[85] If this feature was from an interpenetrating CeB$_6$ lattice, it should occur at lower temperature. It is also possible that this feature is not related to the Ce-doping at all. A broad maximum in the same temperature range was previously reported in undoped SmB$_6$ and may be related to a magnetic excitation that was observed in neutron scattering.[86, 87] Finally, the bulk gap extracted from the resistance rise in doped SmB$_6$ is almost identical to an undoped sample. For both Ce and Gd dopings, the temperature at which the resistance begins to deviate from the fit is higher than in undoped SmB$_6$, suggesting the earlier onset of a secondary conduction channel.

Figure 4.19 presents a survey of the resistivities of many Ce- and Gd-doped samples. All
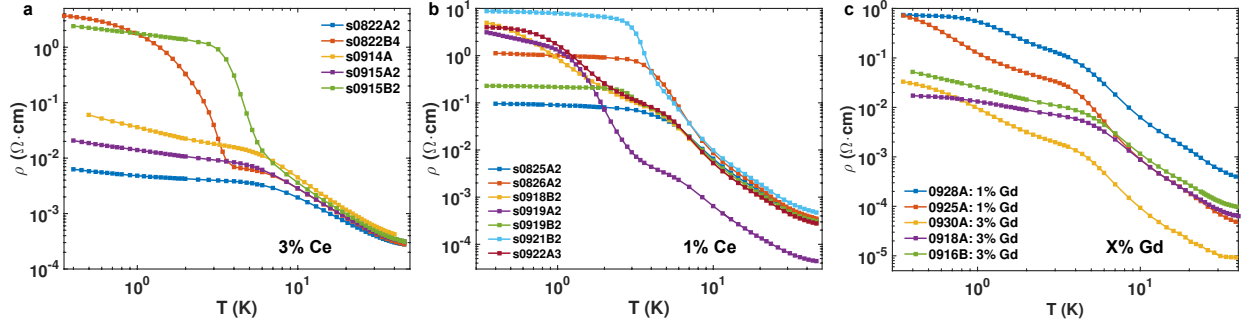
Figure 4.19: Survey of resistivity versus temperature of Ce- and Gd-doped $SmB_6$. (a) Nominally 3% Ce-doped samples. (b) Nominally 1% Ce-doped samples. (c) Nominally X% Gd-doped samples (see legend).

but one of the Ce-doped samples has a resistivity near .3 m$\Omega$·cm at 40 K, which is close the the resistivity of undoped $SmB_6$ at the same temperature reported by several other groups.[88] This means that Ce-doping has relatively little influence on transport in the bulk at high temperatures. The saturation resistivity varies over two orders of magnitude between samples of a given nominal concentration. The large variance in saturation resistivity may be related to the large deviations from nominal concentration observed in Ce-doped $SmB_6$ during EDS measurements.

Gadolinium doping seems to have a much larger influence on the resistivity of the bulk. Only one sample exhibited resistivity similar to undoped $SmB_6$ at 40 K. Every other sample had significantly lower resistivity. Further, the saturation resistivity shows a very clear difference between 1% and 3% nominal concentrations. Not as many Gd-doped samples were subjected to EDS analysis, so it is unknown whether they suffer from the same concentration issues as the Ce-doped samples. A previous study with Gd-doped $SmB_6$ found an even smaller saturation resistance in a 1% Gd-doped sample when compared to the 3% samples studied here.[89] It was suggested that the main role of the Gd was to dope $SmB_6$ with extra electrons.

Coming back to the question of the lack of a surface state in Gd-doped $SmB_6$ that was reported by Kim et al., it is unclear whether this is a universal feature in Gd-doped crystals. They reported a diverging resistivity below 1 K in Gd-doped crystals.[82] While some the

Gd-doped samples studied here do show a secondary divergence after the hints of an initial resistance plateau, none of them appear to have diverging resistance down to the minimum temperature measured (typically 350 mK). Instead, the resistivity of most of the samples appears to eventually saturate, although the temperature at which the second saturation starts is highly sample dependent. If the bulk is more conductive due to the addition of electrons from $SmB_6$, the temperature at which the surface begins to dominate conduction would be lower compared to undoped $SmB_6$. Figure 4.18(e) shows a second resistance ratio plot from the supplemental materials of Kim et al.[82] At the very lowest temperature measured, it appears that the resistance ratio of the 3% Gd-doped sample is beginning to decrease. From the provided plot it is impossible to tell what the minimum measured temperature was, but it would be interesting to know whether the ratio would continue to decrease as the temperature is lowered.

Due to issues with sample inhomogeneity, it remains an open question as to whether the surface state still exists in Ce-doped crystals. Taking the combined evidence of the lack of magnetic Iron ions or applied field destroying the surface state, with the sample variation in Gd-doped samples, it may be worth taking a second look as to whether dilute Gadolinium doping actually destroys the surface state. To accomplish this, much more homogenous crystals will have to be grown. This might be accomplished by alloying stoichiometric $GdB_6$ and $SmB_6$ in a 50/50 concentration, and then repeatedly alloying the result 50/50 with undoped $SmB_6$ to hopefully obtain a more homogenous result in the dilute limit.

# Bibliography

[1] J. Kondo, Prog. Theor. Phys. **32**, 37 (1964).

[2] P. Coleman, Handb. Magn. Adv. Magn. Mater. **1**, 97 (2006).

[3] S. Doniach, Phys. B+C **91**, 231 (1977).

[4] P. Misra, *Heavy-Fermion Systems* (Elsevier B.V., 2008).

[5] G. R. Stewart, Rev. Mod. Phys. **56**, 755 (1984).

[6] L. Degiorgi, Rev. Mod. Phys. **71**, 687 (1999).

[7] Z. Fisk, J. Sarrao, S. Cooper, P. Nyhus, G. Boebinger, A. Passner, and P. Canfield, Phys. B Condens. Matter **223-224**, 409 (1996).

[8] M. Dzero, K. Sun, V. Galitski, and P. Coleman, Phys. Rev. Lett. **104**, 106408 (2010).

[9] T. Takimoto, J. Phys. Soc. Japan **80**, 123710 (2011).

[10] F. Pobell, *Matter and methods at low temperatures*, 3rd ed. (Springer, 2007).

[11] S. Blundell, *Magnetism in Condensed Matter* (Oxford University Press, 2001).

[12] S. C. Whitmore, S. R. Ryan, and T. M. Sanders, Rev. Sci. Instrum. **49**, 1579 (1978).

[13] D. Schoenberg, *Magnetic Oscillations in Metals* (Cambridge University Press, 1984).

[14] L. Li, J. G. Checkelsky, Y. S. Hor, C. Uher, a. F. Hebard, R. J. Cava, and N. P. Ong, Science **321**, 547 (2008).

[15] J. Eisenstein, H. Stormer, V. Narayanamurti, A. Cho, A. Gossard, and C. Tu, Phys. Rev. Lett. **55**, 875 (1985).

[16] J. Chiaverini, K. Yasumura, and A. Kapitulnik, Phys. Rev. B **64**, 014516 (2001).

[17] B. D. Cullity, *Introduction to Magnetic Materials* (Addison-Wesley Publishing Company, 1972).

[18] M. T. Johnson, P. J. H. Bloemen, F. J. A. den Broeder, and J. J. de Vries, Reports Prog. Phys. **59**, 1409 (1996).

[19] T. Kohda, Y. Otani, V. Novosad, K. Fukamichi, S. Yuasa, M. Nyvlt, and T. Katayama, IEEE Trans. Magn. **35**, 3472 (1999).

[20] R. I. Joseph and E. Schlomann, J. Appl. Phys. **36**, 1579 (1965).

[21] U. Gradmann, J. Magn. Magn. Mater. **54-57**, 733 (1986).

[22] S. Huang and A. Stott, J. Phys. E. **21**, 242 (1988).

[23] J. P. Cleveland, S. Manne, D. Bocek, and P. K. Hansma, Rev. Sci. Instrum. **64**, 403 (1993).

[24] K. Gupta, R. Garg, I. Bahl, and P. Bhartia, *Microstrip Lines and Slotlines*, 2nd ed. (Artec House, Inc., 1996).

[25] N. Lea, J. Inst. Electr. Eng. - Part III Radio Commun. Eng. **92**, 261 (1945).

[26] M. Cotinaud, P. Bonniau, and A. R. Bunsell, J. Mater. Sci. **17**, 867 (1982).

[27] L. Onsager, Philos. Mag. **43**, 1006 (1952).

[28] Y. Ishizawa, H. Nozaki, T. Tanaka, and T. Nakajima, J. Phys. Soc. Japan **48**, 1439 (1980).

[29] Y. Ishizawa, T. Tanaka, E. Bannai, and S. Kawai, J. Phys. Soc. Japan **42**, 112 (1977).

[30] J. Custers, P. Gegenwart, H. Wilhelm, K. Neumaier, Y. Tokiwa, O. Trovarelli, C. Geibel, F. Steglich, C. Pépin, and P. Coleman, Nature **424**, 524 (2003).

[31] C. Petrovic, P. G. Pagliuso, M. F. Hundley, R. Movshovich, J. L. Sarrao, J. D. Thompson, Z. Fisk, and P. Monthoux, J. Phys. Condens. Matter **13**, L337 (2001).

[32] P. Haen, J. Flouquet, F. Lapierre, P. Lejay, and G. Remenyi, J. Low Temp. Phys. **67**, 391 (1987).

[33] S. Araki, N. Metoki, A. Galatanu, E. Yamamoto, A. Thamizhavel, and Y. nuki, Phys. Rev. B **68**, 024408 (2003).

[34] E. Jobiliong, J. S. Brooks, E. S. Choi, H. Lee, and Z. Fisk, Phys. Rev. B **72**, 1 (2005).

[35] L. Balicas, S. Nakatsuji, H. Lee, P. Schlottmann, T. Murphy, and Z. Fisk, Phys. Rev. B **72**, 064422 (2005).

[36] A. Thamizhavel, A. Galatanu, E. Yamamoto, T. Okubo, M. Yamada, K. Tabata, T. C Kobayashi, N. Nakamura, K. Sugiyama, K. Kindo, T. Takeuchi, R. Settai, and Y. nuki, J. Phys. Soc. Japan **72**, 2632 (2003).

[37] C. Petrovic, S. Budko, J. Strand, and P. Canfield, J. Magn. Magn. Mater. **261**, 210 (2003).

[38] C. Adriano, P. F. S. Rosa, C. B. R. Jesus, J. R. L. Mardegan, T. M. Garitezi, T. Grant, Z. Fisk, D. J. Garcia, a. P. Reyes, P. L. Kuhns, R. R. Urbano, C. Giles, and P. G. Pagliuso, Phys. Rev. B **90**, 235120 (2014).

[39] C. Adriano, P. F. S. Rosa, C. B. R. Jesus, T. Grant, Z. Fisk, D. J. Garcia, and P. G. Pagliuso, J. Appl. Phys. **117**, 17C103 (2015).

[40] A. Goldstein, S. J. Williamson, and S. Foner, Rev. Sci. Instrum. **36**, 1356 (1965).

[41] K. W. H. Stevens, Proc. Phys. Soc. Sect. A **65**, 209 (1952).

[42] K. Wang, D. Graf, and C. Petrovic, Phys. Rev. B **87**, 235101 (2013).

[43] K. Myers, S. Bud'ko, I. Fisher, Z. Islam, H. Kleinke, A. Lacerda, and P. Canfield, J. Magn. Magn. Mater. **205**, 27 (1999).

[44] S. L. Budko, E. Morosan, and P. C. Canfield, Phys. Rev. B **69**, 014415 (2004).

[45] J. K. Dong, Y. Tokiwa, S. L. Budko, P. C. Canfield, and P. Gegenwart, Phys. Rev. Lett. **110**, 176402 (2013).

[46] Y. Tokiwa, M. Garst, P. Gegenwart, S. L. Budko, and P. C. Canfield, Phys. Rev. Lett. **111**, 116401 (2013).

[47] J. Paglione, M. a. Tanatar, D. G. Hawthorn, E. Boaknin, R. W. Hill, F. Ronning, M. Sutherland, L. Taillefer, C. Petrovic, and P. C. Canfield, Phys. Rev. Lett. **91**, 246405 (2003).

[48] S. Nair, S. Wirth, S. Friedemann, F. Steglich, Q. Si, and A. J. Schofield, Adv. Phys. **61**, 583 (2012).

[49] J. Smit, Physica **21**, 877 (1955).

[50] L. Berger, Phys. Rev. B **2**, 4559 (1970).

[51] M. V. Berry, Proc. R. Soc. London A **392**, 45 (1984).

[52] L. Taillefer, J. Flouquet, and W. Joss, J. Magn. Magn. Mater. **76-77**, 218 (1988).

[53] E. D. Mun, S. L. Bud'Ko, A. Kreyssig, and P. C. Canfield, Phys. Rev. B **82**, 1 (2010).

[54] A. Menth, E. Buehler, and T. H. Geballe, Phys. Rev. Lett. **22**, 295 (1969).

[55] L. Fu, C. L. Kane, and E. J. Mele, Phys. Rev. Lett. **98**, 106803 (2007).

[56] J. E. Moore and L. Balents, Phys. Rev. B **75**, 121306 (2007).

[57] R. Roy, Phys. Rev. B **79**, 195322 (2009).

[58] D. Hsieh, D. Qian, L. Wray, Y. Xia, Y. S. Hor, R. J. Cava, and M. Z. Hasan, Nature **452**, 970 (2008).

[59] S. R. Elliott and M. Franz, Rev. Mod. Phys. **87**, 137 (2015).

[60] X.-L. Qi and S.-C. Zhang, Rev. Mod. Phys. **83**, 1057 (2011).

[61] M. Hasan and C. Kane, Rev. Mod. Phys. **82**, 3045 (2010).

[62] M. Neupane, N. Alidoust, S.-Y. Xu, T. Kondo, Y. Ishida, D. J. Kim, C. Liu, I. Belopol-ski, Y. J. Jo, T.-R. Chang, H.-T. Jeng, T. Durakiewicz, L. Balicas, H. Lin, A. Bansil, S. Shin, Z. Fisk, and M. Z. Hasan, Nat. Commun. **4**, 2991 (2013).

[63] N. W. Ashcroft and N. D. Mermin, *Solid State Physics* (Brooks/Cole, 1976).

[64] F. Lu, J. Zhao, H. Weng, Z. Fang, and X. Dai, Phys. Rev. Lett. **110**, 096401 (2013).

[65] V. Alexandrov, M. Dzero, and P. Coleman, Phys. Rev. Lett. **111**, 226403 (2013).

[66] S. Wolgast, Ç. Kurdak, K. Sun, J. W. Allen, D.-J. Kim, and Z. Fisk, Phys. Rev. B **88**, 180405 (2013).

[67] N. Wakeham, Y. Q. Wang, Z. Fisk, F. Ronning, and J. D. Thompson, Phys. Rev. B **91**, 085107 (2015).

[68] J. C. Cooley, C. H. Mielke, W. L. Hults, J. D. Goettee, M. M. Honold, R. M. Modler, A. Lacerda, D. G. Rickel, and J. L. Smith, J. Supercond. **12**, 171 (1999).

[69] S. Wolgast, Y. S. Eo, T. Öztürk, G. Li, Z. Xiang, C. Tinsman, T. Asaba, B. Lawson, F. Yu, J. W. Allen, K. Sun, L. Li, Ç. Kurdak, D.-J. Kim, and Z. Fisk, Phys. Rev. B **92**, 115110 (2015).

[70] S. Thomas, D. J. Kim, S. B. Chung, T. Grant, Z. Fisk, and J. Xia, Arxiv (2013), arXiv:1307.4133 .

[71] G. Li, Z. Xiang, F. Yu, T. Asaba, B. Lawson, P. Cai, C. Tinsman, A. Berkley, S. Wolgast, Y. S. Eo, D.-J. Kim, C. Kurdak, J. W. Allen, K. Sun, X. H. Chen, Y. Y. Wang, Z. Fisk, and L. Li, Science (80-. ). **346**, 1208 (2014).

[72] Y. Luo, H. Chen, J. Dai, Z.-a. Xu, and J. D. Thompson, Phys. Rev. B **91**, 075130 (2015).

[73] B. S. Tan, Y.-T. Hsu, B. Zeng, M. C. Hatnean, N. Harrison, Z. Zhu, M. Hartstein, M. Kiourlappou, A. Srivastava, M. D. Johannes, T. P. Murphy, J.-H. Park, L. Balicas, G. G. Lonzarich, G. Balakrishnan, and S. E. Sebastian, Science (80-. ). **349**, 287 (2015).

[74] V. Alexandrov, P. Coleman, and O. Erten, Phys. Rev. Lett. **114**, 177202 (2015).

[75] J. Knolle and N. R. Cooper, Phys. Rev. Lett. **115**, 146401 (2015).

[76] C. Larson and W. Gordon, Phys. Lett. **15**, 121 (1965).

[77] C. O. Larson and W. L. Gordon, Phys. Rev. **156**, 703 (1967).

[78] E. M. Gunnersen, Philos. Trans. R. Soc. A Math. Phys. Eng. Sci. **249**, 299 (1957).

[79] E. I. Blount, Phys. Rev. **126**, 1636 (1962).

[80] P. T. Coleridge and P. M. Holtham, J. Phys. F Met. Phys. **7**, 1891 (1977).

[81] S. Caplan and G. Chanin, Phys. Rev. **138**, A1428 (1965).

[82] D. J. Kim, J. Xia, and Z. Fisk, Nat. Mater. **13**, 466 (2014).

[83] N. Wakeham, J. Wen, Y. Wang, Z. Fisk, F. Ronning, and J. Thompson, J. Magn. Magn. Mater. , 1 (2015).

[84] F. J. Ohkawa, Phys. Rev. Lett. **64**, 2300 (1990).

[85] E. Zirngiebl, B. Hillebrands, S. Blumenröder, G. Güntherodt, M. Loewenhaupt, J. M. Carpenter, K. Winzer, and Z. Fisk, Phys. Rev. B **30**, 4052 (1984).

[86] A. Kebede, M. Aronson, C. Buford, P. Canfield, Jin Hyung Cho, B. Coles, J. Cooley, J. Coulter, Z. Fisk, J. Goettee, W. Hults, A. Lacerda, T. McLendon, P. Tiwari, and J. Smith, Phys. B Condens. Matter **223-224**, 256 (1996).

[87] P. A. Alekseev, V. N. Lazukov, R. Osborn, B. D. Rainford, I. P. Sadikov, E. S. Konovalova, and Y. B. Paderno, Europhys. Lett. **23**, 347 (1993).

[88] K. Kojima, M. Kasaya, and Y. Koi, J. Phys. Soc. Japan **44**, 1124 (1978).

[89] T. H. Geballe, J. Appl. Phys. **41**, 904 (1970).